



Government of **Western Australia**
Department of **Mines and Petroleum**

RECORD 2015/3

ALTERATION MINERAL ZONATION ASSOCIATED WITH HIGH-GRADE BIF-HOSTED IRON ORE: MINERAL MAPPING USING HYPERSPECTRAL DRILL CORE DATA

by
L Chiarelli



Geological Survey
of Western Australia



THE UNIVERSITY OF
WESTERN AUSTRALIA



EXPLORATION
INCENTIVE SCHEME



Government of **Western Australia**
Department of **Mines and Petroleum**

Record 2015/3

ALTERATION MINERAL ZONATION ASSOCIATED WITH HIGH-GRADE BIF-HOSTED IRON ORE: MINERAL MAPPING USING HYPERSENSITIVE DRILL CORE DATA

by
L Chiarelli

Perth 2015



**Geological Survey of
Western Australia**

MINISTER FOR MINES AND PETROLEUM
Hon. Bill Marmion MLA

DIRECTOR GENERAL, DEPARTMENT OF MINES AND PETROLEUM
Richard Sellers

EXECUTIVE DIRECTOR, GEOLOGICAL SURVEY OF WESTERN AUSTRALIA
Rick Rogerson

REFERENCE

The recommended reference for this publication is:

Chiarelli, L 2015, Alteration mineral zonation associated with high-grade BIF-hosted iron ore: mineral mapping using hyperspectral drill core data: Geological Survey of Western Australia, Record 2015/3, 156p.

National Library of Australia Card Number and ISBN 978-1-74168-655-5

Grid references in this publication refer to the Geocentric Datum of Australia 1994 (GDA94). Locations mentioned in the text are referenced using Map Grid Australia (MGA) coordinates, Zone 50. All locations are quoted to at least the nearest 100 m.

About this publication

This Record is an Honours thesis researched, written and compiled through an ongoing collaborative project between the Geological Survey of Western Australia (GSWA) and The University of Western Australia, to investigate the origin of, and exploration for, banded iron-formation hosted iron ore deposits in the Yilgarn Craton. Although GSWA has provided funding for this project, the scientific content of the Record and the drafting of figures have been the responsibility of the author. No editing has been undertaken by GSWA.



THE UNIVERSITY OF
WESTERN AUSTRALIA



EXPLORATION
INCENTIVE SCHEME

Published 2015 by Geological Survey of Western Australia

This Record is published in digital format (PDF) and is available online at <www.dmp.wa.gov.au/GSWApublications>.

Disclaimer

This product was produced using information from various sources. The Department of Mines and Petroleum (DMP) and the State cannot guarantee the accuracy, currency or completeness of the information. DMP and the State accept no responsibility and disclaim all liability for any loss, damage or costs incurred as a result of any use of or reliance whether wholly or in part upon the information provided in this publication or incorporated into it by reference.

Further details of geological products and maps produced by the Geological Survey of Western Australia are available from:

Information Centre
Department of Mines and Petroleum
100 Plain Street
EAST PERTH WESTERN AUSTRALIA 6004
Telephone: +61 8 9222 3459 Facsimile: +61 8 9222 3444
www.dmp.wa.gov.au/GSWApublications

This thesis is submitted in partial fulfilment of the requirements for a
Bachelor of Science: Geology and Natural Resource Economics
70100

FNAS Research Thesis
Faculty of Science
The University of Western Australia
October 2013

**Alteration Mineral Zonation Associated with High-Grade BIF-
Hosted Iron Ore: mineral mapping using hyperspectral drill core
data**

Laura Chiarelli

Supervisors: Paul Duuring (UWA- CET), Carsten Laukamp (CSIRO), Steffen
Hageman (UWA- CET)

ABSTRACT

The central aim of this research project is to test the efficacy of recently applied hyperspectral logging techniques (the ‘HyLoggingTM system’) for the accurate mapping of hypogene and supergene iron oxide minerals and alteration zones in Banded Iron Formation and surround mafic igneous rocks. Core from a single diamond drill hole (PK11DD001) from the Mount Richardson BIF-hosted iron ore prospect in the Southern Cross domain of the Yilgarn Craton was scanned at the GSWA Core Library, Perth. The recorded spectral data are interpreted by comparing the data with results from conventional core logging techniques, as well as petrologic and geochemical studies. BIF in drill hole PK11DD001 is affected by early hypogene magnetite-quartz alteration (stage one), hypogene specularite-martite (stage two) and supergene goethite alteration (stage three). Adjacent mafic igneous rocks are altered to hypogene chlorite with proximity to contacts with BIF-hosted iron ore zones. Later supergene goethite and hematite replace primary, metamorphic and hypogene minerals. Hyperspectral data provide detailed resolution that allows the mapping of variations in mineral abundance and chemistry in primary, metamorphic and hypogene/supergene alteration minerals in BIF and mafic rocks. Existing computer-based scripts, including ferric oxide abundance, hematite-goethite and ochreous goethite-vitreous goethite are useful for identifying BIF, and for characterising the different alteration and iron ore styles in BIF. Furthermore, a specular hematite script developed by this study has a higher accuracy than existing scripts for the identification of hypogene specularite ore zones in BIF. Mafic igneous rocks demonstrate zonation in primary and metamorphic minerals; from amphibole in distal areas to BIF contacts, to hypogene chlorite in proximal zones. Within 10 m of BIF contacts, these minerals are entirely replaced by supergene hematite, goethite and kaolinite. Furthermore, hyperspectral data indicate that hypogene chlorite becomes increasingly Mg-rich with proximity to shear zones and BIF-hosted specularite ore zones. Mineral mapping using hyperspectral data is a valuable tool that can be integrated with conventional logging and analytical techniques. The results of this study, such as the new specular hematite script, can potentially be applied to interrogating remote sensing data. However, further work is required to first test the effects of down-sampling the hyperspectral data to match the spectral resolution of the remote sensing data sets (e.g. ASTER, HyMap).

Key words: Mount Richardson, Banded Iron Formation, Hyperspectral Hematite, Hypogene, Supergene

TABLE OF CONTENTS

ABSTRACT	2
ACKNOWLEDGEMENTS	5
RESEARCH THESIS	6
INTRODUCTION	6
METHODOLOGY	7
Conventional logging of diamond drill core	7
Geochemistry	7
Petrography	9
Hyperspectral technologies: HyLogging system	9
Mineral spectroscopy	10
Terminology	11
GEOLOGICAL BACKGROUND TO THE MOUNT RICHARDSON PROSPECT AREA	12
Yilgarn Craton	12
Illaara greenstone belt of the Southern Cross domain	13
Mount Richardson prospect	14
PETROGRAPHY OF LEAST ALTERED ROCK TYPES OBSERVED IN DRILL HOLE PKDD11001	17
BIF	17
Mafic igneous rock	17
Transported sediment	17
HYDROTHERMAL ALTERATION OF BIF AND MAFIC IGNEOUS ROCKS	21
BIF	21
STAGE ONE HYPOGENE ALTERATION: MAGNETITE-QUARTZ	21
STAGE TWO HYPOGENE ALTERATION: SPECULARITE AND MARTITE	21
STAGE THREE SUPERGENE ALTERATION: GOETHITE	22
Mafic igneous rocks	24
GEOCHEMISTRY OF ALTERED BIF AND MAFIC IGNEOUS ROCKS	27
Least- altered BIF	27
Hypogene- altered BIF	27
Supergen-altered BIF	28
Least-altered mafic	29
Intermediate alteration zones in mafic igneous rocks	30
Proximal alteration zones in mafic igneous rocks	31
HYPERSPETRAL DATA	32
Specular hematite script	35
BIF	35
Mafic igneous rocks	39
Transported material	41

DISCUSSION.....	43
Relating observed changes in hydrothermal alteration minerals to geochemistry at Mount Richardson.....	43
BIF	43
GABBRO.....	45
Mapping rock types and alteration zones at Mount Richardson using hyperspectral data.....	45
BIF	45
GABBRO	46
Evaluating the usefulness of hyperspectral studies to iron ore exploration	47
CONCLUSION	49
REFERENCES	51

APPENDICES

Appendix 1: Research Proposal	54
Appendix 2: Geochemical analysis results (USB)	89
Appendix 3: Grant Plot.....	96
Appendix 4: Mass balance analysis data (USB).....	101
Appendix 5: Diamond drill hole log	108
Appendix 6: Diamond drill hole hyperspectral data	113
Appendix 7: Whole rock and trace element geochemistry	116
Appendix 8: Thin section descriptions.....	131
Appendix 9: Geosciences product descriptions (MFEM SCRIPTS) selected VNIR and SWIR active mineral groups/phases.....	141
Appendix 10: hyperspectral image A3	155

Acknowledgments:

This work was fully supported and funded by Cliffs Natural Resources. GSWA is thanked for scanning the diamond drill core with the HyLogger and providing technical support related to core logging; for allowing me to occupy their busy core yard and covering my rocks when it was raining. The support and enthusiasm of supervisor Paul Duuring (UWA-CET) throughout this project provided invaluable improvements to this thesis and is very much appreciated. Carsten Laukamp (CSIRO) is also thanked for his guidance with interpreting hyperspectral data and creating new scripts in TSG.

RESEARCH THESIS

INTRODUCTION

Iron ore exploration is influenced by our understanding of geological processes for iron ore formation combined with the availability of effective methods for the detection of iron ore bodies. Several genetic models exist for the formation of high-grade iron ore deposits, including syngenetic (Lascelles 2006a), supergene-metamorphic (Morris 2007), and more recently the supergene-modified hypogene model (Barley et al. 1999, Taylor et al. 2001a). Each model may have validity, at least in certain districts. Presently, a more holistic “Mineral Systems” approach (Wyborn et al. 1994) is being applied to the study of iron ore systems (Angerer submitted). This approach attempts to describe the genesis of a deposit, from the source of fluids and metals, to the processes for fluid migration, deposition of metals, and to the downstream fluid outflow related to the system. Angerer et al (submitted) applied this approach to BIF-hosted high-grade iron ore where a knowledge gap exists for the defined source of these hydrothermal fluids, their composition, and how these fluids interacted with BIF and surrounding country rocks. Hydrothermal alteration mineral assemblages in BIF and country rocks may be used to constrain the composition of the fluids responsible for mineralisation. Alteration zones associated with high-grade hypogene iron ore have not yet been fully characterised. Newly developed spectral technologies, such as the HyLoggingTM system, have the potential to assist with the high-resolution characterisation of zoned alteration minerals towards high-grade iron ore.

This study is the first to use the HyLoggingTM system to test for the presence of pathfinder minerals associated with high-grade iron ore in BIF and mafic country rocks in the Yilgarn Craton. The HyLoggingTM system has the potential to distinguish important ore minerals (goethite, hematite and potentially specularite), as well as map the distribution of gangue minerals, such as kaolin group minerals in BIF. The acquired spectral data will be interpreted in conjunction with the results of conventional core logging, petrologic studies and bulk rock geochemical analysis. Interpreted spectra data may potentially be used to better interpret remote sensing spectral data (i.e. HyMap and ASTER) that show deposit- to district-scale distributions in mineral abundances and mineral chemistry.

METHODOLOGY

Conventional logging of diamond drill core

The diamond drill hole PK11DD001 is positioned in the Parker area of the Mount Richardson prospect and was drilled by Cliffs Natural Resources in 2011 for the purpose of testing the extent and chemistry of high-grade iron ore in BIF. The drill hole's collar position is located at 791814 mE, 6811030 mN (UTM grid system), and at an elevation of 479 mRL (relative to sea level). The 193.8 m-long hole was drilled at an angle of -60° from surface towards 090°. The drill hole was selected from a total of 16 diamond drill holes for detailed examination based on the hole intersecting fresh and weathered examples of BIF, high-grade iron ore zones, and surrounding mafic igneous countryrocks. The drill hole also has the potential to intersect hypogene alteration mineral zones associated with high-grade iron ore in BIF and mafic igneous countryrocks. Diamond drill hole PK11DD001 was transported from the Windarling mine site to the GSWA Core Library in Perth whereupon the core was cleaned, dried, and scanned with the HyLoggingTM system by GSWA personnel. The diamond drill core was then made available for conventional visual logging by the author. Visual logging included the documentation of relationships between rock types, textures, structures, and hypogene and supergene alteration mineral assemblages.

Geochemistry

Representative hand specimens of variably weathered and hypogene-altered BIF and mafic igneous rocks were selected for geochemical analyses. Seventeen 1-2 kg samples of diamond drill core were analysed by Actlabs Pacific Pty. Ltd. in Vancouver, Canada, for major oxides and trace elements, including Rare Earth Elements (REE). The hand specimens were initially crushed in a steel jaw crusher and then milled to a powder (<100 µm) in a tungsten-carbide mill, with quartz washes performed in between samples. Major element oxides were analysed using the X-ray fluorescence (XRF) method (10 major oxides), whereas trace elements and REE were analysed using inductively-coupled plasma mass spectrometry (ICP-MS) (45 trace elements). A combination of several sample digestion and analytical methods were used to achieve the most accurate and precise geochemical results for the elements of interest (Table 1).

Table 1 Actlabs Pacific Pty. Ltd. whole-rock geochemical assay summary by element preferred analytical method and detection limit.

Major elements		Trace elements						REE	
SiO ₂	0.01%	Ag	0.05ppm	Hf	0.1 ppm	Sn	1.0 ppm	La	0.05 ppm
Al ₂ O ₃	0.01%	As	0.1ppm	In	0.1 ppm	Sr	0.2 ppm	Ce	0.05 ppm
Fe ₂ O ₃	0.01%	Ba	1.0 ppm	Li	0.5 ppm	Ta	0.01 ppm	Pr	0.01 ppm
MnO	0.001%	Be	0.1 ppm	Mo	0.1 ppm	Te	0.05 ppm	Nd	0.05 ppm
MgO	0.01%	Bi	0.02 ppm	Nb	0.2 ppm	Th	0.05 ppm	Sm	0.01 ppm
CaO	0.01%	Cd	0.1 ppm	Ni	0.5 ppm	Tl	0.05 ppm	Eu	0.005 ppm
Na ₂ O	0.01%	Co	0.1 ppm	Pb	0.5 ppm	U	0.01 ppm	Gd	0.01 ppm
K ₂ O	0.01%	Cr	0.5 ppm	Rb	0.2 ppm	V	1.0 ppm	Tb	0.01 ppm
TiO ₂	0.001%	Cs	0.05 ppm	Re	0.01 ppm	W	0.1 ppm	Dy	0.01 ppm
P ₂ O ₅	0.01%	Cu	0.2 ppm	Sb	0.2 ppm	Y	0.5 ppm	Ho	0.01 ppm
LOI	0.01%	Ga	0.1 ppm	Sc	1.0 ppm	Zn	0.2 ppm	Er	0.01 ppm
Total	0.01%	Ge	0.5 ppm	Se	0.1 ppm	Zr	1.0 ppm	Tm	0.005 ppm
								Yb	0.01 ppm
								Lu	0.002ppm

Lab code	Method	Advantages/disadvantages
TD-MS	Four acid digest: hydrochloric, nitric, perchloric acids finished by mass spectrometry	Achieves low detection limits for most elements, however may not be quantitative for elements hosted in refractory minerals
FUS-ICP	Lithium metaborate/tetraborate fusion, bead dissolution in weak nitric acid and finished by ICP-OES	Suitable for major elements, transition metals and metalloids, as accurate or better than traditional XRF methods for major elements

FUS-MS	Lithium metaborate/tetraborate fusion, bead dissolution in weak nitric acid and finished by mass spectroscopy	Quantitative for all elements, including those hosted in refractory minerals, but slightly higher detection limits than TD-MS
--------	---	---

Analytical accuracy and precision for the geochemical data are measured through the submission of one international standard for BIF ((sample FeR-3; Bau and Alexander 2009), as well as the routine inclusion of several international standards by Actlabs, and the duplication of samples within the submitted sample suite.

Petrography

Seventeen samples of BIF and mafic igneous rocks were sent to Vancouver Petrographics Ltd., Vancouver, Canada, for the preparation of polished thin sections. The samples were examined using a reflected and transmitted light microscope. Petrographic observations include the documentation of iron oxide and silicate mineral relationships for each rock type and alteration style. Detailed thin section descriptions are presented in Appendix 8.

Hyperspectral technologies: HyLogging™

The HyLogging™ hyperspectral scanning system developed by CSIRO in Australia uses reflectance and emissivity spectra of scanned diamond drill core to identify mineral abundances and mineral chemistry (Clark 1984, Hunt 1977). The HyLogging™ system is operated by the GSWA in Perth and detects radiation reflected from the drill core within the visible to near infrared (VNIR: 380-1,000 nm), short wave infrared (SWIR: 1,000-2,500 nm) and thermal infrared (TIR: 6000-14000 nm) parts of the electromagnetic spectrum. The HyLogging™ system uses an automated xy-table that moves the core tray at intervals of 1 cm data resolution (Haest et al. 2012a). The reflectance spectra are cross-calibrated using a Spectralon™ panel. During the scanning process the HyLogging™ system also captures high resolution digital core images, which are referenced to a standard set of munsell colours. The hyperspectral data are then condensed to determine the abundance of minerals, as well as their composition and/or crystallinity, based on the wavelength, depth and width of diagnostic absorption features. Algorithms in this project were developed by CSIRO (Sonntag et al. 2012, Haest et al. 2012a, Laukamp 2011a) and were used to determine mineral abundance and composition

of iron oxides, including hematite, vitreous goethite and ochreous goethite and other minerals such as chlorite, carbonates, amphiboles, white micas and kaolin group minerals.

The collected VNIR and SWIR reflectance spectra were processed using the commercial software “The Spectral Geologist” (TSGTM), a full list of scripts used to determine abundances and compositions of common minerals is given in Appendix 9. Mineral abundance and composition information are extracted using the multiple feature extraction method (MFEM). Positions and depths of absorption features in this study are calculated by locally removing the hull from the reflectance spectra to reduce influence of instrument and/or atmospheric noise (Cudahy et al. 2008).

Mineral spectroscopy

The use of mineralogical diagnostic absorption features allows the identification of the mineralogy, although quantitative determination of this mineralogy is often more difficult (Clark 1984). Iron oxides produce diagnostic absorption features in the VNIR, which are caused by electronic processes involving Fe^{3+} cations octahedrally bonded to ligands of oxygen (hematite, $\alpha\text{Fe}_2\text{O}_3$) or oxygen and hydroxyl (goethite, αFeOOH) (Ramanaidou 1997) (Figure 1). These electronic processes include the transfer of electrons within electron orbits an ligand to metal iron (i.e. charge transfer). Energy of absorption processes (wavelength) can be altered by changes in valence state, coordination number, site symmetry, type of ligand, distortion of metal-ligand site, the length of the metal-ligand distance and mineral properties (grain size, shape, orientation, density, matrix and temperature (Sherman and Burns 1982, Adams and Flilic 1967, Morris et al. 1985, Singer and Roush 1985).

In major rock forming minerals, such as hydrated silicates and carbonates, diagnostic absorption features are located in the SWIR (Figure 1), which are related to the overtones of fundamental stretching vibrations and combination of fundamental stretching and bending vibrations of the hydroxyl group.

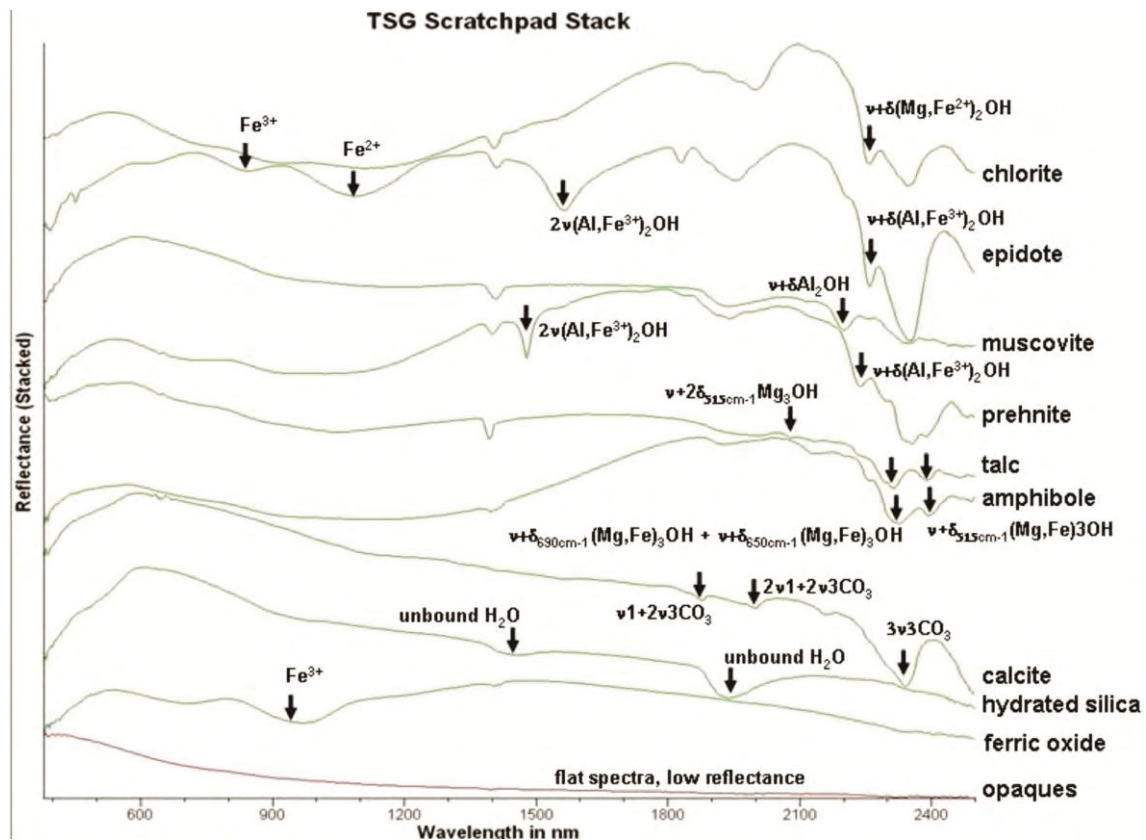


Figure 1 Visible-near (VNIR) to shortwave infrared (SWIR) reflectance spectra of selected rock forming minerals showing bands assignments of diagnostic absorption features, ν -stretching, δ -bending, bending $\nu + \delta$ combination of stretching and, 2ν first overtone of stretching fundamental, 3ν second overtone of stretching fundamental, νn arbitrary number of respective stretching vibration according to literature (Laukamp 2011a).

Terminology

The term “High-grade iron mineralisation” refers to Fe values that are greater than 50 % Fe, whereas “low-grade iron mineralisation” indicates Fe values that are between 25 and 50 %. “Martite” refers to the pseudomorphic replacement of magnetite by hematite (Clark 1993).

GEOLOGICAL BACKGROUND TO THE MOUNT RICHARDSON PROSPECT AREA

Yilgarn Craton

The Yilgarn Craton is primarily composed of Archaean granite-gneiss metamorphic and granite-greenstone terranes. The Craton is separated into five major terranes, which include the Narryer, South West areas, Murchison, Southern Cross and the Eastern Goldfields terrane (Figure 2). Narryer and South West areas are dominated by granite and granitoid-gneiss rocks while Murchison, Southern Cross and the Eastern Goldfields are granite-greenstones dominated terranes.

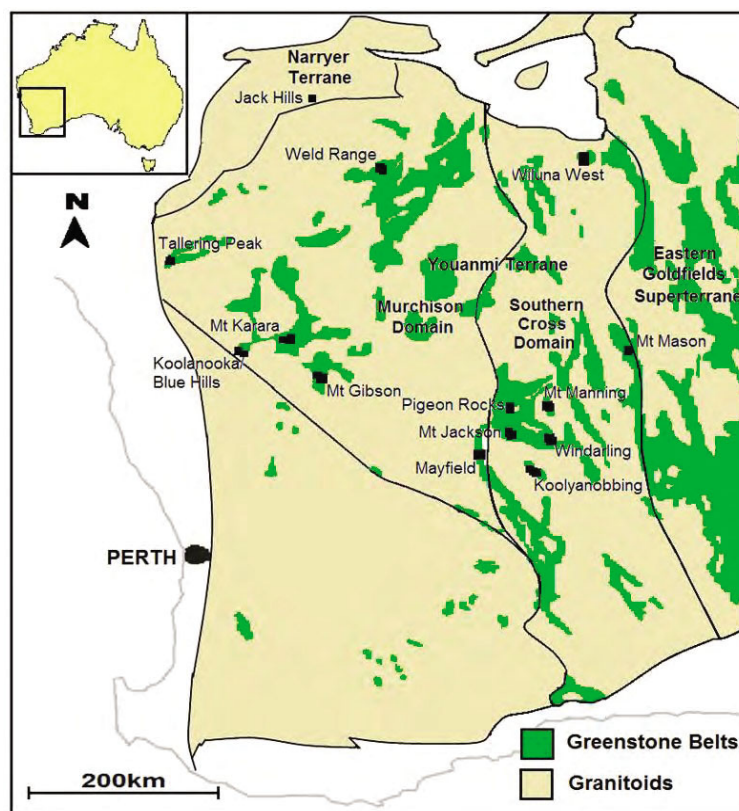


Figure 2 The Archaean granite-gneiss metamorphic and granite-greenstone terranes of the Yilgarn Craton, Western Australia. Divided into five terranes, Narryer, South West areas, Murchison, Southern Cross and the Eastern Goldfields terrane (Lascelles 2007, Cooper 2009)

The Mount Richardson iron ore prospect is located in the Southern Cross domain, approximately 530 km northwest of Perth and 130 km west of Leonora. Exploration of the Mount Richardson prospect area has identified several BIF macrobands that host high-grade iron ore. In these areas, the high grade ore is characterised by supergene goethite-martite that overprints an earlier hypogene magnetite-talc and hypogene specularite alteration. The most current geological report on the Mount Richardson area

is by Duuring (2013); the sections below on the Illara greenstone belt and the geology of the Mount Richardson prospect are summarised from this unpublished report.

Illara greenstone belt of the Southern Cross Domain

The Mount Richardson prospect lies within the Illara greenstone belt in the central-northern part of the Southern Cross Domain of the Youanmi Terrane, Yilgarn Craton (Chen 2004, Cassidy et al. 2006). The Illara greenstone belt is one of seven N-trending greenstone belts separated by monzogranite plutons in the Marmion and Richardson area. This greenstone belt comprises greenschist- to amphibolite-facies metamorphosed tholeiites, high Mg basalt, komatiite basalt, gabbro, banded iron formation, and chert, with minor ultramafic rocks and clastic sedimentary rocks (Chen 2004). Within the Richardson area the Illara greenstone belt trends N-S; the belt is up to 5 km wide near its northern extent, but is 1-2 km wide along most of the strike length. This greenstone belt is enveloped by granitoid plutons and western margins are defined by strongly foliated granitoid rocks of the Edale and Evanston shear zones. The quartzite located at the stratigraphic base of the Illara greenstone belt has a maximum depositional age of ca. 3130 Ma (U-Pb SHRIMP analysis of detrital zircons).

According to Chen (2004) three deformation events affect the greenstone belts within the Richardson district. The regional D₁ event involved N-S shortening and produced E-trending, tight to isoclinal folds, a layer-parallel foliation, and thrust faults. The second event D₂ took place during E-W shortening and granitoid plutonism at ca. 2755-2680 Ma (U-Pb SHRIMP analysis of zircon in granitoids), resulting in N-trending folds and an axial planar fabric in greenstone units, as well as gneissic banding in granitoid rocks. Continued E-W shortening occurred during subsequent D₃ event at ca. 2680-2655 Ma (U-Pb SHRIMP analysis of zircon in granitoid) resulted in the progressive tightening of earlier fold hinges, and the formation of the N-W-trending, sinistral Edale shear zone and the NE-trending, dextral Evanston shear zone.

Mount Richardson prospect

Geology relationships for the Mount Richardson prospect area has recently been documented based on detailed mapping of lithological and structural relationships in this area by Duuring (2013). This study demonstrates that the Mount Richardson prospect area coincides with a prominent <700 m-wide, NNW-SSE trending range of hills that extend about 140 m above the surrounding plains. This range extends along strike for more than 50 km and continues northwards for about 13 km before abruptly changing strike to a SSW trend, which coincides with the hinge area of a tight regional-scale fold (Figure 3).

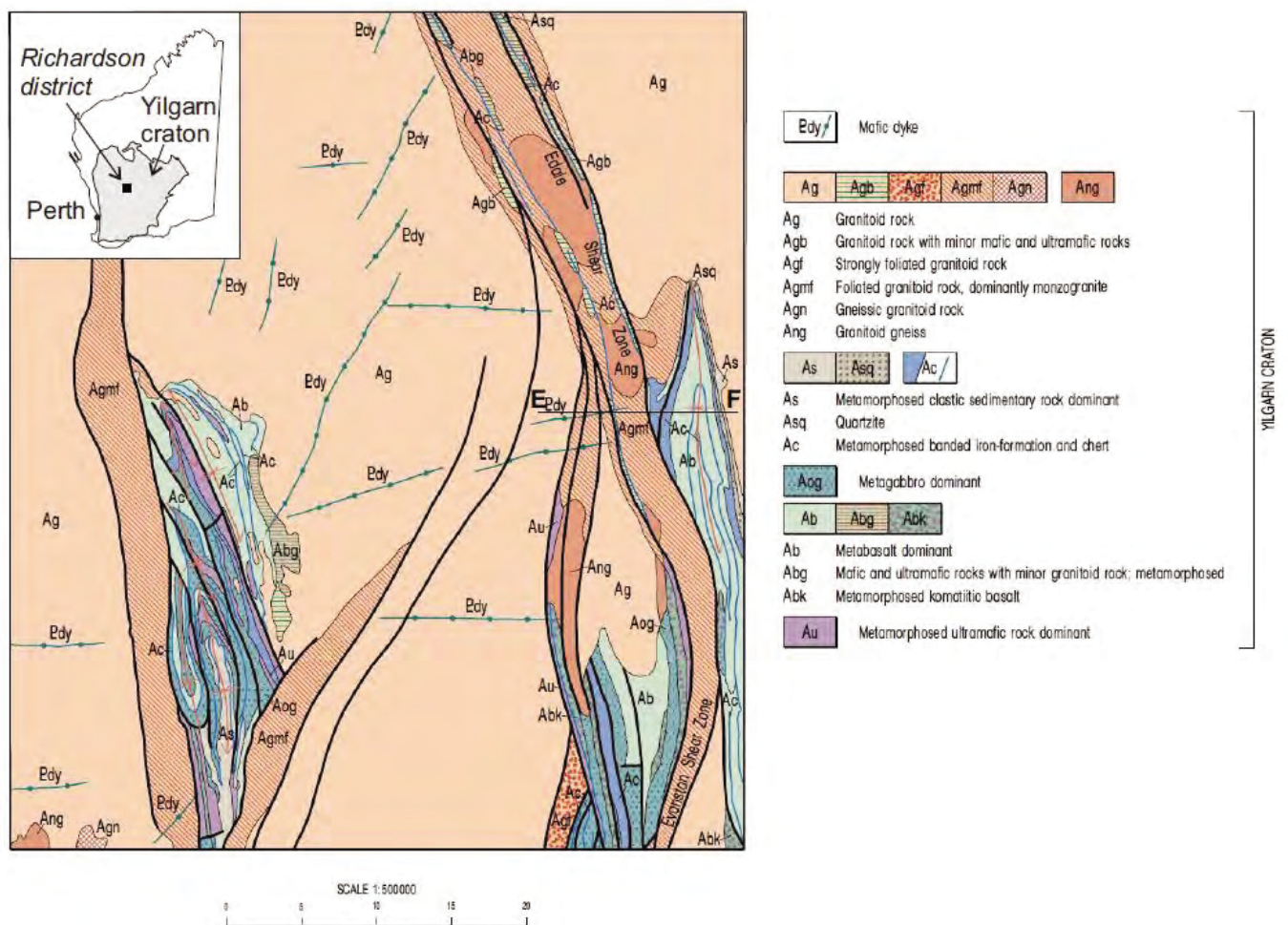


Figure 3 Solid geology map of Richardson 1:100,000 scale, Geological Survey of Western Australia map sheet, showing major lithological associations and structural relationships (modified after Chen, 2004)

The range comprises multiple BIF and chert macrobands that are between 1-100 m thick, and are flanked by poorly-exposed weathered mafic igneous rocks, with sandstone and siltstone exposed sporadically along the eastern margin of the range. Outcrop is rare and poorly expressed in the plain to the west of the range where

intensely weathered mafic igneous rocks dominate; 20 m-high, 3 to 60 m-wide, exposures of BIF and banded chert define NNW- and NNE-trending ridges in these western areas. All rocks in the Mount Richardson prospect are metamorphosed to upper greenschist facies (Figure 4).

The symmetric regional distribution of BIF and mafic igneous rocks suggests these units mark the hinge area of a regional fold. In the Mount Richardson prospect, macroscopic fold hinges defined in BIF units are preferentially exposed along ridges within the range, with some of the narrow fold limbs commonly faulted and truncated. The BIF macrobands cannot be easily separated based on their primary textures or compositions, the macrobands comprise alternating mesobands (1-30 mm thick) of primary iron oxides and quartz. The iron oxide bands represent up to 40 vol. % of least-altered BIF, although BIF may grade into banded chert along strike away from the Mount Richardson prospect (Duuring 2013).

Fine-grained mafic igneous rocks exposed along the margins of BIF and chert ridges are commonly intensely weathered and weakly to intensely schistose. Grain size of these rocks varies from basalt to gabbro, some fresh examples include komatiitic basalt, high Mg tholeiitic basalt, and high Fe tholeiitic basalt comprises primary igneous plagioclase, primary and metamorphic amphiboles, and metamorphic and hydrothermal chlorite and epidote. Intense weathering and deformation is located at the margin of BIF macrobands. A 1-10 m thick, blanket of poorly sorted transported sediment covers weathered mafic rocks and BIF along the flanks of most ridges in the Mount Richardson prospect.

Current geological interpretations indicate main controls for high-grade iron ore at Mount Richardson are: (1) fold-thickened BIF, (2) repeated reactivation of early shear and/or specularite veins and alteration. These early hypogene alteration zones are important in terms of changing the primary mineralogy (and some physical properties) of primary BIF through the formation of coarse-grained magnetite and talc. This hypogene stage did not remove all the silica from the altered BIF. Later supergene alteration played an important role in removing the silica gangue minerals from hypogene-altered BIF, through the dissolution of quartz and/or the replacement of quartz and talc by supergene goethite minerals (Duuring 2013).

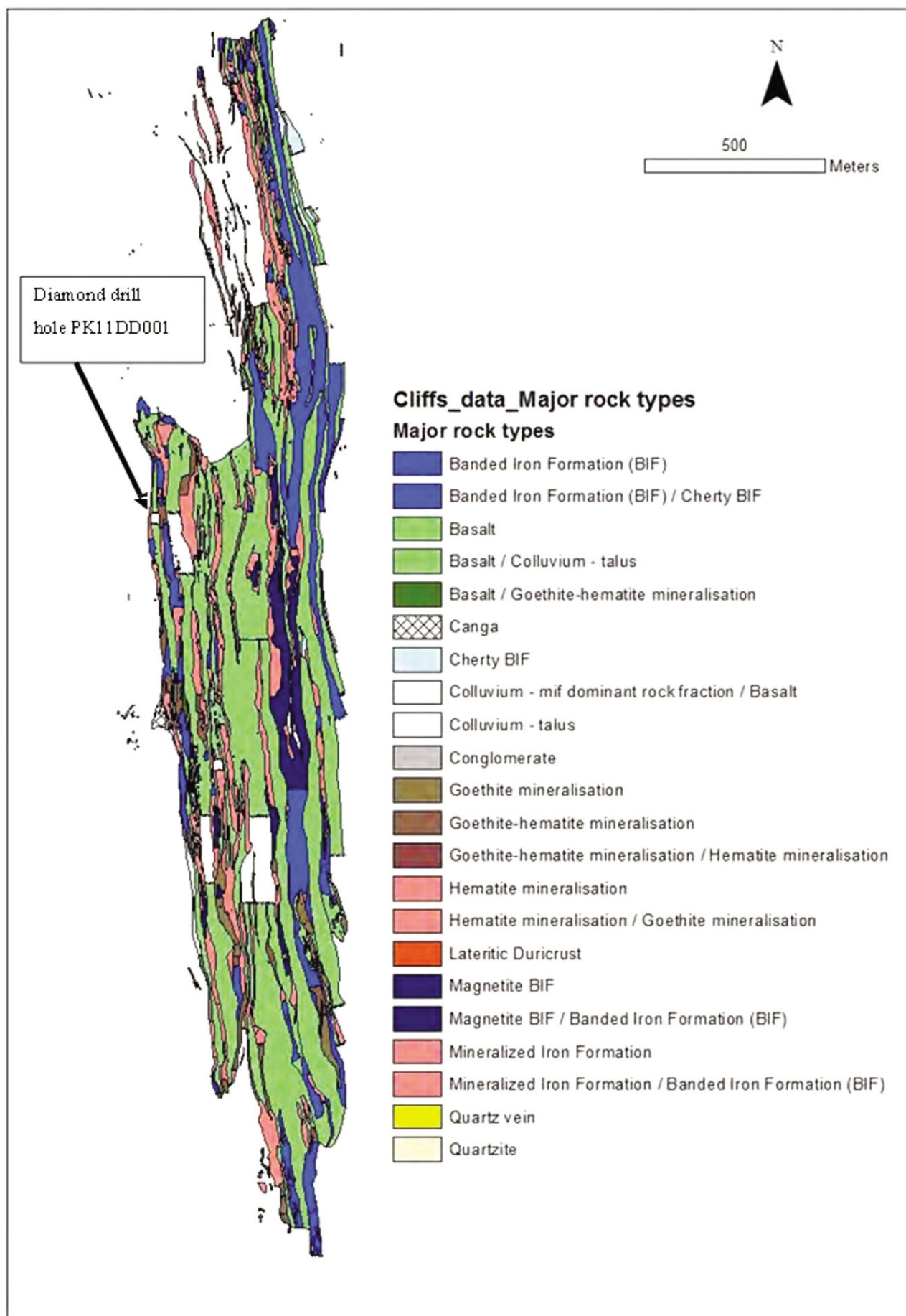


Figure 4 Solid geology map for the Mount Richardson prospect showing the distribution of rock types and alteration zones within BIF (Duuring and Hagemann 2013, modified after mapping by Cliffs Natural Resources).

PETROGRAPHY OF LEAST-ALTERED ROCK TYPES OBSERVED IN DRILL HOLE PK11DD001

Rock types at Mount Richardson are universally affected by metamorphism, hypogene alteration, and/or supergene alteration. Representative examples of least-altered BIF and mafic igneous rocks are described below based on core logging observations recorded by the author. Lithological rock types, mineral abundances, geochemistry and alteration zones are graphically portrayed in the drill hole log in Figure 5 and Appendix 5.

BIF

Banded Iron Formation displays 0.5 to 25 mm-thick, alternating bands of quartz and Fe oxide minerals (Figure 7). The quartz-rich bands comprise mainly (80 vol%), ~300 μm -diameter, anhedral recrystallised quartz grains, with minor disseminated euhedral magnetite (10 vol%) and cryptocrystalline disseminated hematite (10 vol%). Magnetite crystals are moderately oxidised to martite.

Mafic igneous rocks

Mafic igneous rocks are green, fine- to coarse-grained, and comprise amphibole (25 vol%), chlorite (20 vol%), pyroxene (15 vol%), plagioclase (15 vol%), biotite (10 vol%), with minor white mica (5 vol%), carbonate minerals (5 vol%) and serpentine (5 vol%) (Figure 8). Primary igneous amphibole, pyroxene, plagioclase (and possibly olivine) are altered by metamorphic chlorite, epidote, white mica and serpentine. Amphibole and pyroxene grains up to 5 mm long are locally aligned and define a N-trending, steeply-dipping foliation in the rock (Figure 8e).

Transported sediment

BIF and mafic igneous rocks are covered by about 2 m of moderately cemented transported material (Figure 6). This detrital unit is red/brown, massive, and poorly sorted, with grain sizes ranging from 1 to 30 mm. Fragments of BIF and mafic igneous rocks are angular to sub-rounded, up to 1 cm in diameter, and cemented by very fine-grained (<1 mm) goethite and kaolinite.

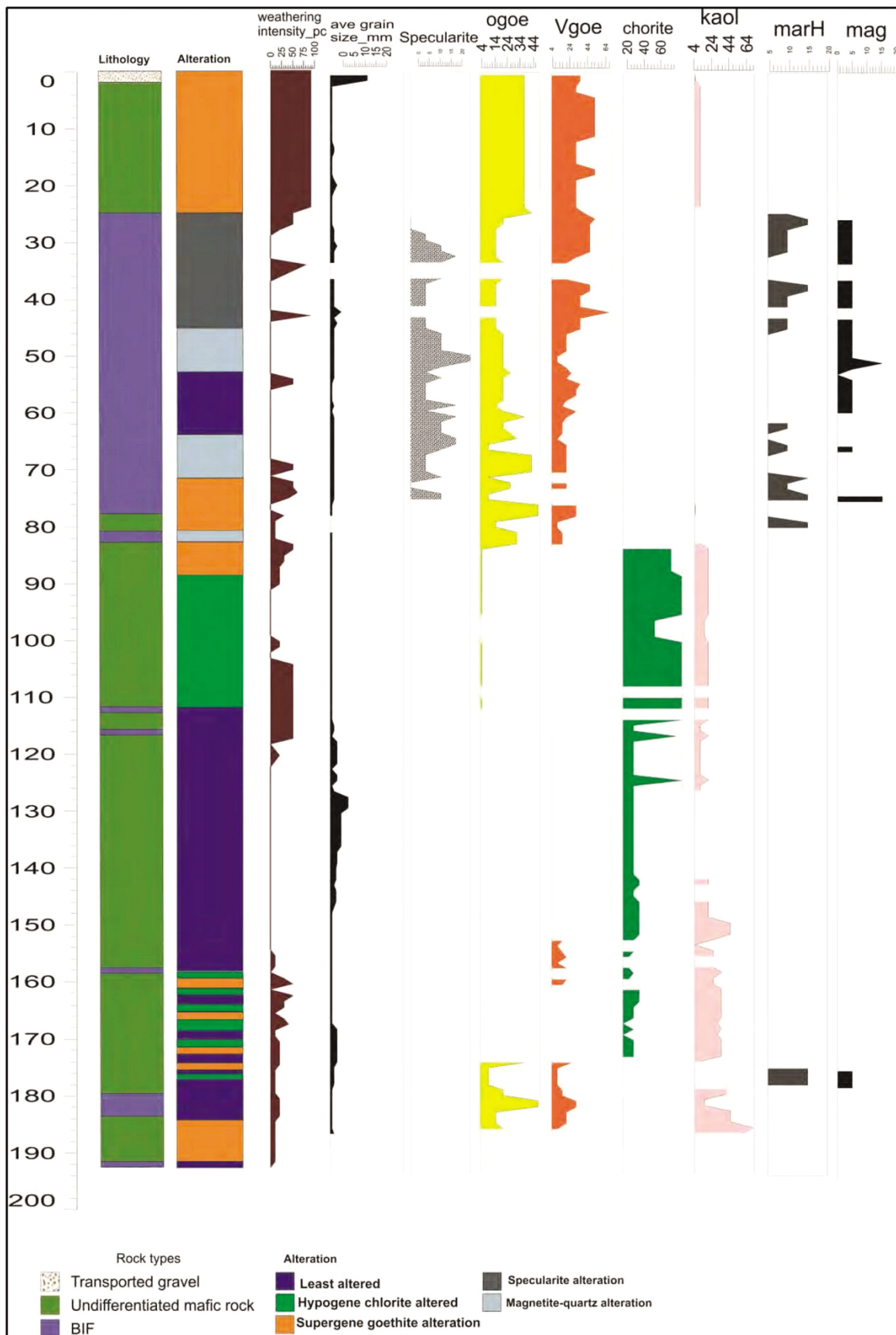


Figure 5 Graphic portrayal of data derived from conventional logging. Depths in metres below surface are shown on the left-hand margin. Abbreviations: ogoe, ochreous goethite; Vgoe, vitreous goethite; kaol, kaolinite; marH, martite; mag, magnetite.

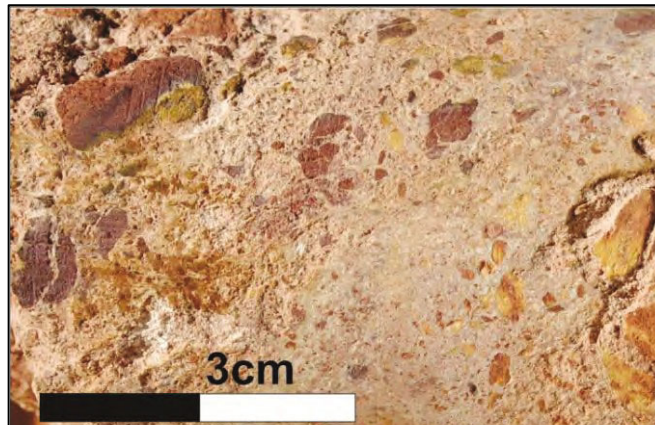


Figure 6 Transported sediment (observed at 1.5 m depth PK11DD001).

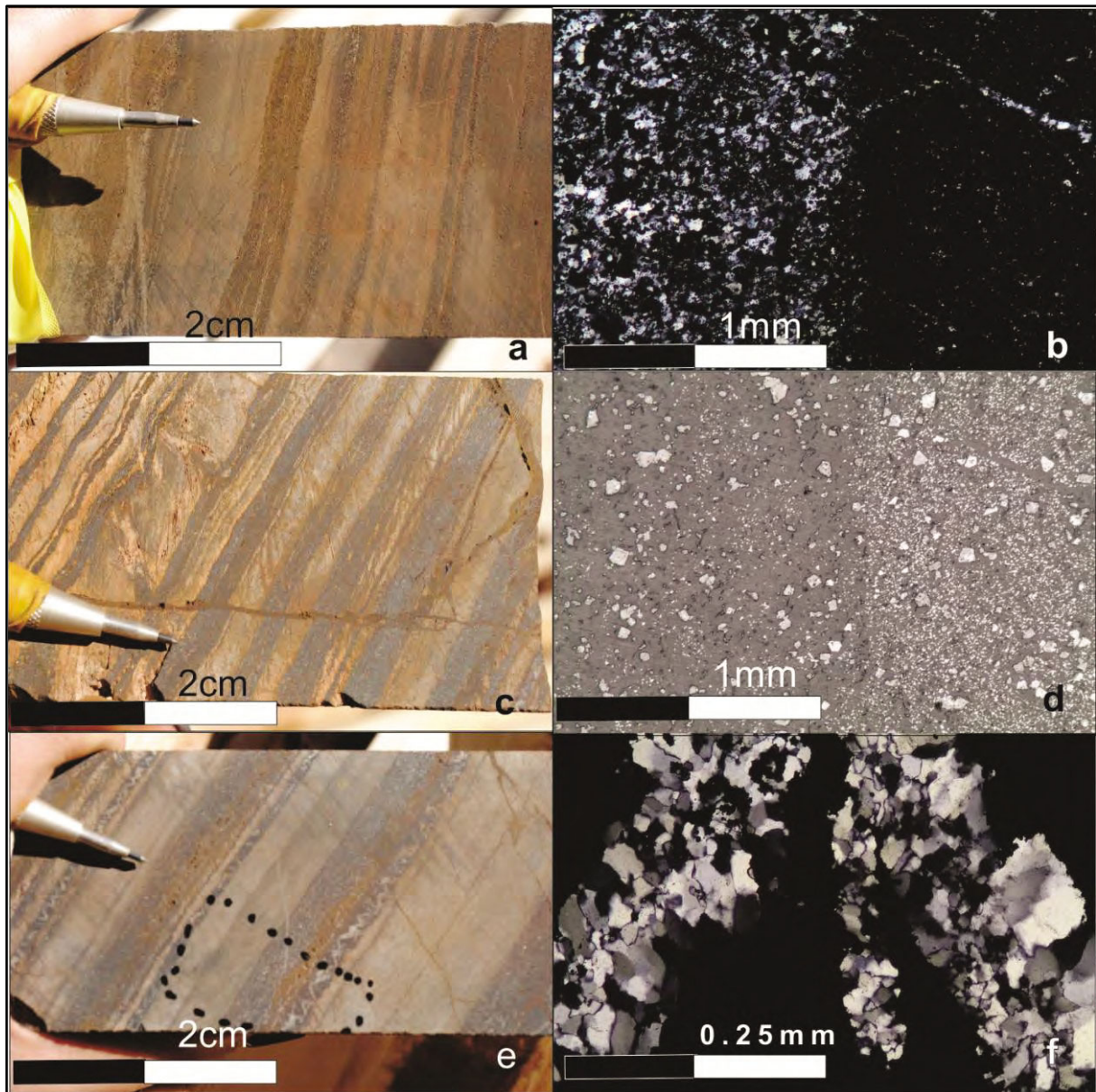


Figure 7 Least-altered BIF samples and thin sections photos (a) Least-altered BIF hand specimen sample LCMR10 at 55.5 m depth, (b) Thin section photo at 5Xmag reflected light in cross polarised light of LCMR10 showing the silica rich band on the left and iron oxide rich band on the right, (c) LCMR09 geochemistry sample of least-altered BIF at 48.5 m depth, (d) LCMR10 thins section photo at 5Xmag, polarised light showing silicia-rich bands and iron oxide-rich bands under transparent light, (e) LCMR09 thin section sample of iron oxide band textures at 48.5 m depth (f) recrystallised quartz band texture growths LCMR09 under 20Xmag reflected light, cross polarised.

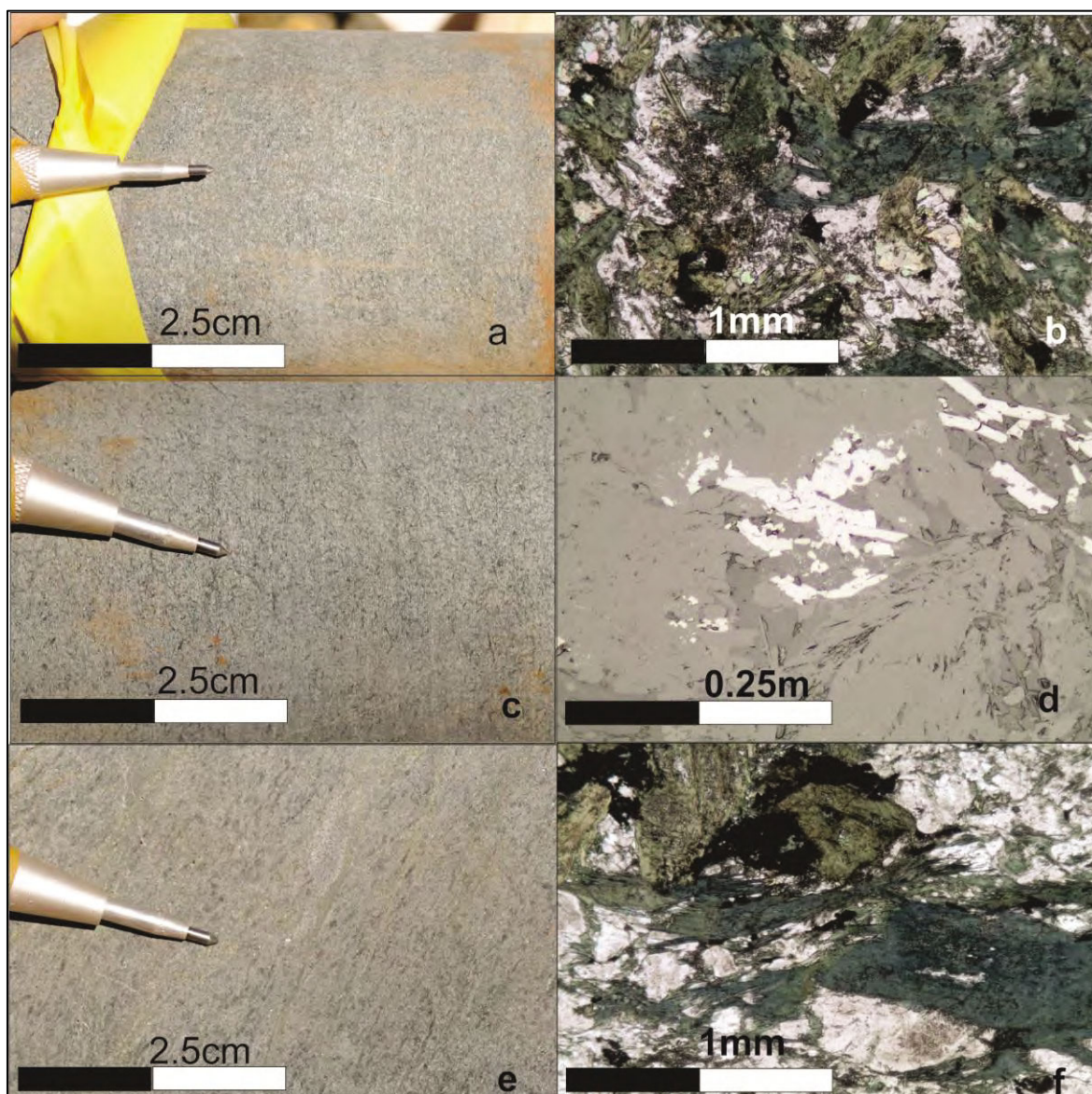


Figure 8 Least-altered mafic igneous rock, gabbro (a) Least-altered sample LCMR21 at 127.5 m depth (b) thin section LCMR22 under 5Xmag, reflected polarised light showing mineralogy of least-altered mafic rock, (c) Least-altered sample LCMR23 at 153 m depth (d) thin section LCMR22 under reflected polarised light 20Xmag showing iron oxide minerals found in least-altered mafic rock, (e) Least-altered sample LCMR22 at 134 m depth, showing foliation of dark amphibole minerals, (f) thin section LCMR22 under 40Xmag reflected polarised light, least-altered mineralogy and iron oxide mineral growths.

HYDROTHERMAL ALTERATION OF BIF AND MAFIC IGNEOUS ROCKS

Conventional diamond drill hole logging techniques and microscopy were used to identify the key mineralogical and textural changes in hypogene- and supergene-altered BIF and mafic igneous rocks at Mount Richardson.

BIF

STAGE ONE HYPOGENE ALTERATION: MAGNETITE-QUARTZ

Several BIF macrobands intersected by hole PK11DD001 record early hypogene magnetite and quartz replacement of primary quartz-magnetite bands. The location of these <10 m-thick, hypogene alteration zones coincides with the occurrence of brittle-ductile shear zones cutting BIF. These alteration and deformation zones are located parallel to the contact between BIF and mafic igneous country rocks; positioned in the middle of the BIF macrobands, or immediately along some contacts with the country rocks (Figure 5). Within these magnetite-quartz alteration zones, primary bands are moderately (<70 %) replaced by disseminated euhedral hypogene magnetite grains, with crystalline hypogene quartz surrounding the magnetite grains, or occurring as mineral inclusions. Primary banding is mostly replaced by a massive texture defined by disseminated magnetite, as well as some micro-veins of magnetite-quartz that occur parallel and perpendicular to BIF microbands (Figure 9). At the lower-most contact between BIF and mafic igneous country rocks, a <2 m-thick magnetite±quartz ductile shear zone is defined by massive to weakly schistose magnetite, rather than disseminated magnetite.

STAGE TWO HYPOGENE ALTERATION: SPECULARITE AND MARTITE

Primary quartz-magnetite bands and hypogene magnetite-quartz alteration mineral assemblages are locally replaced by specularite wall rock alteration zones and widespread martitisation (i.e. pseudomorphic replacement of magnetite by hematite). These alteration zones are structurally controlled and are most intensely developed in BIF along lithological contacts and areas of existing hypogene magnetite-quartz alteration zones (Figure 5). The disseminated fine-grained crystals of specularite impart

a massive texture to these alteration zones and a marked decrease in the magnetism of the least-altered and hypogene magnetite-quartz altered BIF. Specularite crystals are associated with hydrothermal quartz (Figure 9b).

STAGE THREE SUPERGENE ALTERATION: GOETHITE

Least-altered and hypogene-altered BIF are locally affected by supergene alteration. The intensity of supergene alteration generally decreases with depth, but intensifies within 5 m of lithological contacts with mafic igneous country rocks, or where BIF is cut by discrete 1-2 m-thick, fault zones (Figure 5). Supergene-altered BIF is red, brown, or yellow depending on the intensity of alteration and the proportion of supergene hematite, vitreous goethite, and ochreous goethite. Primary and hypogene minerals and textures are preserved in weak to moderately supergene-altered BIF. In these rocks, primary quartz-rich bands are replaced by cryptocrystalline hematite and goethite supergene minerals. Primary magnetite-rich bands and disseminated euhedral hypogene magnetite grains are completely replaced by hematite or goethite (Figure 10b, d). Goethite \pm quartz veins (Figure 10f) commonly cut hypogene-altered bands. Intensely supergene-altered BIF displays the destruction of pre-existing textures, the complete replacement of primary and hypogene minerals; the resultant rock is massive and porous (<15 vol% cavities).

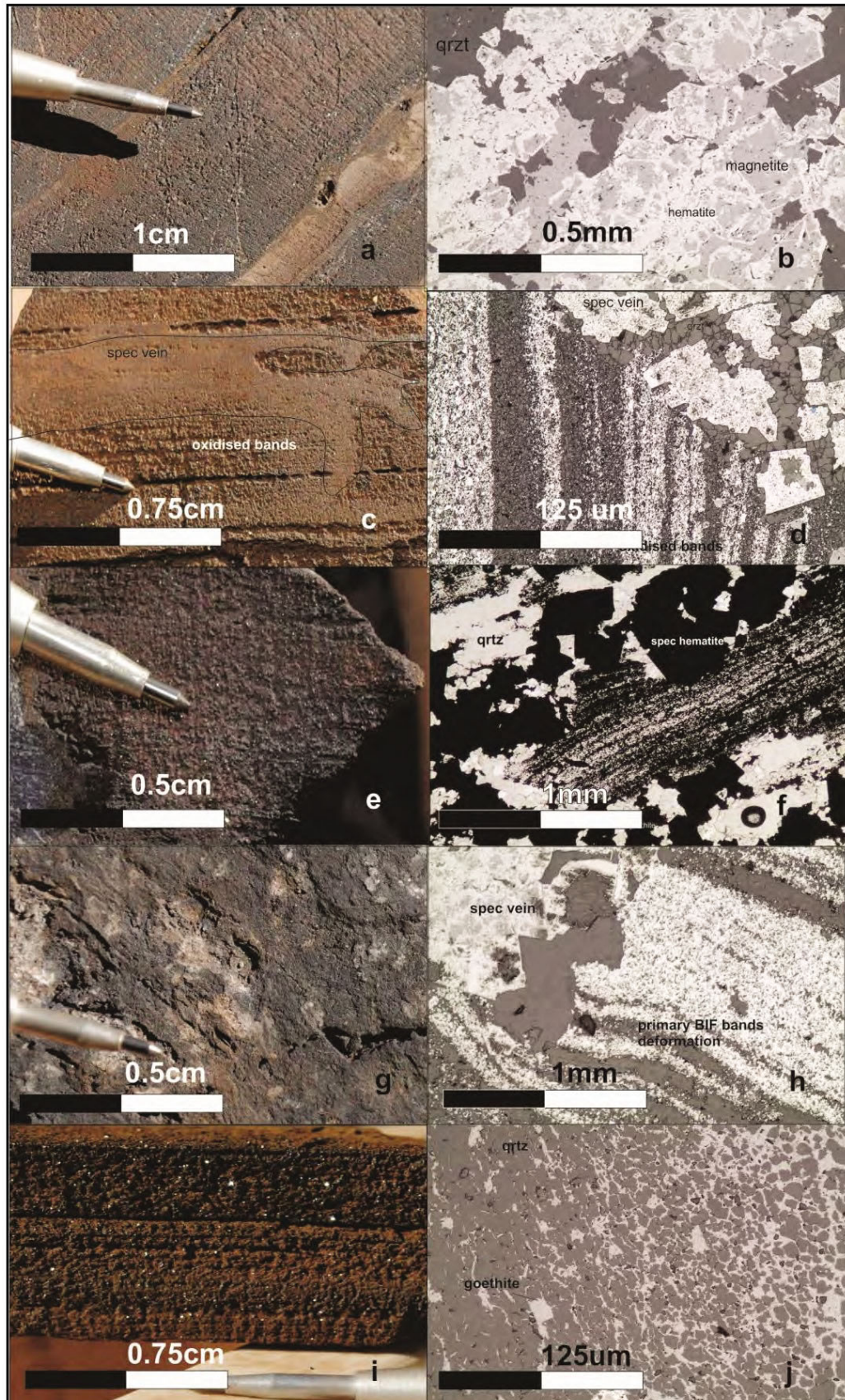


Figure 9 Hypogene alteration in BIF (a) sample LCMR08 at 46.5 m depth, hypogene-altered BIF original banding, (b) thin section LCMR06 in transmitted polarised light at 10Xmag, disseminated hematite textures (c) sample LCMR04 at 32.9 m depth, coarse grained supergene-modified, hypogene-altered BIF (d) LCMR07 transmitted polarised light at 40Xmag, crosscutting relationship between specular hematite vein and primary BIF bands (e) sample LCMR05 at 38 m depth, dark hypogene-altered BIF at lithological contact (f) LCMR07 reflected polarised light at 5Xmag, infill of specular hematite vein in oxidised primary BIF (g) sample LCMR07 at 46 m depth, hypogene-altered BIF (h) LCMR08 transmitted polarised light at 10Xmag, deformation of primary bands by hypogene vein infilling BIF (i) Coarse grained hypogene alteration, specular hematite (j) thin section LCMR06 in transmitted polarised light at 10Xmag goethite infill in silica-rich bands of hypogene-altered rock.

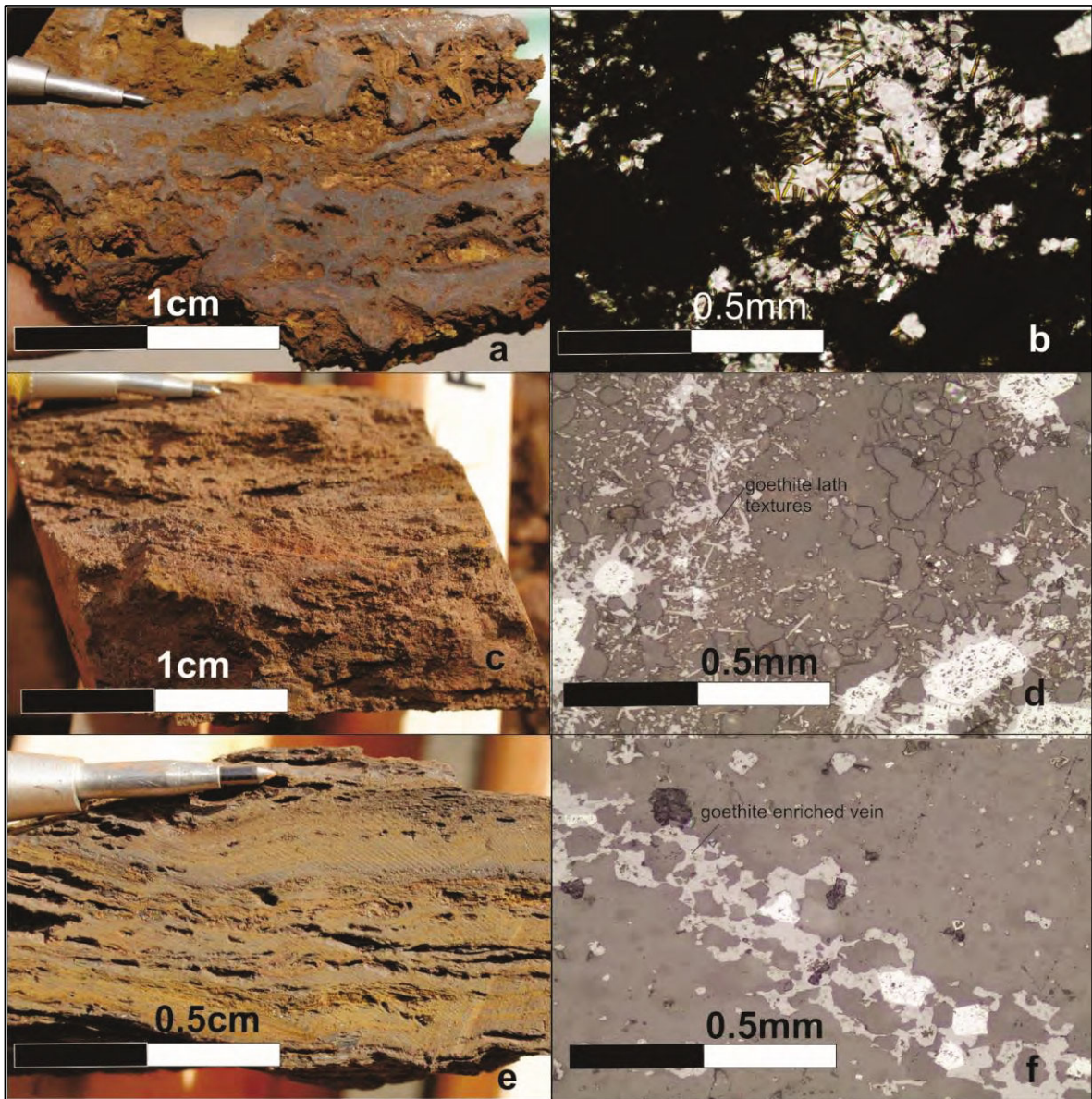


Figure 10 Supergene-altered BIF; (a) Highly porous supergene-altered BIF (b) Thin section LCMR09 20Xmag, reflected polarised light, goethite enrichment textures (c) Sample LCMR03 at 32.5 m depth, supergene-altered BIF (d) Thin section LCMR09 20Xmag, transmitted polarised light, goethite enrichment textures (e) Sample LCMR02 26 m depth narrow ore zone of supergene-altered BIF (f) Thin section LCMR09 20Xmag, transmitted polarised light, late supergene enrichment of specular hematite vein.

Mafic igneous rocks

Mafic igneous rocks display an obvious spatial zonation in mineral abundances and texture with proximity to contacts with hypogene-altered BIF. Individual hypogene alteration mineral assemblages were not detected in the mafic igneous rocks. Consequently, the section below describes hypogene-altered mafic igneous rocks from distal zones to proximal zones.

Distal hypogene alteration zones in mafic igneous rocks located more than 63 m away from the contact with specularite-altered BIF (i.e. at drill hole depths of 129 to 152 m), are dark green and coarse-grained. The rocks display weak (< 10 %) replacement of primary igneous amphibole, pyroxene and biotite by hypogene chlorite.

Intermediate hypogene alteration zones, located between 40 and 63 m from specularite-altered BIF (i.e. at drill hole depths of 115 to 129 m) are blue-green and medium-grained (Figure 11e, g). These rocks display primary igneous amphibole, pyroxene and biotite that are moderately (<30 %) replaced by hypogene chlorite.

Proximal hypogene alteration zones in mafic igneous rocks occur up to 26 m from specularite-altered BIF (i.e. at drill hole depths of 81 to 115 m). Fresh examples of proximal hypogene-altered rocks are light-green, very fine-grained, and comprise mainly hypogene chlorite (90 %). Proximal hypogene alteration zones rocks are intensely supergene goethite-hematite altered and schistose within 10 m of all contacts with BIF (Figure 11a, c).

Supergene-altered mafic igneous rocks occur from near-surface to depths of about 170 m and along the deformed lithological contacts with BIF. The rocks are red-brown, fine-grained and soft. Primary igneous, metamorphic and hypogene minerals are replaced by very fine-grained goethite, hematite, kaolinite and quartz. Primary textures and foliation are weakly preserved in weak to moderately altered mafic igneous rocks (Figure 11 b, d).

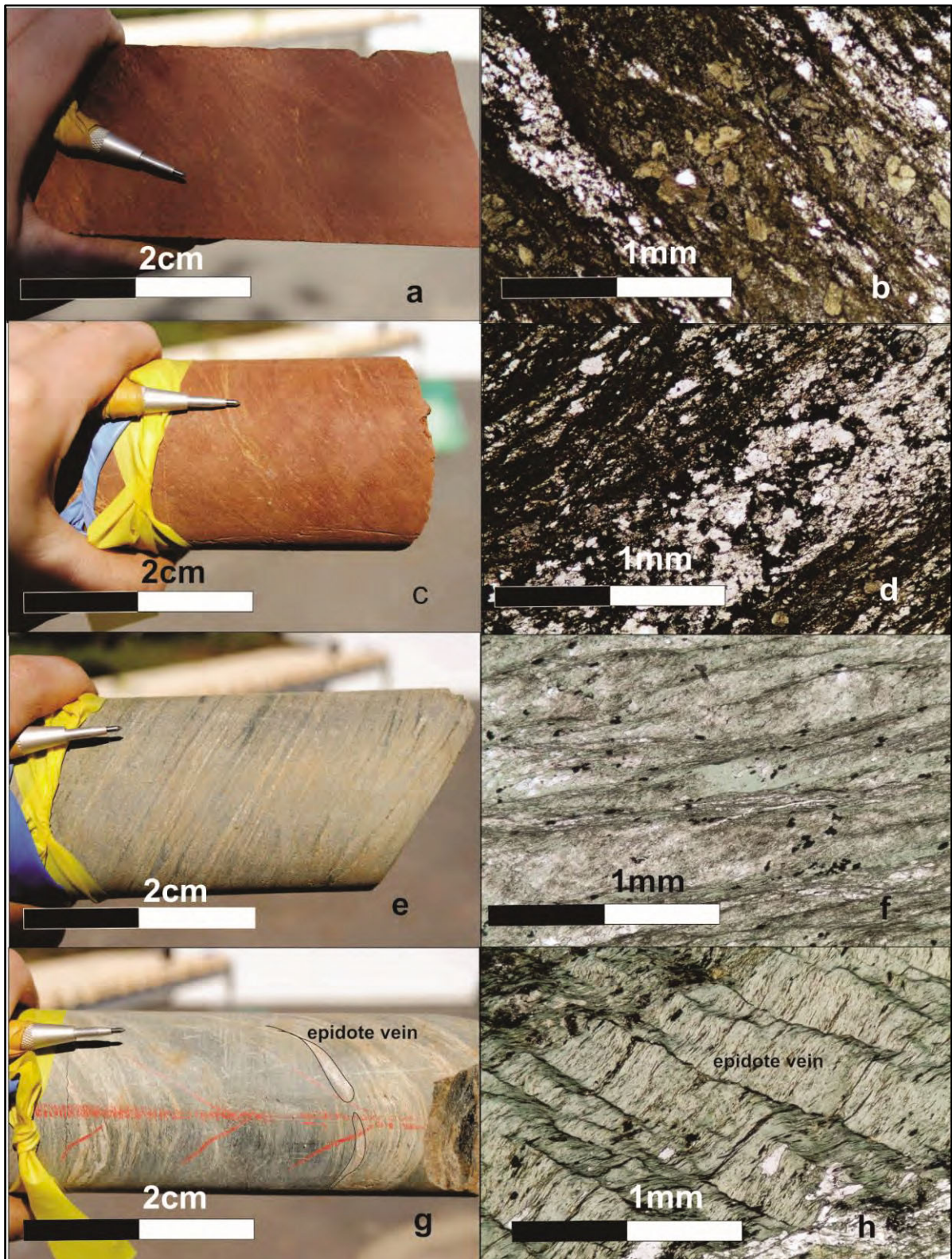


Figure 11 Supergene and hypogene-altered mafic igneous rocks (a) sample LCMR17 supergene-altered mafic rock near BIF contact (b) thin section LCMR17 of supergene mafic rock at 5X mag in reflected polarised light (c) sample LCMR18 supergene-altered mafic rock with strong foliation textures (d) thin section LCMR18 of supergene mafic rock at 5X mag in reflected polarised light (e) sample LCMR19 hypogene altered mafic rock (f) sample LCMR19 hypogene altered mafic rock textures at 5X mag in reflected polarised light (g) sample LCMR19 hypogene-altered mafic rock with epidote veining (h) thin section LCMR19 epidote vein deformation textures from wall rock foliation in mafic rock at 5Xmag in reflected polarised light.

GEOCHEMISTRY OF ALTERED BIF AND MAFIC IGNEOUS ROCKS

Least-altered BIF

Three representative samples of least-altered BIF comprise mainly SiO_2 (47.41 ± 3.42 wt %; quoting the 1σ standard deviation) and $\text{Fe}_2\text{O}_{3\text{Total}}$ (50.68 ± 2.92 wt %). All other major oxide elements, TiO_2 , Al_2O_3 , MnO , MgO , CaO , Na_2O , K_2O , and P_2O_5 , do not exceed 0.2 wt%. Trace elements are uniformly low (< 10 ppm), with the exceptions of Mn (288 ± 62 ppm), Cr (22 ± 2 ppm), Ni (19 ± 17 ppm), Cu (19 ± 4 ppm), and Co (13 ± 7 ppm). Rare Earth Element values for least-altered BIF are very low (ranging from 0.09 to 5.9 ppm). REE values that are normalised against the chondrite values of McDonough and Sun (1995) define a negative slope, indicating enrichment in Light Rare Earth Elements (LREE) relative to Heavy Rare Earth Elements (HREE). The REE trend for the least-altered BIF at Mount Richardson overlaps the trend for least-altered BIF in the Yilgarn Craton (Gole 1981). The positive Eu anomaly for least-altered BIF from Mount Richardson is most likely the product of the interaction between heated hydrothermal fluids and seawater during BIF deposition (Dymek and Klein 1988, Danielson et al. 1992). Appendix 2 shows geochemical data for all rock samples analysed at Mount Richardson.

Hypogene-altered BIF

Binary plots for $\text{Fe}_2\text{O}_{3\text{Total}}$ wt% versus major element oxides and trace elements are shown in Appendix 7. The plots investigate if there are any general relationships between high-grade iron ore and other elements at Mount Richardson. The most obvious trend is the inverse relationship between $\text{Fe}_2\text{O}_{3\text{Total}}$ and SiO_2 . Geological processes that encourage the net removal of SiO_2 and/or the addition of $\text{Fe}_2\text{O}_{3\text{Total}}$ are a prerequisite for iron ore genesis. However, there are also weak to moderate positive correlations between $\text{Fe}_2\text{O}_{3\text{Total}}$ and Al_2O_3 , TiO_2 and P_2O_5 . However, these positive elemental trends do not take into account apparent enrichment via volume changes in altered BIF.

The geochemical mass balance analysis method (first described by Gresens 1967 and modified by Grant 1997, Grifkins et al. 2005) is used to evaluate net gains and losses in mobile elements in altered BIF and mafic igneous rocks at Mount Richardson. The technique uses immobile elements (Ga, Ge, Nb, TiO_2 and Zr for BIF; Dy, Ho, Lu, Nb, Sm, TiO_2 , Y, Yb and Zr for mafic igneous rocks) to compensate for volume changes in

altered rocks. The results of the mass balance analysis are tabulated in Appendix 5. In these calculations, the averages for least-altered BIF or mafic igneous rocks are compared against the averaged values for hypogene- and supergene-altered variants.

Relative to least-altered BIF, stage 1 and 2 hypogene-altered BIF samples are depleted in SiO_2 (containing an average of 23.00 ± 12.03 wt %; i.e. a change of -30%) and are enriched in $\text{Fe}_2\text{O}_{3\text{Total}}$ (72.20 ± 12.45 wt%; indicating a net gain of 104%). Enrichments in major oxide elements include MnO (1926%), Al_2O_3 (505%), and Na_2O (257%). Trace elements that display net enrichments of greater than 50 percent include Ag, As, Be, Be, Co, Cs, Cu, Ge, Li, Ni, Rb, Re, Sr, Ta, V, W, Zn, Sc and Y. Elements that display depletions of more than 20 percent include Bi, Cr and Pb. The LREE (La, Ce, Pr, Nd) are more enriched than the HREE in hypogene-altered BIF. Net gains and losses of hypogene-altered BIF are shown in Figure 12.

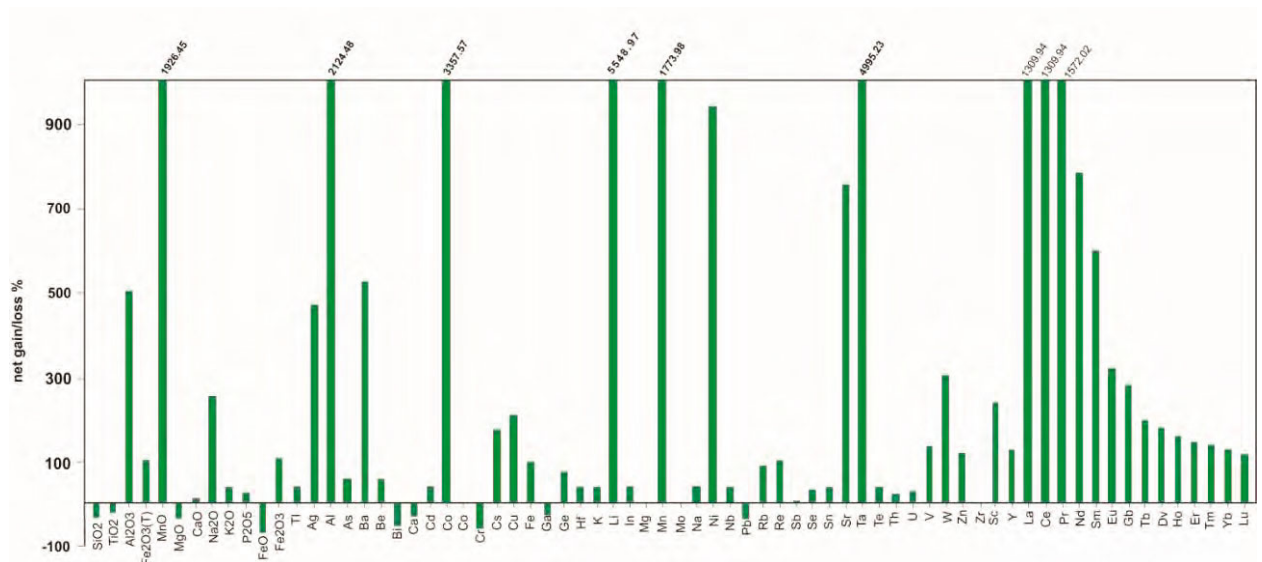


Figure 12 Calculated percentage net gains and losses of elements in hypogene-altered BIF relative to least-altered examples (after Grant, 1986).

Supergene-altered BIF

Binary plots that show $\text{Fe}_2\text{O}_{3\text{Total}}$ wt% compared with values for major element oxides and trace elements are presented in Appendix 8. Apart from an inverse relationship between $\text{Fe}_2\text{O}_{3\text{Total}}$ and SiO_2 , a strong positive relationship exists between $\text{Fe}_2\text{O}_{3\text{Total}}$ and Al_2O_3 . Additionally, a weak to moderate positive correlation occurs between $\text{Fe}_2\text{O}_{3\text{Total}}$ and Na_2O , K_2O and P_2O_5 .

Mass balance calculations for three representative examples of supergene-altered BIF indicate that these rocks are greatly depleted in SiO_2 (2.63 ± 0.94 wt%; i.e. a change of -94%) and enriched in $\text{Fe}_2\text{O}_{3\text{Total}}$ (86.85 ± 3.98 wt%; a net gain of 90%) compared with average values for least-altered BIF. Other major oxide elements that are enriched include MnO (3586%), K_2O (530%), Na_2O (372%) and Al_2O_3 (243%), with depletions in MgO (-21%). Trace elements that display an enrichment of greater than 50 percent include Ag, As, Ba, Be, Bi, Cd, Co, Cr, Cs, Cu, K, Li, Mo, Ni, Pb, Rb, Sb, Se, Sr, Ta, U, V, W, Zn, Zr, Sc and Y. Elements that display significant depletions (i.e. at least -20%) include Ga and Re. Rare Earth Elements are all enriched in supergene-altered BIF (>400% enrichment) (Figure 13).

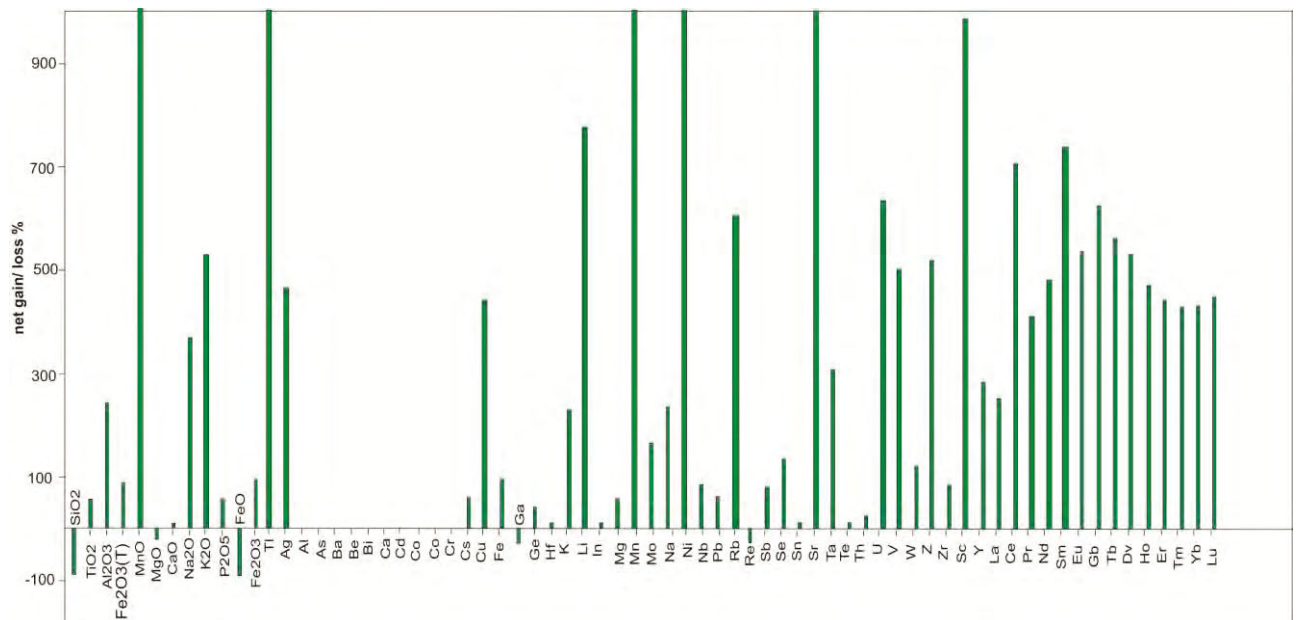


Figure 13 Calculated percentage net gains and losses of elements in supergene-altered BIF relative to least-altered examples (after Grant, 1986).

Least-altered mafic igneous rocks

Least-altered mafic igneous rocks contain mainly SiO_2 (55.07 ± 0.98 wt%), Al_2O_3 (11.87 ± 0.10 wt%), CaO (7.31 ± 2.31 wt%), Fe_2O_3 (4.96 ± 0.60 wt%), and MgO (3.45 ± 0.34 wt%). These rocks from Mount Richardson plot as andesite/basalt and Fe-rich tholeiitic basalts using the geochemical rock discrimination diagrams of Winchester and Floyd (1977) (Figure 14C) and Jensen (1976) (Figure 14D), respectively. Trace element concentrations for least-altered mafic igneous rocks are mostly less than 10 ppm for Ag, As, Be, Bi, Cd, Cs, Ge, Hf, Li, In, Mo, Nb, Pb, Rb, Re, Sb, Se, Sn, Ta, Te,

Th, U and W. Trace elements are up to 100 ppm for Ba, Co, Cr, Cu, Ga, Ni, Sr, Sc, and Y, with notable exceptions for V (187 ppm), Zn (132 ppm), Zr (105 ppm) and Mn (1393 ppm). Rare Earth Element abundances are greater in mafic igneous rocks than in BIF (i.e. greater than 0.99 ppm). Chondrite -normalised REE patterns for least-altered mafic igneous rocks have a positive slope indicating HREE-enrichment relative to LREE (Figure 14B).

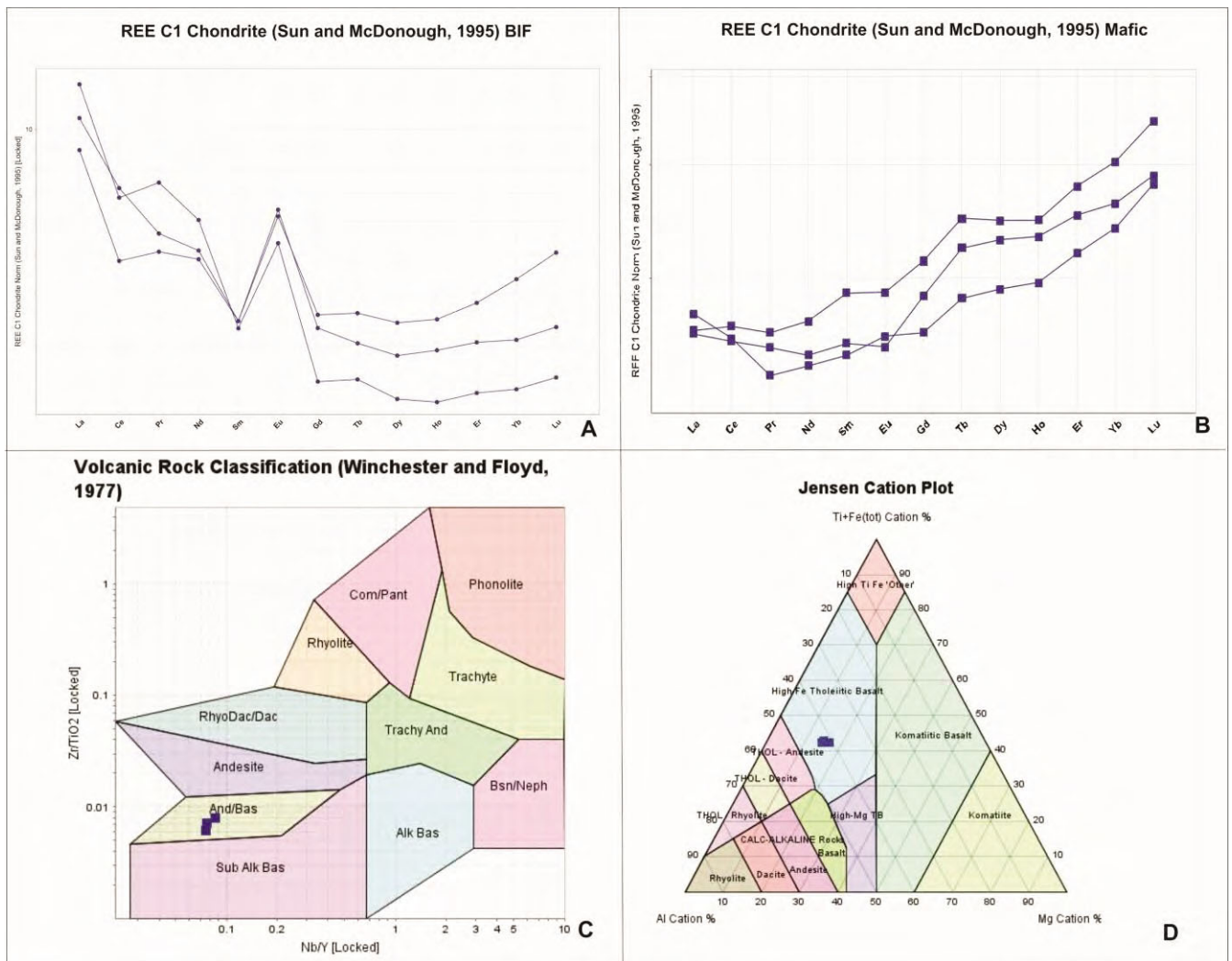


Figure 14 A) Winchester & Floyd (1977) REE plot showing chondrite-normalised data for least-altered BIF, (B) REE chondrite normalisation diagram for least-altered mafic igneous rocks, (C) volcanic rock classification diagram for least-altered mafic igneous rocks.

Intermediate alteration zones in mafic igneous rocks

Two samples of mafic igneous rocks were analysed in an intermediate zone, located between least-altered mafic rocks and proximal alteration zones along the contact with

specularite-altered BIF. These intermediate alteration zones are <30 percent altered by hypogene chlorite and are weakly (10 %) altered to supergene goethite and hematite.

Relative to average values for least-altered mafic igneous rocks, mafic igneous rocks in intermediate zones are enrichment in MgO (6.81 ± 0.57 wt%; i.e. a net gain of 163%). Major element oxides that show significant depletions include K₂O (-74%), Na₂O (-44%) and CaO (-24%). Trace elements that show significant enrichments (over 50%) include As, Bi, Cr, Cs, Cu, Ge, Li, Ni, Rb, Sb and W. Depletions of more than -20 percent include Ba, Cd, Mo, Re, Se, Sr, Te and U. Rare Earth Elements are relatively immobile (Figure 15).

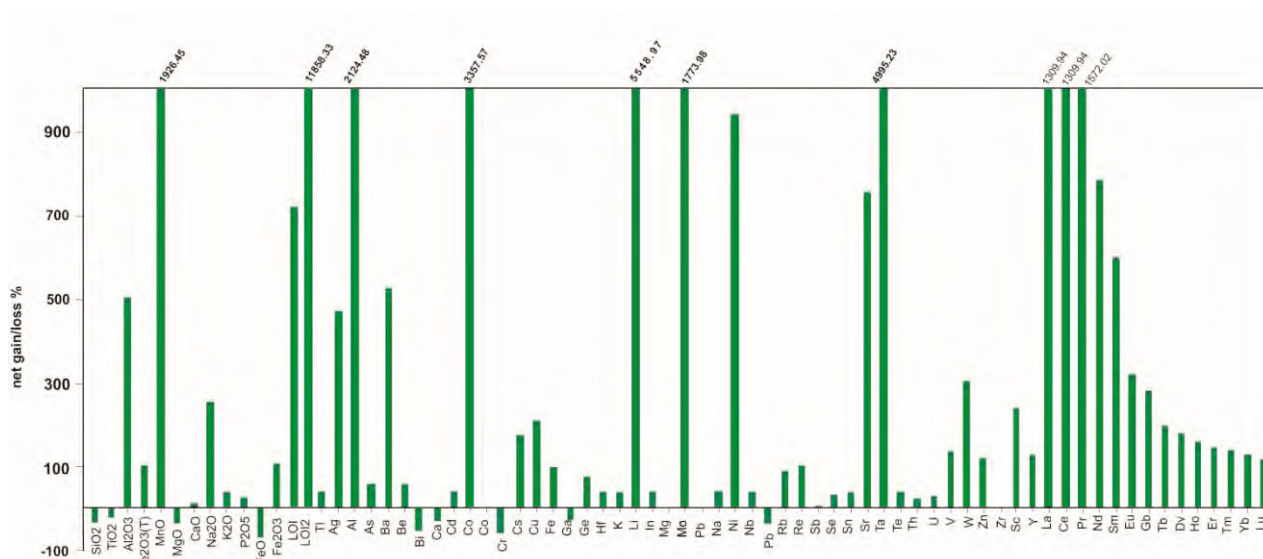


Figure 15 Mass balance net gain and losses of elements in intermediate (hypogene)-altered mafic igneous rocks relative to least-altered mafic igneous rocks (after Grant, 1986).

Proximal alteration zones in mafic igneous rocks

Two analysed samples of proximal hypogene alteration zones in mafic igneous rocks occur up to 26 m from specularite-altered BIF. Proximal hypogene alteration zones rocks are intensely (80 %) supergene goethite-hematite altered.

The supergene-modified, proximal alteration zones are enriched in SiO₂ (61.42 ± 0.25 wt%; i.e. a net gain of 31%) and Al₂O₃ (14.74 ± 0.01 wt%; 46%) Significant depletions in major element oxides include FeO (-99%), CaO (-99%), Na₂O (-98%), MgO (-96%), MnO (-75%), TiO₂ (-72%), K₂O (-61%) and P₂O₅ (-48%). Trace element enrichments of more than 50 percent include As, Ba, Be, Cr, Ge, Li, Ni, Rb and W. Depletions of more than -20 percent include Bi, Cd, Co, Cu, Ga, Hf, In, Mo, Nb, Pb, Se, Sr, Ta, Te, Th, Zn

and Zr. LREE are uniformly depleted, whereas HREE are enriched relative to least-altered mafic igneous rocks (Figure 16).

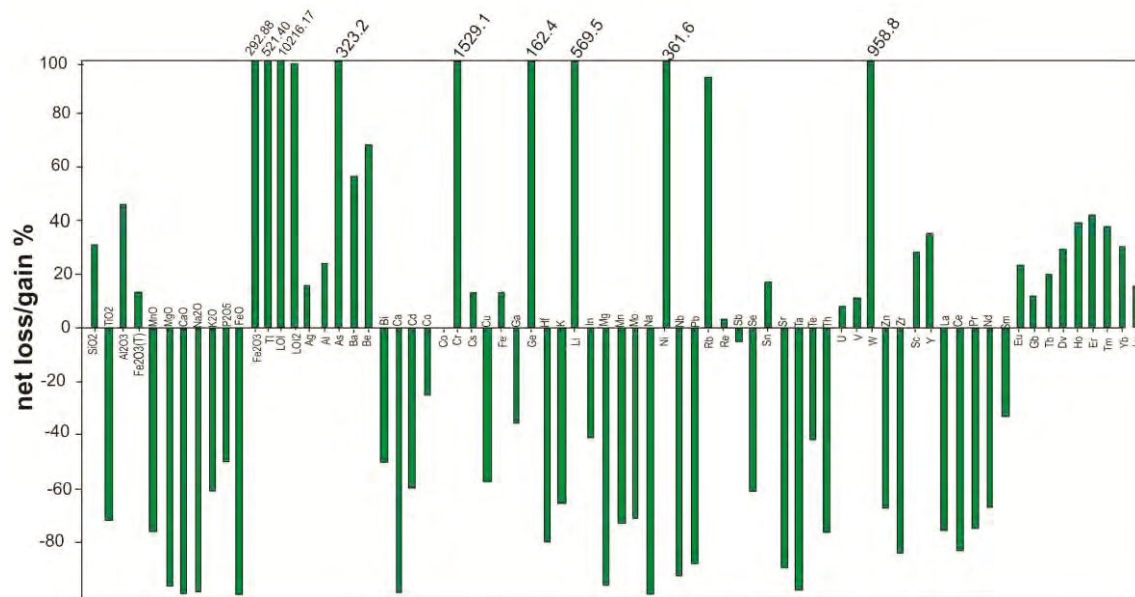


Figure 16 Mass balance net gain and losses for elements in proximal (supergene-altered) mafic igneous rocks relative to least-altered mafic igneous rocks (after Grant, 1986).

HYPER SPECTRAL DATA

Hyperspectral data for BIF and mafic igneous rocks obtained from the GSWA HyLogging™ system has been interpreted using the TSG™ commercial software. The section below describes the abundances and compositions of common minerals throughout the entire drill hole using pre-existing scripts developed by other studies (described in the methodology section and in more detail in Appendix 9). Figure 17 is a summary of mineral abundances based on core logging and hyperspectral data interpretation. Characteristic reflectance spectra for common minerals observed in this study are shown in Figure 18. This section also describes the development of a new script for the identification of specular hematite, which is used to map the distribution of hypogene specular hematite ore zones in BIF.

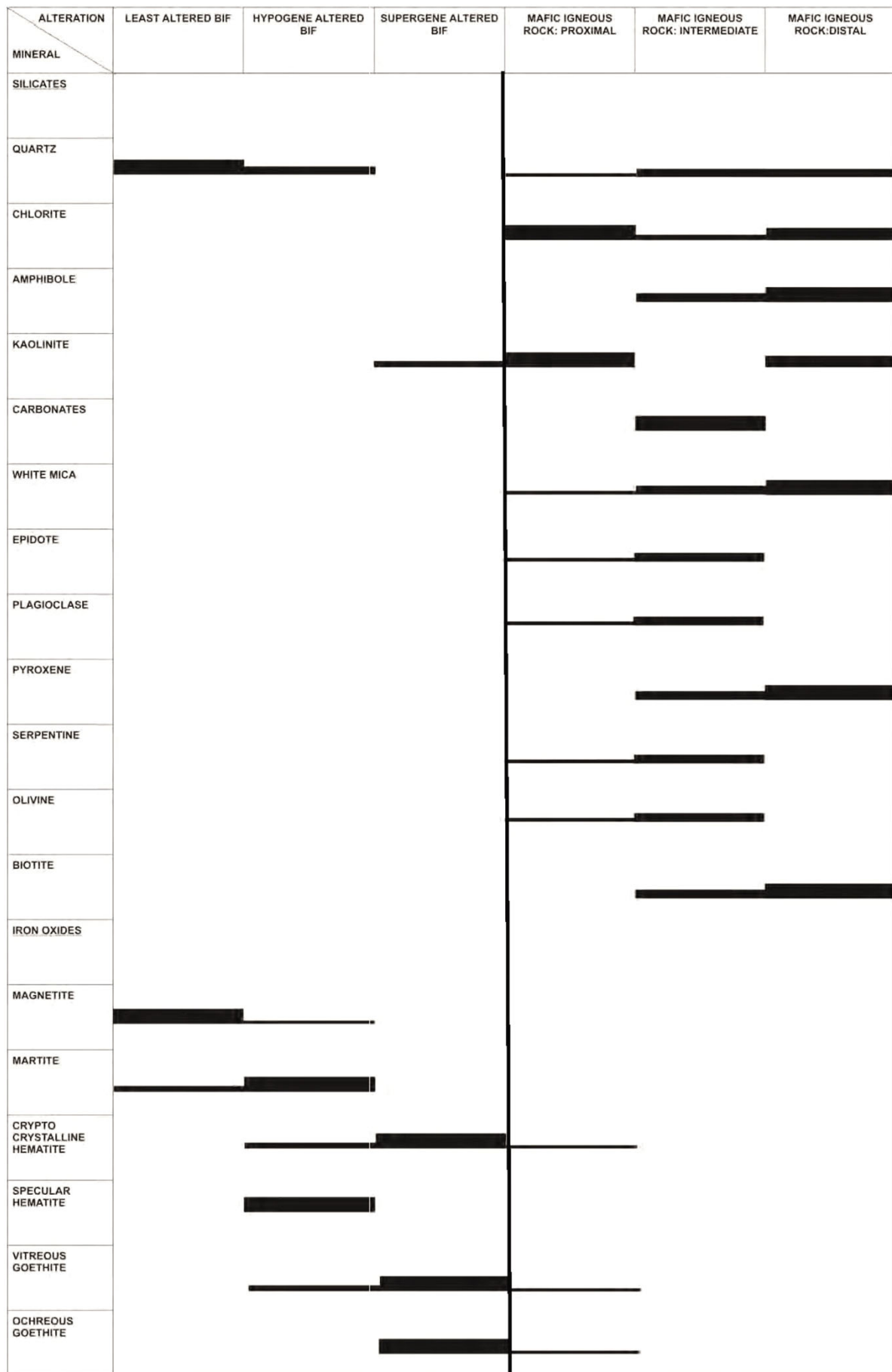


Figure 17 Mineral presence and relative abundances in BIF and mafic igneous rocks. Thick lines show major abundances, medium lines show moderate abundance and thin lines show minor abundance.

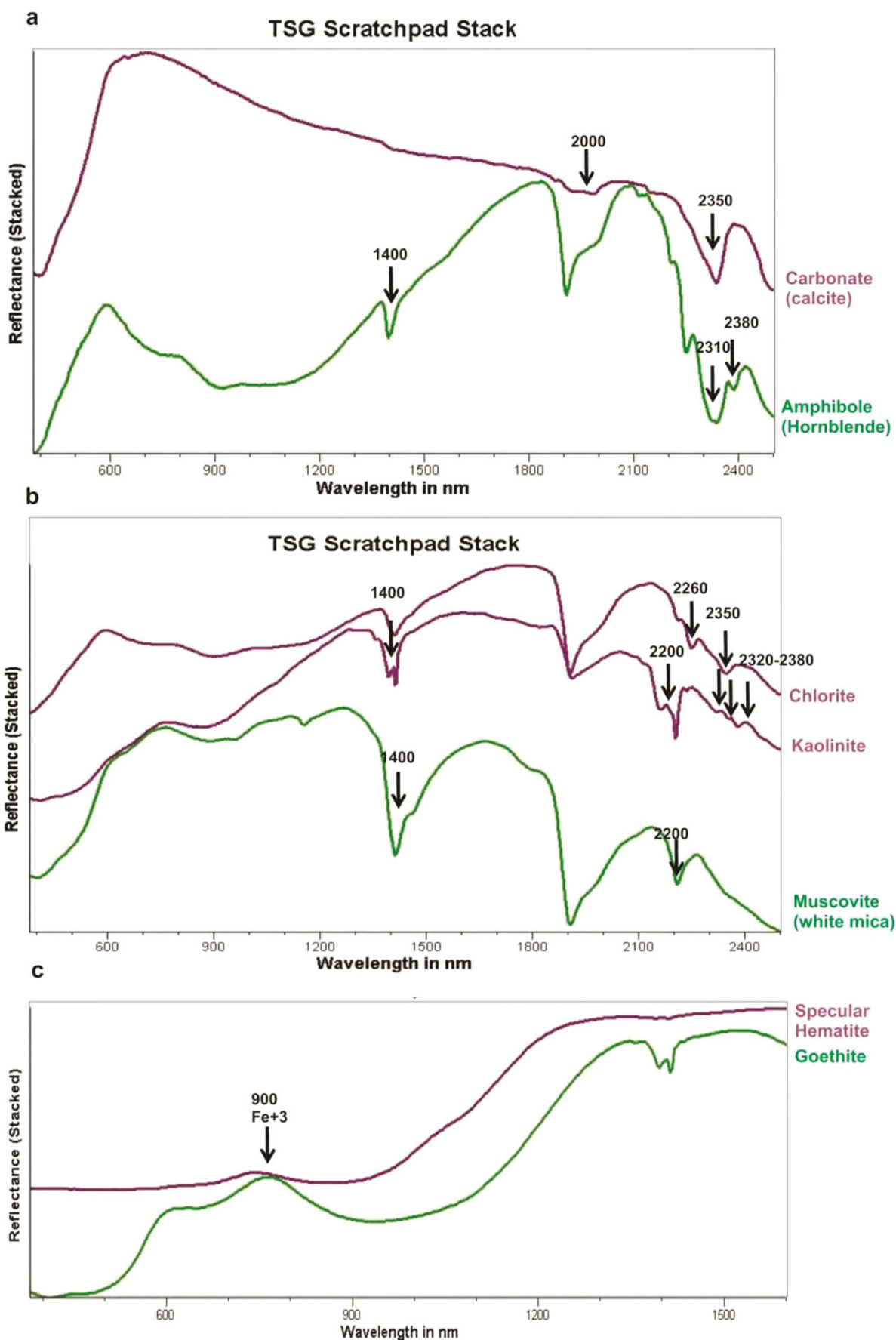


Figure 18 Characteristic reflectance features for common minerals. Representative spectra are from PK11DD001.

Specular hematite script

A new script for specular hematite was developed to detect the specific reflectance spectra for this type of iron oxide and to map its abundance. A representative reflectance spectra for specular hematite is shown in Figure 19, displaying the high reflectance values in the SWIR when compared to the VNIR and a steep slope between 900-1250 nm. A combination of VNIR and SWIR absorption features were used to create new algorithms in TSG for a specular hematite abundance script. VNIR reflectance ratio of the steeply dipping spectra between 900 and 1200 nm, and high reflectance values in the SWIR, represented by flat line between 1250 and 1600, were encoded into the script and combined to show their abundance throughout the drill hole (Figure 20b).

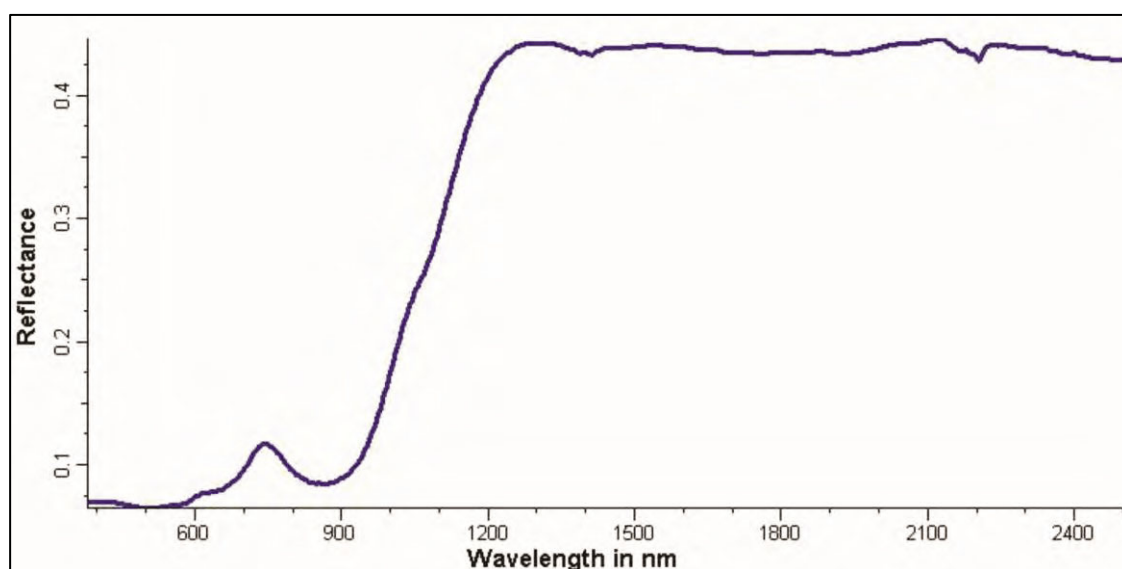


Figure 19 Characteristic reflectance spectra for specular hematite used to create script in the TSG program.

BIF

Two main intervals of BIF are intersected, from 25 to 82 m depth and from 185 to 190 m. This rock type can be classified into (1) least-altered BIF, (2) stage 1 hypogene magnetite-quartz, (3) stage 2 specularite and martite and (4) stage 3 supergene goethite-altered BIF (Figure 20). Ferric oxide abundance is highest in areas that contain BIF. The abundance of ferric oxide in BIF shows a steady increase from the top of the drill core, reaching its highest abundance at depths between 35 to 40 m. From there, the ferric oxide abundance steadily decreases (40 to 60 m), with changing goethite chemistry from vitreous to goethite towards mafic rocks (Figure 20a).

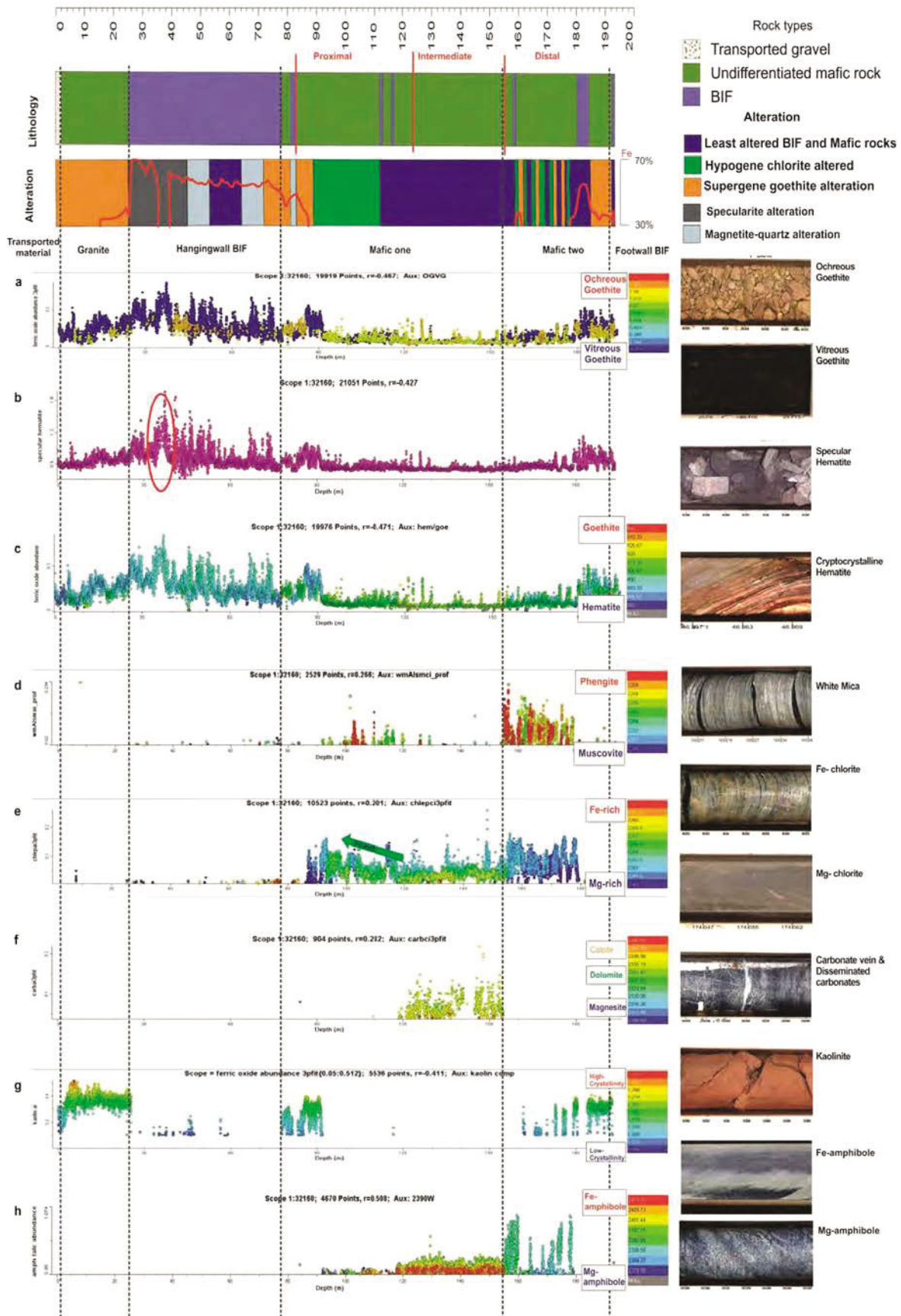


Figure 20 Summary image of hyperspectral data within PK11DD001 separated into main lithologies and alteration zones (observed in core logging) with characteristic images of rock types. image (a) ferric oxide abundance showing ochreous goethite (yellow) and vitreous goethite (blue), (b) specular hematite abundance, (c) ferric oxide abundance showing the distribution of goethite (yellow to red) and hematite (blue to green), (d) white mica abundance with composition ranging from muscovite to phengite, (e) chlorite abundance and composition ranging from Mg- to Fe-rich, (f) carbonate abundance and composition showing mostly calcites, (g) kaolin abundance and crystallinity, and (h) amphibole abundance with composition ranging from Mg- to Fe-rich. (A3 size image in Appendix 10).

Based on conventional logging, ochreous goethite is dominant in two horizons, at 40 to 45 m and 78 to 82 m. Vitreous goethite is located in areas with slightly higher ferric oxide values and in association with hematite-enriched BIF from 25 to 40 m and 45 to 75 m. The hematite-goethite script successfully identifies these before mentioned goethite intervals in core. Whereas, the ochreous goethite-vitreous goethite script separates the different goethite mineral species.

Kaolin group minerals in BIF occur at the base of the thickest BIF unit, between 78 to 82 m depth, with some scattered low abundances of kaolin group minerals also located between 40 to 45 m. Kaolin group minerals are more abundant in layers containing ochreous goethite, rather than with vitreous goethite in surrounding BIF (Figure 21). However, some areas show kaolin group minerals associated with vitreous goethite and hematite (~85 m).

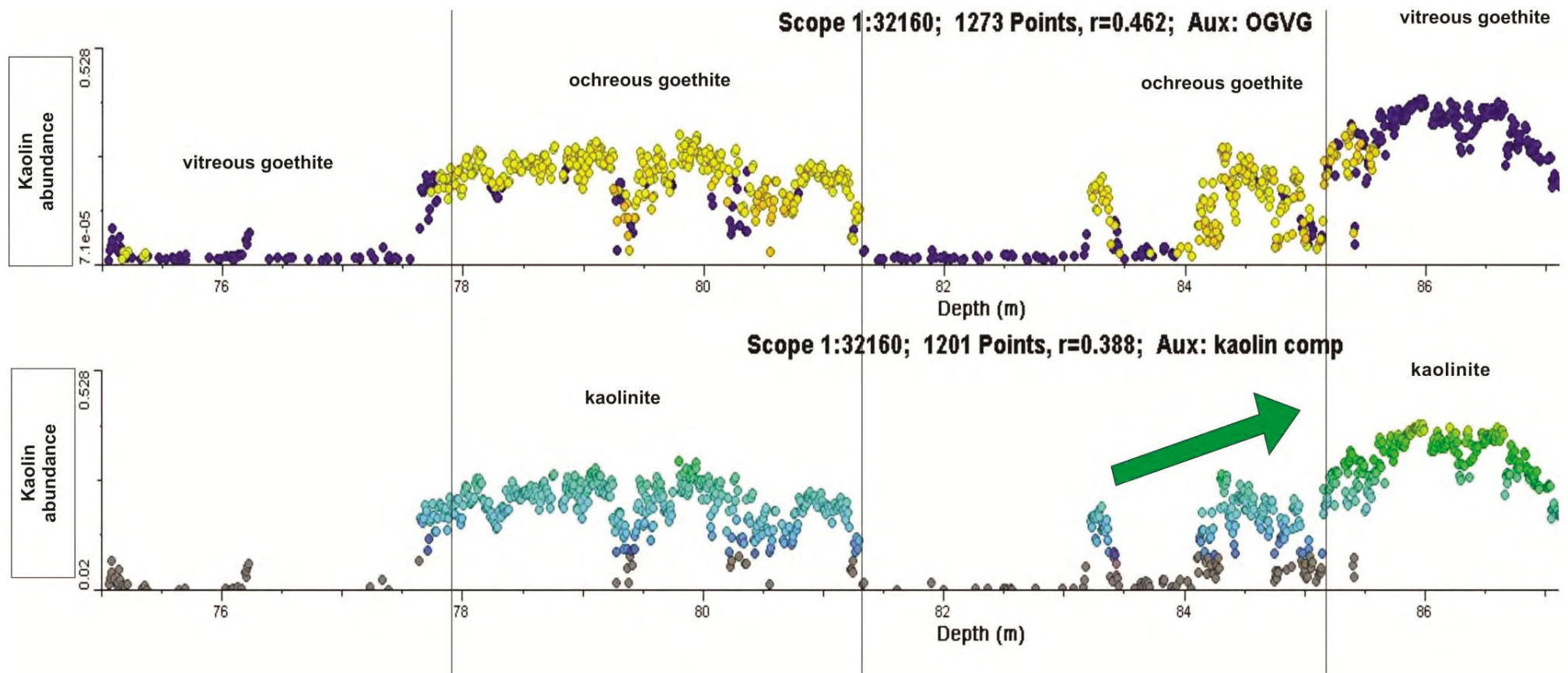


Figure 21 Kaolin group minerals association with goethite minerals in proximal mafic rocks between 75 to 87 m. Kaolin minerals show an association with ochreous goethite (yellow), and vitreous goethite (blue) in surrounding rocks (BIF). At ~86m kaolin shows an association with vitreous goethite. The increase in crystallinity is also observed (blue=low crystallinity) (green/yellow = higher crystallinity).

Specular hematite is concentrated in BIF at depths between 27 to 47 m, with the highest abundances at 40 to 45 m depth (Figure 20b). Narrow intervals of specular hematite-altered BIF are present at depths 180 to 183 m. The data in Figure 22 are separated into two groups showing a low ferric oxide abundance (0 -0.4) and a high ferric oxide abundance (0.4-0.5), with the values of the ferric oxide abundance mainly based on the depth of the Crystal Field Absorption Feature at around 900 nm. Specular hematite abundance directly corresponds with the ferric oxide abundance (Figure 22).

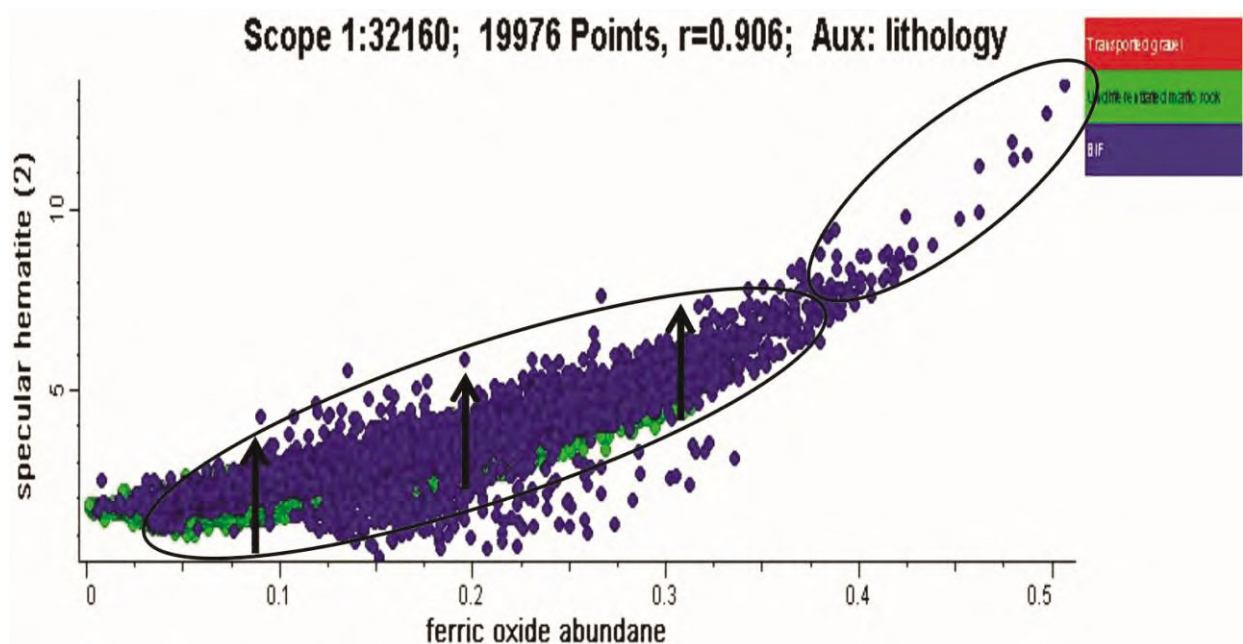


Figure 22 Relationship between specular hematite and ferric oxide abundance.

Mafic igneous rocks

Mafic rocks are divided into two compositional groups based on the collected hyperspectral data. The “proximal” mafic compositional group is located at 92 to 129 m depth (i.e. in a proximal position to BIF-hosted iron ore), whereas the “distal” group lies between 129 to 192 m depth. The proximal mafic rocks are characterised by an elevated abundance of chlorite and carbonate minerals (Figure 20e, f), whereas the distal rocks contain more amphibole and white mica. Quartz was observed during conventional logging of these mafic rock intervals, but was not detected by VNIR and SWIR data. The presence of quartz has been confirmed from the collected thermal infrared data.

Two kaolinitic zones in mafic rocks are observed, with the first being located at the lower lithological contact between the thick BIF interval and proximal mafic igneous rocks (i.e. at 80 m), which coincides with a 4 m-wide zone (78 to 92 m) of crystalline kaolin group mineral enrichment. A second zone of kaolin group minerals occurs in the distal mafic rocks between 155 to 195 m depth as a number of discrete 1 m-wide, intervals of crystalline kaolin group minerals.

Chlorite becomes more abundant in mafic igneous rocks with proximity to the lithological contact with BIF (i.e. from 155 to 90 m depths, corresponding with the proximal mafic rocks). Concomitant with the increase in the abundance of chlorite is slight increase in the Mg/Fe ratio for chlorite (observed from 115 to 97 m). Chlorite abundance in distal mafic rocks varies in unison with the occurrence of discrete 1 m-wide shear zones (located between 155 and 180 m depth). Three prominent, 1 m-wide, intervals of chlorite-rich mafic rocks are logged in the drill hole and are interpreted from spectral reflectance data. These chlorite intervals are mostly Mg-rich with a weak compositional change to Fe-rich chlorite towards amphibole-rich rocks, coinciding with an increase in the abundance of detected kaolin group minerals and ferric oxide minerals, such as goethite (Figure 24).

Amphibole mineral abundance corresponds with the occurrence of mafic igneous rocks between 120 to 180 m depths. Amphibole minerals are most abundant in the distal mafic rocks between 155 to 180 m depth, where detectable variations in the abundance of amphibole suggests the presence of at least six compositionally distinct layers over this depth range. The proximal mafic rocks contain higher Fe/Mg ratios for amphibole minerals compared with distal mafic rocks (Figure 20h).

White mica is abundant in the distal mafic rocks, with lower abundances scattered throughout proximal mafic rocks; white mica compositions are mostly Al-poor (e.g. phengite). White mica distribution shows that white mica abundance increases in the distal mafic rock towards the proximal mafic rock, but does not occur at the contact with BIF (Figure 20d).

Carbonate minerals occur exclusively between the intervals of 120 to 155 m, corresponding to the lower half of the proximal mafic rock interval, where abundant 3 to 5 cm-thick, carbonate-rich veins cut gabbro. The carbonate minerals range in composition from calcite to Mg-rich calcite (Figure 20f).

Transported material

Kaolin group minerals are located at the top of the drill hole between depths 0 to 25 m; the high kaolin group mineral abundance corresponds to saprolite zones within the regolith (Figure 20g). Transported materials logged between depths of 0 to 2 m contain kaolin group minerals with low crystallinity, whereas in situ saprolite logged from 2 to 25 m displays crystalline kaolin group minerals (Figure 23). Rocks between 2 to 25m are rich in quartz and feldspar minerals.

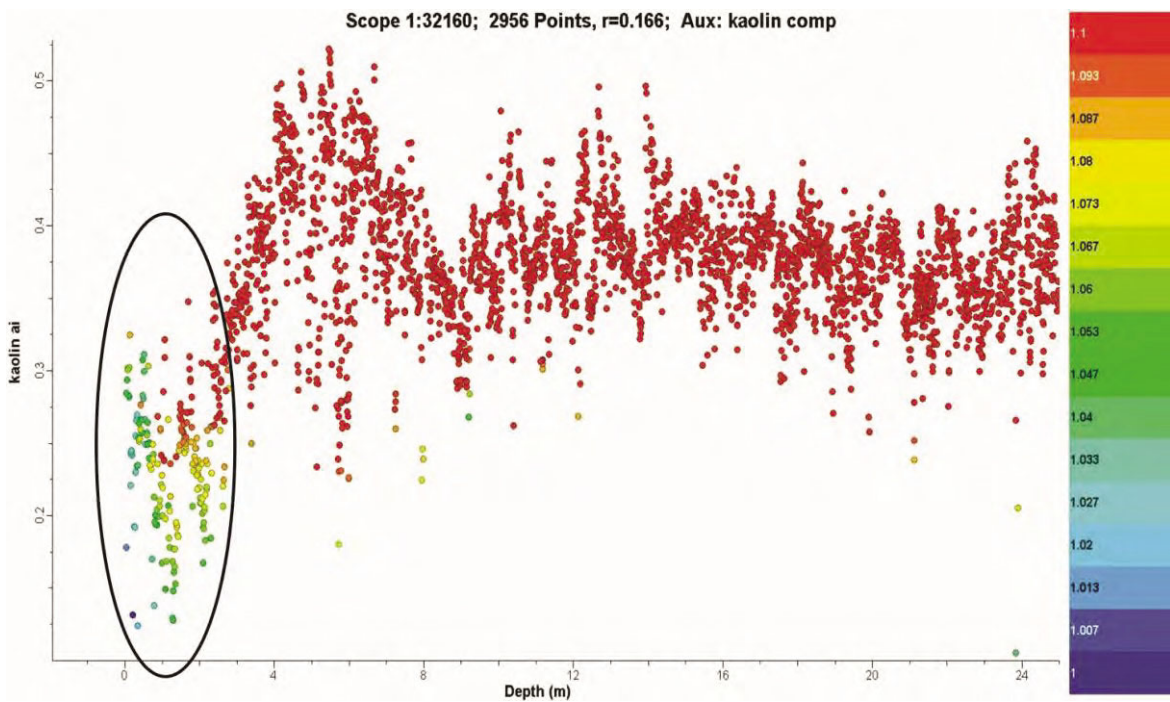


Figure 23 Kaolin mineral abundance and crystallinity in the drill hole interval 0 to 25 m depth. The red circles indicate crystalline kaolin, whereas the other colours indicate the presence of kaolin that is not crystalline. The kaolin abundance and kaolin crystallographic data show the distinction between transported sediment with low kaolin crystallinity and in situ mafic rock saprolite with crystalline kaolin.

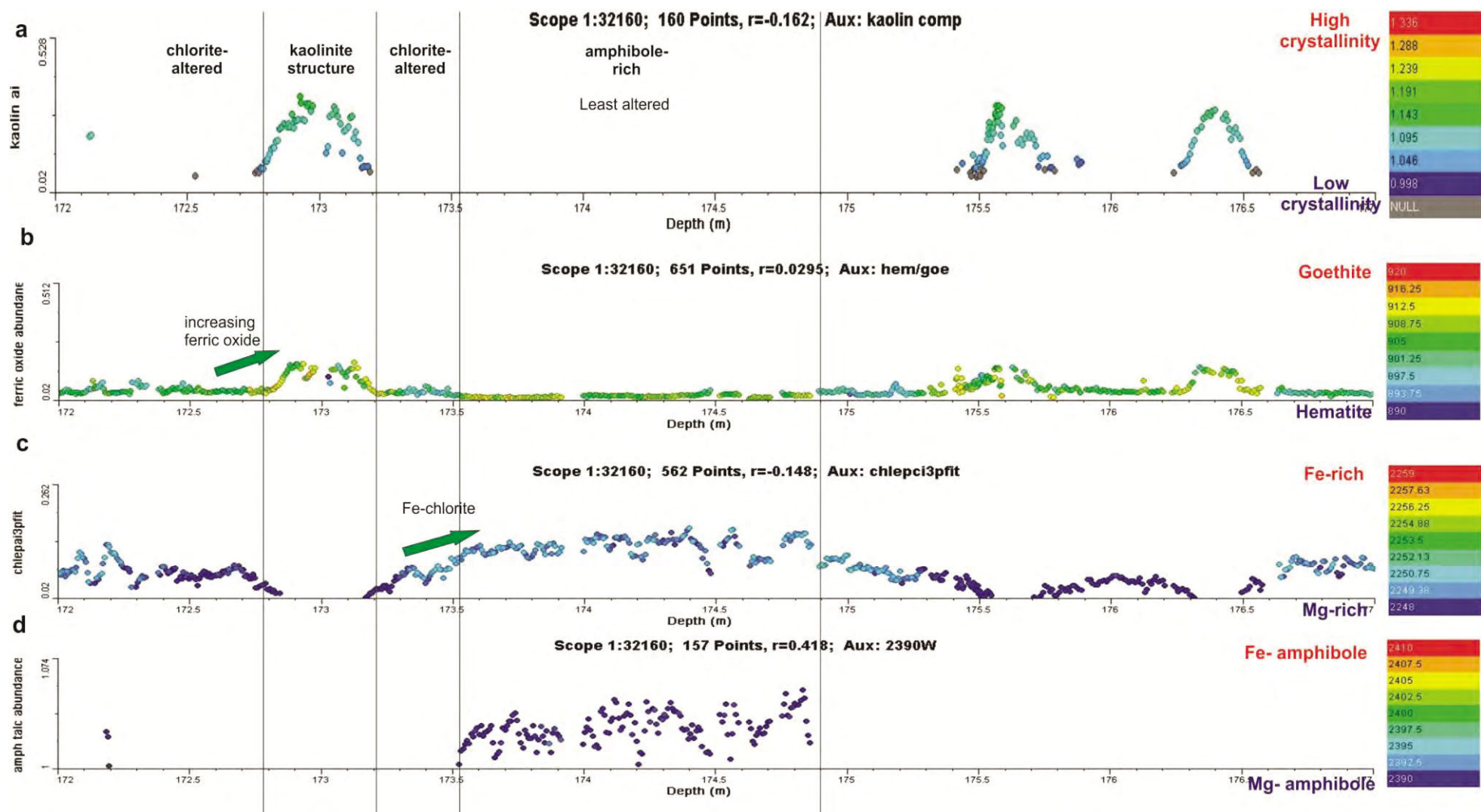


Figure 24 Several 1 m-wide shear zones documented in the down-hole interval of 172 to 177 m depth correspond with elevated abundances for kaolin and ferric oxide minerals, with outer halos of Fe-rich chlorite and amphibole, and distal halos of more Mg-rich chlorite and amphibole. (a) kaolin abundance and composition, (b) ferric oxide abundance in relation to hematite/goethite compositions, (c) chlorite abundance and compositions, (d) amphibole abundance and compositions.

DISCUSSION

Relating observed changes in hydrothermal alteration minerals to geochemical data at Mount Richardson

Petrological studies that combine conventional logging of drill core with microscopy indicate that fresh least-altered BIF has experienced two stages of hypogene alteration followed by supergene alteration. Whereas, nearby mafic igneous rocks (gabbro) are affected by at least one recognised stage of hypogene alteration and later supergene alteration. The intensity of hypogene and supergene alteration zones increase with proximity to deformed contacts between BIF and adjacent gabbro. The interpretation of geochemical data for hypogene and supergene alteration mineral assemblages is complicated by their superposition in many areas. This section interprets geochemical changes in BIF and gabbro associated with hypogene and supergene alteration.

BIF

The transition from fresh least-altered BIF to hypogene-altered BIF (i.e. stage 1 magnetite-quartz and stage 2 specularite-martite) is marked by an increase in magnetite or specularite and a decrease in primary quartz through the replacement of primary quartz bands by the hypogene iron oxide minerals. These mineralogical changes are associated with a 104% increase in $\text{Fe}_2\text{O}_{3\text{Total}}$ and a 30% decrease in SiO_2 . Other significant elemental changes include an increase in MnO_2 , Al_2O_3 and Na_2O . Considering that fresh least-altered BIF mainly comprises $\text{Fe}_2\text{O}_{3\text{Total}}$ and SiO_2 with low concentrations ($< 0.2\%$) of other elements, any minor changes in trace elements will have a large impact on mass balance calculations.

The large percentage increase in Al_2O_3 in the hypogene-altered BIF may represent either the mobility of Al in the hydrothermal fluid, or a primary compositional difference in the analysed samples of BIF. Given that Al is a relatively immobile element in most hypogene fluids associated with greenstone belt-hosted mesothermal gold deposits (Kerrick 1989), it is more likely that the BIF at Mount Richardson contains minor shale or mudstone layers that would cause variability in Al_2O_3 concentrations in BIF. The increase in MnO_2 may be a product of the weak supergene overprint of BIF owing to the mobility of Mn in oxidised supergene fluids. The decrease in the measured FeO values and corresponding increase in measured Fe_2O_3 confirms that the least-altered BIF experienced oxidation by hypogene and

possibly supergene fluids, resulting in specularite and martite (hypogene) and goethite (supergene). The increases in Na₂O, CaO, K₂O, Ni, and Co in BIF are probably the product of chemical exchange between gabbro and BIF during hypogene alteration. Whereby these elements were transferred from gabbro to BIF, resulting in their enrichment in BIF and matching depletion in proximal hypogene alteration zones in gabbro (Figures 12 and 16). The sodic, calcic and potassic enrichments detected in BIF were not supported by observed enrichment in feldspars or carbonate minerals (based on interpretation of TIR data). Similar enrichment and depletion patterns are noted for BIF-hosted iron ore deposits at the Weld Range (Duuring et al. 2012) and the Koolyanobbing and Windarling iron ore camps (Angerer et al. 2012). Other trace element enrichments in BIF and gabbro, including Ag and As, have a less constrained origin and may have been added to both rock types directly from hypogene fluids since these elements are not commonly present in significant primary concentrations in these rocks and they are mutually enriched in hypogene alteration zones in both rock types.

Supergene-altered BIF displays a volumetric increase in goethite minerals (vitreous and ochreous) and a dramatic decrease in primary quartz relative to least- and hypogene-altered BIF. Relative to these rocks, supergene-altered BIF displays a strong enrichment in Fe₂O₃ Total and a major decrease in SiO₂. Enrichments in measured Fe₂O₃ values (relative to FeO) and an increase in LOI values, mirrors the enrichment in goethite in supergene-altered BIF. The two-fold increase in MnO₂ abundance in supergene- relative to hypogene-altered BIF reflects the enhanced mobility and abundance of Mn in oxidised supergene fluids. The strong enrichments in K₂O, Na₂O, Co, Ni, and Cr in supergene-altered BIF are probably the result of further chemical exchange between the gabbro and BIF. These levels of enrichment are mostly higher than in hypogene alteration zones in BIF, suggesting that supergene fluids promoted the transferral of these elements from gabbro to BIF. Increases in mobile elements such as As, Ag, Bi, Cu, Mo, Pb and W are most likely transported by supergene fluids and have an uncertain origin. Although apatite was not observed in thin-section, P₂O₅ is enriched in supergene-altered zones relative to least-altered BIF. Lastly, REE are enriched in supergene-altered BIF, with LREE more enriched than HREE. These REE trends are consistent with other documented cases of REE mobility in hydrothermal fluids (Renner et al. 1994).

GABBRO

Relative to least-altered gabbro, weakly supergene-modified and hypogene-altered gabbro in intermediate zones display increases in MgO, with depletions in K₂O, Na₂O, and CaO. These compositional changes most likely equate to the replacement of igneous plagioclase by hypogene Mg-rich chlorite (detected by hyperspectral data). The source of Mg enrichment in hypogene-altered gabbro is unclear but may be the result of the mobilisation of Mg from distal areas of the gabbro, or primary compositional variations in the mafic rocks.

Proximal alteration zones record the combined effects of hypogene and supergene alteration. These zones are enriched in SiO₂, Al₂O₃, with major depletions in FeO, CaO, Na₂O, MgO, MnO, TiO₂, K₂O, and P₂O₅. The combination of hypogene and supergene fluids have most likely been responsible for the movement of Fe and Si from BIF and enrichment in proximal mafic rocks. At the same time, the Large Ion Lithophile Elements (LILE), including Ca, Na, K, were mobile and depleted from proximal alteration zones and enriched in BIF. The mobile behaviour of LILE has been documented elsewhere for altered mafic rock (Leshner et al. 2001, Arndt et al. 1997) Depletion in MgO in proximal alteration zones in mafic rocks at Mount Richardson (i.e. within 10 m of BIF contacts) probably corresponds to the replacement of hypogene chlorite and primary/metamorphic amphibole by goethite minerals.

Mapping rock types and alteration zones at Mount Richardson using hyperspectral data

BIF

Hyperspectral data confirm that the highest grade iron ore zones are hosted by BIF and correspond with intervals with the highest concentrations of hypogene specularite. The existing ferric oxide script was the most accurate for discriminating BIF from mafic igneous rocks. The specular hematite script developed by this study is better than the ferric oxide abundance script at identifying specularite-rich iron ore zones. The goethite-hematite script was useful for distinguishing these minerals, but did not separate ochreous from vitreous goethite. Rather, the existing ochreous goethite-vitreous goethite script was useful for this purpose. High LOI values in proximal mafic rocks at 129 m corresponds with high abundances of goethite relative to hematite recorded by hyperspectral data. Further evaluation of the TIR spectral data is required to map variations in quartz, feldspar or carbonate abundance; these minerals were not accurately defined using conventional core logging techniques.

GABBRO

Compositions of mafic rocks can be best defined by the presence of primary and metamorphic amphibole and hypogene chlorite. Based on observed variations in hyperspectral data for amphibole abundance and mineral chemistry in fresh and least-altered gabbro (i.e. between the depths of 110 and 155), it seems likely that there are discrete primary compositional layers present within this interval of gabbro. Sharp lithological contacts were not observed during visual logging within this interval; however, gradational changes in grain size of amphiboles and plagioclase were logged during the conventional logging of the drill core. These compositional layers may correspond to the presences of several narrow sills in the gabbro, or compositional variations due to local fractionation of the melt during crystallisation of the mafic magma. Further investigation is needed to distinguish metamorphic from primary amphibole minerals and their mapped mineral abundances with hyperspectral data. If no correlation is seen it could be concluded that more than one mafic rock type is present with a difference in primary mineral compositions. Hypogene alteration zones in mafic igneous rocks are defined by diagnostic absorption features that measure the Mg/Fe ratio of chlorite and amphibole. Notable increases in Mg/Fe ratios for hypogene chlorite with proximity to BIF-hosted iron ore zones, or discrete shear zones in distal mafic rocks can be observed.

Supergene alteration of mafic rocks within 10 m of the contacts with BIF results in the replacement of primary, metamorphic, and hypogene minerals by supergene goethite, hematite and kaolinite. However, it is important to note that the observed changes in the Mg/Fe signatures for chlorite and amphibole are unaffected by supergene alteration and are indicators of chemical changes in these minerals due to earlier hypogene alteration.

Importantly, there is evidence that some supergene minerals inherit anomalous mineral chemistry signatures from earlier hypogene alteration or primary/metamorphic minerals in intensely supergene-altered zones located in discrete distal shear zones in the distal mafic rocks (Figure 24). For example, at about 175 m depth in distal mafic rocks, Fe-rich kaolinite is indicated by a prominent 2235 feature (cf. Cudahy 1997) (Figure 25). The Fe-rich kaolinite was most likely a product of the supergene replacement of Fe-rich primary/metamorphic amphibole.

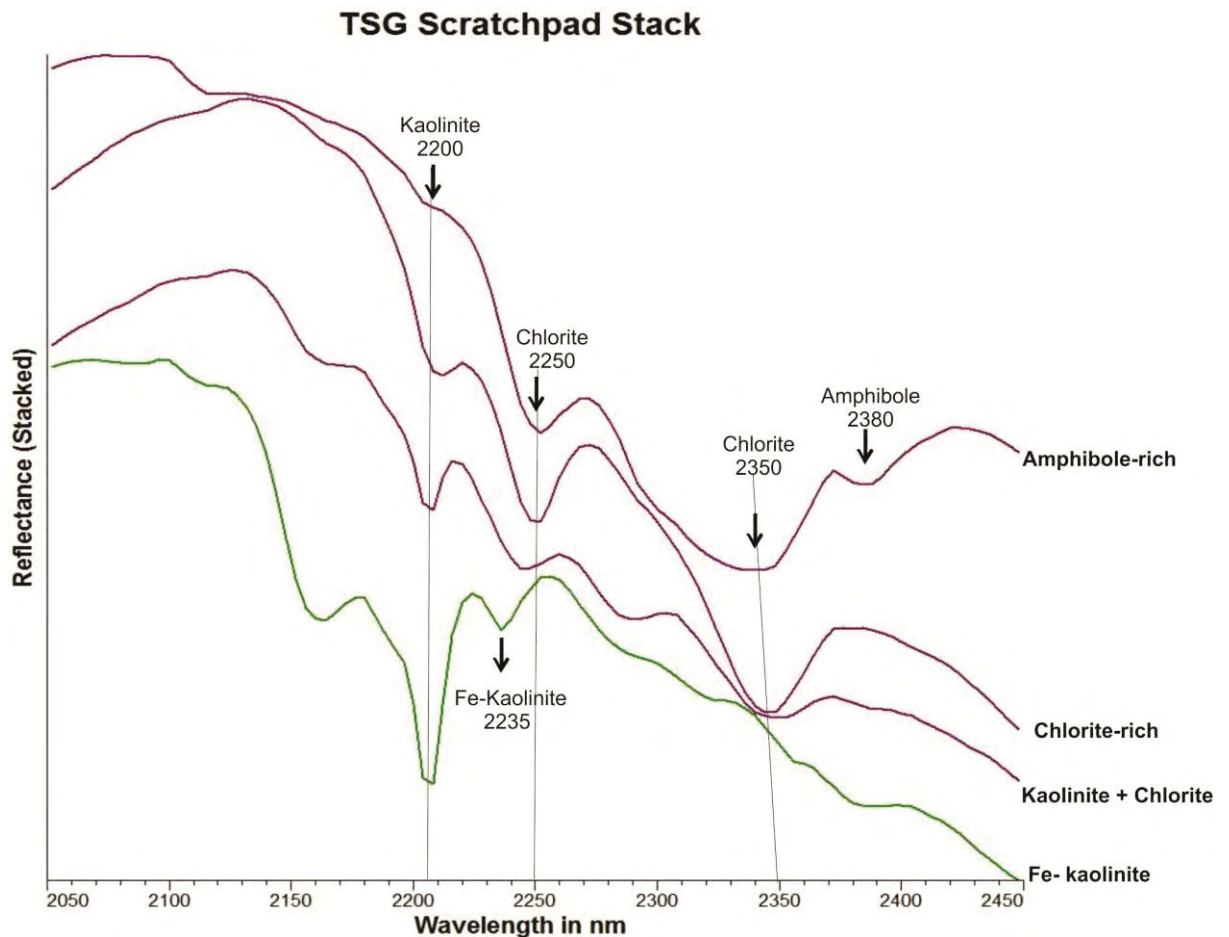


Figure 25 Representative reflectance spectra for mafic rocks between 170 - 180 m, showing the transition from least-altered distal mafic rock (top reflectance spectrum), through intensely chlorite-altered to supergene-altered rock samples in the centre of the shear zones (bottom reflectance spectrum). Kaolin group minerals inherit Fe-rich composition possibly from chlorite formed during hypogene processes.

Evaluating the usefulness of hyperspectral studies to iron ore exploration

The application of hyperspectral studies to the study and exploration for iron ore has advanced during the last five years. Two recent studies, by Gallagher (2013) and Haest (2012 a, b) have tested the multi-scale application of hyperspectral drill core data for studies of iron ore deposits, ranging from analyses of hand-specimen (ASD and HyLogging system) to district-wide scales (ASTER and HyMap).

Gallagher (2013) examined the high grade magnetite-goethite (M-G) and magnetite-microplaty hematite (M-mpIH) iron ore deposit at Hashimoto to establish an understanding of the mineralogical and geochemical characteristics and ore forming processes in a polygenetic iron ore system. Methods applied included an integration of conventional core-logging, rock petrography, HyLoggingTM data and high resolution whole-rock geochemistry

(including major, trace and REE) on two diamond drill holes. Gallagher identified nine mineralogical ore types using the HyLogging™ system, based on the relative abundances of goethite, microplaty hematite and martite. The HyLogging™ system was not able to differentiate textural variations amongst hematite ore; however it was successfully used to identify the contact between transported material and in situ bedrock, which has strong impacts on strip ratios, final pit designs and effective long term mine planning. Haest (2012a, b) used hyperspectral- derived mineralogy to build one, two and three dimensional models for the architecture of a channel iron ore system, with applications towards exploration and mining specifically at Rocklea Channel Iron Deposit. A comparison of laboratory geochemistry and field geologist logging was applied to 180 drill holes with major findings demonstrating a relationship between parent rock composition, superimposed regolith cover, and channel iron deposit ore quality, which are linked through groundwater interactions and physicochemistries of parent rock and the deposit. Implications of this study show these deposits can form several kilometres downstream from source rock, potential vectors include vitreous goethite, calcrete, Al and Fe smectite cover, with improved mineralogy from hyperspectral data improving resource delineation, processing and pit design.

The main implications of this present study are that it is possible to use hyperspectral technologies in combination with traditional petrographical and geochemical studies for the discrimination of hypogene and supergene alteration zones in BIF and surrounding mafic igneous rocks. In addition, this study shows an improvement in the identification of hypogene iron ore zones through the development of a specular hematite script, which is more accurate than the existing ferric oxide abundance script.

Mineralogy derived from the Hylogging™ system has provided a range of information that could not have been determined through use of visual logging techniques. The uppermost mafic rock unit (2-25 m) has probably been misclassified during visual logging; hyperspectral reflectance spectra for these rocks show abundant feldspar and quartz minerals, which suggest it is granitic rock rather than supergene-altered mafic rocks. The changes in Mg/Fe ratios were significant in the determination of hypogene alteration evident in the mafic rocks proximal to mineralised BIF. These changes in Mg/Fe compositions of chlorites and amphiboles could not have been determined in visual logging. The successful mapping of the newly developed spectral hematite script showed improvement from visual logging. In the hanging wall BIF specular hematite was visually observed with abundances being improved with application of the script, in footwall BIF specularite was not logged; however, the script shows specularite is

present. With an early application of these hyperspectral methods (i.e. the HyLogging™ system) in the large volume sampling logging of drill core, we can potentially develop new routine applications in mining exploration.

Development of land surface mineral mapping techniques, field airborne (e.g., Hymap; Laukamp 2011b) and satellite hyperspectral sensors (e.g., Hyperion; Cudahy and Barry 2002) would be significant in the exploration of high-grade iron ore deposits. Potentially mapping vitreous goethite, ochreous goethite and specular hematite could be used as pathfinder minerals for high grade iron ore, whereas kaolin group minerals impact on ore quality. However, additional research is required to test the transferral of the specular hematite script to remote sensing surveys. Down-sampling of the specular hematite spectral data would be needed to test the application of this script to the resolution of airborne spectra. Changes in the Mg and Fe ratio in chlorite and amphibole composition in mafic igneous rocks has been demonstrated at Mount Richardson as indicators of hypogene alteration. These signatures probably translate well to airborne and satellite surveys, as demonstrated by the interpretation of ASTER data, showing changes in Fe-rich chlorite associated with hypogene magnetite-rich ore at the Beebyn deposits, Weld Range (Duuring et al. 2012).

CONCLUSIONS

The integration of HyLogging data with conventional logging of drill core, petrological data, and geochemical data has constrained the relationships between rock types and alteration at the BIF-hosted iron ore prospect at Mount Richardson, Yilgarn Craton, Western Australia. Three stages of alteration in BIF are identified: hypogene magnetite-quartz alteration (stage one), hypogene specularite-martite (stage two) and supergene goethite enrichment (stage three). Surrounding mafic igneous rocks are divided into proximal, intermediate and distal hypogene alteration zones relative to proximity to BIF-hosted iron ore zones. With increasing proximity to BIF contacts, primary and metamorphic minerals in mafic rocks become progressively replaced by hypogene chlorite. Whereas, the inner proximal alteration zones located within 10 m of BIF contacts are intensely replaced by supergene goethite, hematite and kaolinite.

The transition from fresh least-altered BIF to hypogene-altered BIF is marked by an increase in magnetite or specularite and a decrease in primary quartz through the replacement of primary quartz bands by the hypogene iron oxide minerals. These mineralogical changes are

associated with an increase in $\text{Fe}_2\text{O}_{3\text{Total}}$, MnO_2 , Al_2O_3 , Na_2O , CaO , K_2O , Ni and Co , and a decrease in SiO_2 . The increases in Na_2O , CaO , K_2O , Ni , and Co in BIF are probably the product of chemical exchange between gabbro and BIF during hypogene alteration. Relative to least-altered gabbro, weakly supergene-modified and hypogene-altered gabbro in intermediate zones display increases in MgO , with depletions in K_2O , Na_2O , and CaO . These compositional changes most likely equate to the replacement of igneous plagioclase by hypogene Mg-rich chlorite. Proximal alteration zones record the combined effects of hypogene and supergene alteration. These zones are enriched in SiO_2 , Al_2O_3 , with major depletions in FeO , CaO , Na_2O , MgO , MnO , TiO_2 , K_2O , and P_2O_5 . The combination of hypogene and supergene fluids have most likely been responsible for the movement of Fe and Si from BIF and enrichment in proximal mafic rocks.

Existing computer-based scripts, including ferric oxide abundance, hematite-goethite and ochreous goethite-vitreous goethite are useful for identifying BIF, and for characterising the different alteration and iron ore styles in BIF. Furthermore, a specular hematite script developed by this study has a higher accuracy than existing scripts for the identification of hypogene specularite ore zones in BIF. The crystallinity index of kaolinite was useful for discriminating transported from in situ regolith. Mafic igneous rocks demonstrate zonation in primary and metamorphic minerals; from amphibole in distal areas to BIF contacts, to hypogene chlorite in proximal zones. Within 10 m of BIF contacts, these minerals are entirely replaced by supergene hematite, goethite and kaolinite. Furthermore, hyperspectral data indicate that hypogene chlorite becomes increasingly Mg-rich with proximity to shear zones and BIF-hosted specularite ore zones.

Mineral mapping using hyperspectral data is a valuable tool that can be justified with conventional logging and analytical techniques. The results of this study, such as the new specular hematite script, can potentially be applied to interrogating remote sensing data. However, further work is required to first test the effects of down-sampling the hyperspectral data to match the spectral resolution of the remote sensing data sets (e.g. ASTER, HyMap).

REFERENCES

- ADAMS J. B. & FLILIC A. L. 1967 Spectral reflectance 0.4 to 0.2 microns of silicate rock powders, *Journal of geophysical research*, vol. 72, pp. 5705-5715.
- ANGERER T., DUURING, P., HAGEMANN, S.G., THRONE, W., MCCUAIG, T. submitted A mineral system approach to iron ore in Archaean and Paleoproterozoic BIF of Western Australia.
- ANGERER T., HAGEMANN S. G. & DANYUSHEVSKY L. V. 2012 Geochemical evolution of the Banded Iron Formation-hosted high-grade iron ore system in the Koolyanobbing greenstone belt, Western Australia, *Economic Geology*, vol. 107, pp. 599-644.
- ARNDT N. T., NALDRETT A. J. & HUNTER D. R. 1997 Ore deposits associated with mafic magmas in the Kaapvaal Craton, *Mineralium Deposita*, vol. 32, no. 4, pp. 323-334.
- BARLEY M. E., *et al.* 1999 Hydrothermal origin for the 2 billion year old Mount Tom Price giant iron ore deposit, Hamersley Province, Western Australia, *Mineralium Deposita*, vol. 34, no. 8, pp. 784-789.
- BAU M. & ALEXANDER B. W. 2009 Distribution of high field strength elements (Y, Zr, REE, Hf, Ta, Th, U) in adjacent magnetite and chert bands and in reference standards FeR-3 and FeR-4 from the Temagami iron-formation, Canada, and the redox level of the Neoproterozoic ocean, *Precambrian Research*, vol. 174, pp. 337-346.
- CASSIDY K. C., *et al.* 2006 A revised geological framework for the Yilgarn Craton, Western Australia. pp. 8. Perth: Geological Survey of Western Australia.
- CHEN S. F. 2004 Geology of Marmion and Richardson 1:000000 sheets, *1:100000 Geological Series Explanatory Notes*, vol. Western Australia Geological Survey, p. 27.
- CLARK A. M. 1993 Hey's Mineral Index, Mineral Species, Varieties and Synonyms. (3rd edition). Chapman and Hall, London.
- CLARK R. N., & ROUSH, T.L 1984 Reflectance Spectroscopy: Quantitative Analysis Techniques for Remote Sensing Applications, *J. Geophys. Res.*, vol. 89, pp. 6329-6340.
- COOPER R. W. F. D. J. 2009 Iron ore deposits of the Yilgarn Craton - 2009 (1:1500000), *Geological Survey of Western Australia*.
- CUDAHY T. & BARRY P. S. 2002 Earth magmatic-seawater hydrothermal alteration revealed through satellite-borne Hyperion imagery at Panorama, Western Australia. IEEE 2002 International Conference on Geoscience and Remote Sensing. pp. 590-592. Toronto.
- CUDAHY T. J. 1997 PIMA-II spectral characteristics of natural kaolins, *Exploration and mining report CSIRO/AMIRA*.
- CUDAHY T. J., *et al.* 2008 Next Generation Mineral Mapping: Queensland Airborne HyMap and Satellite ASTER Surveys 2006-2008. CSIRO report P2007/364. pp. 153.
- DANIELSON A., MOLLER P. & DULSKI P. 1992 The europium anomalies in banded iron formations and the thermal history of the oceanic crust, *Chemical Geology*, vol. 97, pp. 89-100.
- DUURING P. AND HAGEMANN, S. 2013 Controls for iron mineralisation hosted by Banded Iron Formation in the Mount Richardson district, Yilgarn Craton, Western Australia, Unpublished University of Western Australia report to Cliffs Natural Resources, 28p.
- DUURING P., HAGEMANN S., NOVIKOVA Y., CUDAHY T. AND LAUKAMP C. 2012 Targeting iron ore in Banded Iron Formation using ASTER data: Weld Range greenstone belt, Yilgarn Craton, Western Australia, *Economic Geology*, vol. 107, no. 4, pp. 585-597.
- DYMEK R. F. & KLEIN C. 1988 Chemistry, petrology and origin by banded iron-formation lithologies from the 3800 Ma Isua supracrustal belt, West Greenland, *Precambrian Research*, vol. 39, pp. 247-302.
- GALLAGHER R. 2013 Hashimoto high-grade martite-goethite (M-G), martite-microplaty hematite (M-(mplH)) iron ore deposit- towards understanding ore genesis and associated alteration zoning, *Research project report*.
- GOLE M. J. 1981 Archean Banded Iron-Formations, Yilgarn Block, Western Australia, *Economic Geology*, vol. 76, pp. 1954-1974.

- GRANT S. L. 1997 Geochemical, radiogenic tracer isotopic, and U-Pb geochronological studies of Yukon Tanana Terrane rocks from the Money Klippe, southeastern Yukon, Canada. Edmonton: University of Alberta.
- GRESENS R. L. 1967 Composition-volume relationships of metasomatism, *Chemical Geology*, vol. 2, pp. 47-65.
- GRIFFINS C., HERRMANN W. & LARGE R. R. 2005 Altered volcanic rocks: a guide to description and interpretation: Hobart, Tasmania, Australia, *Centre for Ore Deposit Research*, p. 275.
- HAEST M., CUDAHY, T., LAUKAMP, C. and GREGORY, S. 2012a Quantitative mineralogy from infrared spectroscopic data: (I) Validation of mineral abundance and composition scripts at the Rocklea channel iron deposit in Western Australia, *Economic Geology*, pp. 209-228.
- HAEST M., CUDAHY, T., LAUKAMP, C. and GREGORY, S. 2012b Quantitative mineralogy from infrared spectroscopic data: (II) Three-dimensional mineralogical characterization of the Rocklea channel iron deposit, Western Australia, *Economic Geology*, vol. 107, no. 2, pp. 229-249.
- HUNT G. R. 1977 Spectral Signatures Of Particulate Minerals In The Visible And Near Infrared, *Geophysics*, vol. 42, pp. 502-513.
- JENSEN L. S. 1976 A new cation plot for classifying subalkalic volcanic rocks, *Ontario Geological Survey Miscellaneous Paper*, vol. 66, p. 22.
- KERRICH R. 1989 Lithophile element systematics of gold vein deposits in Archean greenstone belts; implications for source processes. In KEAYS R. R., RAMSAY W. R. H. & GROVES D. I. eds. The geology of gold deposits; the perspective in 1988. pp. 508-519. Chur, Switzerland: Harwood Academic Publishers.
- LASCELLES D. 2007 A possible origin of pisolitic iron ore deposits from raindrops and sheetwash in a semi-arid environment, *Iron Ore Conference 2007, Australasian Institute of Mining and Metallurgy*, Publication Series 6/2007, pp. 113-121.
- LASCELLES D. F. 2006 The Mount Gibson banded iron formation-hosted magnetite deposit: Two distinct processes for the origin of high-grade iron ore, *Economic Geology*, vol. 101, no. 3, pp. 651-666.
- LAUKAMP C. 2011a Short wave infrared functional groups of rock-forming minerals, *CSIRO Report EP115222*.
- LAUKAMP C. C., T.J., CLEVERLY, J. S., OLIVER N.H.S., AND HEWSON, R., 2011b Airborne hyperspectral imaging of hydrothermal alteration zones in granitoids of the Eastern fold belt, Mount Isa inlier, Australia, *Geochemistry: Exploration, Environmental Analysis*, vol. 11, no. 3-24.
- LESHER C. M., *et al.* 2001 Trace-element geochemistry and petrogenesis of barren and ore-associated komatiites. In BARNES S.-J., CROCKET J. H. & MARTIN R. F. eds. International Geological Correlation Program 427 field conference; Ore-forming processes in dynamic magmatic systems. pp. 673-696. Rouyn-Noranda, PQ, Canada.
- MCDONOUGH W. F. & SUN S. S. 1995 The composition of the Earth, *Chemical Geology*, vol. 120, pp. 223-253.
- MORRIS R. C., AND RAMANAIDOU, E.R., 2007 Genesis of channel iron deposits (CID) of the Pilbara Region, Western Australia, *Australian Journal of Earth Sciences*, vol. 54, pp. 733-756.
- MORRIS R. V., *et al.* 1985 spectral and other physiochemical properties of submicron powders of hematite (Fe₂O₃), maghemite (Fe₂O₃), magnetite(Fe₃O₄), goethite (FeOOH), *Journal of Geophysical Research*, vol. 90, pp. 3126-3144.
- RAMANAIDOU C. 1997 Measurement of the hematite:goethite ratio using field visible and near-infrared reflectance spectrometry in channel iron deposits, Western Australia, *Australian Journal of Earth Sciences*, vol. 44, pp. 411-420.
- RENNER R., *et al.* 1994 Komatiite flows from the Reliance Formation, Belingwe Belt, Zimbabwe; I, Petrography and mineralogy, *Journal of Petrology*, vol. 35, no. 2, pp. 361-400.
- SHERMAN D. M. & BURNS R. G. 1982 spectral characteristics of the iron oxides with application to the Martian Bright region mineralogy, *Journal of geophysical research*, vol. 87, pp. 169-180.
- SINGER R. B. & ROUSH T. L. 1985 Effects of temperature on remotely sensed mineral absorption features, *Journal of geophysical research*, vol. 90, pp. 434-444.

- SONNTAG I., LAUKAMP C. & HAGEMANN S. 2012 Low potassium hydrothermal alteration in low sulfidation epithermal systems detected by IRS and XRD: an example from the Co-O Mine, Eastern Mindanao, Philippines, *Ore Geology Reviews*, vol. 45, pp. 47-60.
- TAYLOR D., *et al.* 2001 Genesis of high-grade hematite orebodies of the Hamersley Province, Western Australia, *Economic Geology*, vol. 96, pp. 837-873.
- WINCHESTER J. A. & FLOYD P. A. 1977 Geochemical discrimination of different magma series and their differentiation products using immobile elements, *Chemical Geology*, vol. 20, no. 4, pp. 325-343.
- WYBORN L. A. I., HEINRICH C. A. & JAKES A. L. 1994 Australian Proterozoic Mineral Systems - Essential Ingredients and Mappable Criteria, *1994 AusIMM Annual Conference: Australian Mining Looks North - the Challenges and Choices*, vol. 94, no. 5, pp. 109-115.

APPENDIX 1: RESEARCH PROPOSAL

Research Proposal

Alteration Mineral Zonation Associated with High-Grade BIF-Hosted Iron Ore: Mineral Mapping Using Hyperspectral Drill Core Data

Laura Chiarelli

Supervisors

Paul Duuring

Steffen Hagemann

Carsten Laukamp

Word count: 5,512



**THE UNIVERSITY OF
WESTERN AUSTRALIA**

Abstract

The central aim of this research project is to assist exploration for BIF-hosted high grade iron ore in the Yilgarn Craton of Western Australia by better constraining genetic models for iron formation and by defining important pathfinder minerals and elements for detecting high-grade iron ore bodies. The Mount Richardson BIF-hosted iron ore prospect, located in the Southern Cross Domain of the Yilgarn Craton, is chosen for detailed study. This study will apply recent advances in hyperspectral logging (e.g. the 'HyLogger') in conjunction with conventional drill core logging to map alteration styles and zonation associated with high-grade iron ore. The Scanning Electron Microscope (SEM) will be used to validate the minerals detected using the HyLogger, whereas whole rock geochemical analyses of drill core samples will be used to define geochemical changes in the BIF and mafic country rock with distance from iron ore. The results from this study will help to constrain the composition of the hydrothermal fluids that reacted with BIF and mafic rocks, and will be used to compare with other BIF-hosted iron ore deposits in the Yilgarn Craton.

Contents

Abstract	56
1. Introduction	58
2. Background information	58
2.1 Introduction	58,59
2.2 Available spectral techniques for the detection of mineral abundance and mineral chemistry in rocks	59
2.2.1 Remote sensors: ASTER and HyMap	59-61
2.2.2 Proximal sensors: HyLogger and ASD	61-62
2.3 BIF-hosted iron ore deposits: their properties and models for their genesis	62
2.3.1 Physical and chemical properties of BIFs	62
2.3.2 Geographical distribution of BIF	62,63
2.3.3 Ore genesis models	63,64
2.3.4 Structural controls of Fe mineralization	64,65
2.3.5 Ore forming fluids and metal precipitation	65,66
2.4 BIF-hosted iron ore deposits: ore forming fluids	68
2.4.1 Metamorphic, hypogene alteration and supergene alteration	68,69
2.5 BIF-hosted iron ore deposits: their properties and models for the genesis	69,70
2.5.1 Koolyanobbing (Southern Cross Domain)	70
2.5.2 Beebyn and Madoonga (Murchison Domain)	71
2.5.3 Yilgarn BIF-hosted high-grade iron ore: ore forming processes	71
2.5.4 Discussion: Ore forming processes in Yilgarn Craton BIF-hosted high grade iron ore	72,73
2.5.5	
2.6 Examples of spectral studies applied to the exploration for BIF-hosted iron deposits	75
2.6.1 Weld Range greenstone belt, Western Australia: the use of ASTER data	75
2.6.2 Delineation of Channel Iron Deposits at Rocklea Dome: using HyLogger data	77
2.6.3 Discussion: Integration of spectral technologies in ore deposit exploration	78
3. Aims and objectives	78
4. Significance and outcomes	79
5. Methodology	79,80
6. Timeline	81
7. Budget	82
8. Appendix	83
9. References	84-88

1. Introduction

Demand for high-grade iron ore is rising at levels that will soon see significant depletion of high-grade iron ore deposits. As the search for new deposits becomes increasingly more difficult our exploration methods must evolve. Historical methods for iron ore exploration include direct observation of outcrop and drill core, as well as the interpretation of remotely acquired data, including geophysical and radiometric datasets. Recently, spectral data have been used to determine hydrothermal alteration patterns associated with ore deposits (e.g. porphyry Cu-Au, skarn alteration mineralogy at Yerington Nevada (Cudahy et al. 2001)). However, no systematic study exists that uses the HyLogger spectral analysis technique for the examination of hydrothermal alteration zonation associated with BIF-hosted hypogene iron ore deposits. This present study will be the first to test for the zonation of pathfinder minerals and mineral chemistry surrounding BIF-hosted iron ore deposits in the Yilgarn Craton. This research proposal outlines the key background information about the current understanding and application of spectral studies, reviews the properties and genesis of BIF- hosted iron deposits, describes existing studies that have integrated spectral studies into iron ore exploration, and details the planned research strategy for testing the hypothesis that BIF- hosted iron deposits have zoned alteration minerals surrounding high-grade iron ore that are detectable using spectral analytical techniques.

2. Background information

2.1 Introduction

Iron ore exploration is influenced by our understanding of geological processes for iron ore formation (i.e. genetic models) plus the availability of effective technologies for the detection of iron ore bodies. Several genetic models exist for the formation of high-grade iron ore deposits, including syngenetic (Lascelles 2006a), supergene-metamorphic (Morris 2007), and more recently the supergene-modified hypogene model (Barley et al. 1999, Taylor et al. 2001a). Each model may have validity, at least in certain districts. Presently, a more holistic “Mineral Systems” approach (Wyborn et al. 1994) is being applied to the study of iron ore systems. This approach attempts to describe the genesis of a deposit along its path of formation, from the source of fluids and metals, the processes for fluid migration, deposition of metals, to the downstream fluid outflow related to the system. Most recent

literature which applies this approach to BIF-hosted high-grade iron ore is in (Angerer submitted). It presents a knowledge gap presently exists in the defined source of these hydrothermal fluids, their composition, and how these fluids interacted with BIF and surrounding country rocks. Hydrothermal alteration mineral assemblages in BIF and country rocks may constrain the composition of the fluids responsible for mineralisation. Alteration zones associated with high-grade hypogene iron ore have not yet been fully characterised. Newly developed spectral technologies, such as the HyLogger, have the potential to assist with the high-resolution characterisation of zoned pathfinder minerals surrounding high-grade iron ore.

2.2 Available spectral techniques for the detection of mineral abundance and mineral chemistry in rocks

Minerals are defined by their range in elemental composition. Spectrometry can be used to detect these variations by using the reflectance and emissivity spectra of the minerals (Clark 1984, Hunt 1977). A rapid expansion in the application of spectrometry has occurred in Earth Science research during the last few decades in that geochemical and geophysical processes in the Earth are now being modeled using new spectral technologies in combination with the more conventional methods (e.g. whole rock and trace element geochemistry). Spectral data are used to identify the mineral abundance and mineral chemistry for different rock types and alteration patterns in outcrop and samples collected from beneath the present erosional surface. There are multiple spectral techniques and detectors that are used for the identification of mineral assemblages in rocks. These modern techniques have been reviewed by several recently studies, including (Duuring et al. 2012, Haest et al. 2010, Moghtaderi et al. 2007, Mhopjeni 2012). The section below briefly outlines the key features of spectral sensors, divided into detectors that are located in a *remote* position to the sample, to detectors located in a *proximal* position.

2.2.1 Remote sensors: ASTER and HyMap

Hyperspectral remote sensors collect images of the Earth's surface through airborne, satellite- based or ground based methods, with each image representing a band of the electromagnetic spectrum. The combination of these bands creates a three dimensional image, which is useful to identify mineral assemblages and detect significant ore deposits. The Advanced Space borne Thermal and Reflection radiometer (ASTER), on

board NASA's Earth Observing System satellite, Terra, was launched in 1999 for the purpose of creating high resolution images of the Earth's surface temperatures, emissivity, reflectance and elevation. The multispectral ASTER measures 14 bands of reflectance and emitted electromagnetic radiation from the Earth's surface and atmosphere. Three bands are in the visible and near infrared radiation (VNIR) with spatial resolution of 15 m, six bands record proportions of shortwave infrared radiation (SWIR) with spatial resolution of 30 m, and five bands record thermal infrared radiation (TIR) with a resolution of 90 m (Kahle et al. 1991).

ASTER image analysis is a useful and well-established method for mapping mineral and alteration surface patterns for a variety of ore deposits. Applications of this ASTER image analysis for the detection of ore bodies include orogenic Au (Gabr et al. 2010) Abu-Marawat district of Egypt, Porphyry Cu (Rowan et al. 2006) Reko Diq area of Pakistan, (Di Tommaso and Rubinstein 2007) Infiernillo deposit, Porphyry skarn (Cudahy et al. 2001) Yerington deposit, Pb-Zn-Au (Hewson et al. 2006) Broken Hill-Curnamona district, Hydrocarbons (Fu et al. 2007) Northern Tian Shan and Mn (Hewson et al. 2006) Woodie Woodie deposits. Recently ASTER has been applied to the mapping of minerals and alteration surface patterns of BIF-hosted Fe ore deposits. Examples include the Matthew Ridge prospect in the Jack Hills greenstone belt of the Narryer Terrane, (Maskell 2010) and Weld Range in the Murchison Domain of Western Australia (Duuring et al. 2012). In both studies, ASTER geoscience products are used to identify high-grade iron ore deposits in the respective exploration district. Useful geoscience products include: the ferric iron oxide minerals product (which identifies hematite and goethite), the ferrous iron in silicate and/or carbonate minerals product (e.g. actinolite, chlorite and siderite), and the opaque and ferrous iron oxides and/or sulphides product (e.g. magnetite, pyrite) (Duuring et al. 2012). The ASTER data are useful for the identification of outcrop, definition of rock types and high-grade Fe ore bodies. However, the limitations of ASTER products are the relatively large pixel resolution size, which can exceed the width of narrow high-grade Fe ore zones that are intermittently exposed. For example, the exposed hypogene magnetite and specular hematite ore zones at the Madoonga deposit, Weld Range, are poorly identified with ASTER data (Duuring and Hagemann 2013a).

Hyperspectral detectors, such as the HyMap sensor, record a wider band range than the multispectral ASTER. The HyMap sensor is an airborne hyperspectral device developed

in Australia by Integrated Spectronics Ltd. The HyMap sensor has a 5 m spatial resolution with wide spectral coverage of approximately 126 spectral bands. Identification of minerals can be obtained from the wide spectral coverage of the region due to the higher spectral resolution and signal to noise ratio. In comparison with ASTER data, the HyMap has a higher resolution allowing for the better definitions of narrow Fe ore bodies, plus HyMap data are not as strongly influenced by the presence of vegetation, fire scars, and man-made boundaries (Hewson et al. 2006)

2.2.2 Proximal sensors: HyLogger and ASD

Proximal hyperspectral logging tools such as the HyLogger and ASD (Analytical Spectral Device) have been used to determine spectral reflectance features including the mineralogy, mineral chemistry, and physical characteristic of geological samples. The HyLogger provides a non-destructive and rapid sampling of drilled material (core and chips) with the integration of three instruments: (1) a hyperspectral spectroradiometer, (2) high resolution camera, and (3) a laser profilometer. The HyLogger device uses the mineralogical content of samples to rapidly and accurately define features in the drill hole, such as lithological boundaries and spatial relationships between zoned alteration mineral assemblages. Spectral data obtained using the HyLogger are processed and interrogated using specialise software, “The Spectral Geologist” (TSG). By comparing multiple holes from a single deposit, it is possible to create a 3 dimensional representation of rock types and alteration minerals in a deposit. For example, hyperspectral data collected from drill chips have been recently used to map detailed surface and subsurface zonation in channel iron ore deposits at Rocklea Dome, Hamersley Province, Western Australia (Haest et al. 2012a). This study demonstrated the use of the HyLogging system in building models for the architecture of ore zones, with direct application for exploration and mining channel iron ore deposits. Companies routinely use collected VNIR- SWIR reflectance spectra from the drill core scanned by the HyLogger to characterise their iron ore deposits within the Hamersley province (Haest et al. 2012a).

Several hand-held portable spectrometers exist that can be taken into the field for the collection of data sourced from outcrop. Examples include the Portable Infrared Mineral Analyser spectrometer (PIMA, Integrated Spectronics Pty Ltd), and the Analytical Spectral Devices FieldSpec-3 (ASD, Analytical Spectral Devices Inc.). ASD spectra are collected in three parts, one covering the visible to near-infrared wavelengths and the other two covering the short infrared wavelengths. ASD spectrometer has a wider spectral

coverage than PIMA, providing data in the VNIR to SWIR range, whereas PIMA only covers the SWIR range.

These portable spectrometers can be easily integrated into exploration strategies involving significant ore deposits, and are used to validate ASTER and HyMap data. They are quick and easy to use, giving useful information in less than a minute, in comparison to the HyLogger which involves extensive preparation time, transport and scanning and high costs. Integration of proximal sensors devices at different scales can be useful in the exploration of ore deposits; early exploration is aided by the use of remote surveys and portable devices (ASD, PIMA), whereas latter stages of exploration benefit from the HyLogger scanning of multiple drill holes.

2.3 BIF-hosted iron ore deposits: their properties and models for their genesis

2.3.1 Physical and chemical properties of BIF

Banded iron formations are sedimentary rocks consisting of alternate layers of magnetite and hematite iron oxides and iron-poor shales and chert containing micro bands of iron oxides. In some areas BIFs are enriched by hydrothermal fluids to form high-grade iron-ore deposits. BIF-hosted iron ore deposits of all scales are the products of favourable juxtapositions of multiple structural controlled diagenetic, metamorphic, hypogene hydrothermal, and typically an overprinting later stage of supergene enrichment (Angerer submitted). Paleomagnetic methods suggest a Paleoproterozoic to Mesozoic age for most of the world's high-grade iron ore deposits. Banded iron formations are rich in total Fe (ranging from about 20 to 40 wt. %) and SiO₂ (ranging from 43 to 56 wt. %). CaO and MgO contents range from 1.75 to 9.00 and from 1.20 to 6.70 wt. percent, respectively. Al₂O₃ contents are universally very low, ranging from 0.09 to 1.80 wt. percent (Klein 2005).

2.3.2 Geographical distribution of BIF

Iron-rich sediments have been episodically deposited on the seafloor in large concentrations from the early Archean to modern times (Clout and Simonson 2005, James and Trendall 1982, Gross 1995, Angerer submitted). Global distribution of high-grade iron ore is spatially associated almost exclusively in BIF in most continents. Iron formations show

spatial distributions restricted of their age, forming in early Archean to Neoproterozoic ~3.8-0.6 Ga, displaying extensive heterogeneity of abundance, size, depositional environment and style (Clout and Simonson 2005). High-grade iron-ore fertility is favourable within thick Fe-rich BIF, in contrast thinner cherty BIF show a lower tendency to host significant Fe-enrichment. Giant high-grade iron ore deposits occur in Brazil's Carajas and Quadrilatero Ferrifero mineral provinces, South Africa's Kaapvaal Craton, and Westerns Australia's Hamersley Province and Yilgarn Craton (e.g. Weld Range, Koolyanobbing and Jack Hills). Global distribution of known Archean BIF's is shown in Figure 1, which also displays supracrustal greenstone successions that have been extensively deformed and metamorphosed (Klein 2005).

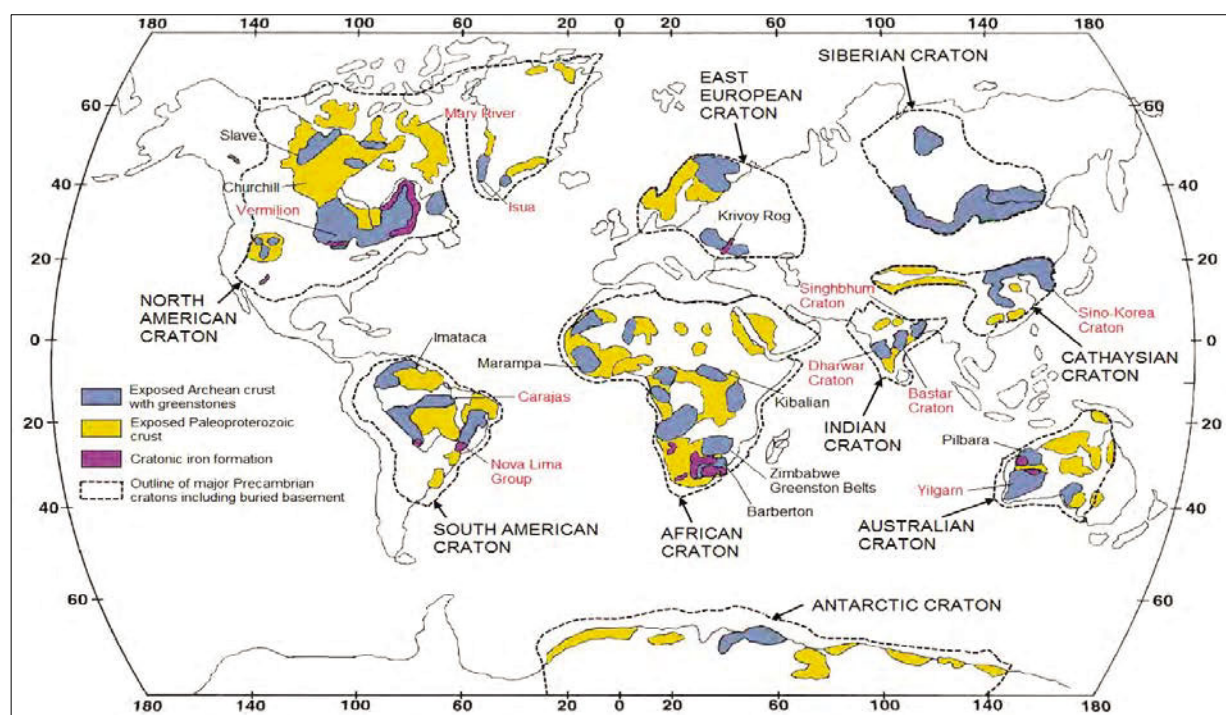


Figure 1: Global distribution of Precambrian crust and Archean banded iron formations (Gutzmer et al. 2008)

2.3.3 Ore genesis models

Although many similarities exist between BIFs and their protorees there is variability in the nature of their high-grade iron ore deposits. This variability can in part be explained by the proposed variety of ore forming processes for iron ore bodies (Clout and Simonson 2005). Several genetic models exist for the formation of high-grade iron ore deposits, including syngenetic (Lascelles 2006a), supergene-metamorphic (Morris 2007), and more

recently the supergene-modified hypogene model (Barley et al. 1999). Each model has strengths and weakness, and certain models may prove to be valid at least locally. Presently, a holistic “Mineral Systems” approach (Wyborn et al. 1994) is being applied to the study of iron ore systems. Within literature (Angerer submitted) show current attempts to apply a mineral system analysis for iron ore by describing the critical processes involved within the ore forming processes of BIF mineralization, which are summarized in Table 1.

Martite-goethite ores are deemed to have resulted from recent supergene enrichment with the replacement of gangue minerals by goethite beneath Mesozoic to Cenozoic weathering profiles; Australia and Indian deposits contain these ore types. Brazilian and Indian high-grade soft hematite ore are most likely the result of supergene processes that involved the leaching of gangue minerals and concentrations of residual hematite (Clout and Simonson 2005, Mukhopadhyay et al. 2008). Microplaty hematite and hard hematite ores, such as in Australia, Brazil, India and North America (Brown 2008, Mukhopadhyay et al. 2008, Figueiredo e Silva et al. 2008, Angerer et al. in press), are more controversial with many authors explaining different processes of their formation due to: (1) supergene hydrothermal fluid events with (e.g. Morris 1980, Morris 1985) or without metamorphic enrichment (Beukes 1986), (2) syn-sedimentary formation of a chert-free BIF (Lascelles 2002, Lascelles 2006b) or (3) hypogene alteration involving deep-seated hydrothermal and/or magmatic fluids (e.g. Dorr 1965, Gutzmer et al. 2002) or shallow meteoric waters (e.g. Taylor et al. 2001b, Beukes et al. 2002) and further upgraded by supergene enrichment (Taylor et al. 2001b, Dalstra and Guedes 2004b, Angerer et al. in press).

2.3.4 Structural controls for Fe mineralisation

High-grade iron ore deposits are structurally complex and exhibit a variety of structural features including extensional normal faults and compression thrust faults. Not only do structures provide a vital pathway for fluid flow they are also important in assisting the preservation of large deposits. Rocks that have undergone brittle-styles of deformation commonly display fault and fracture structures which create permeable pathways for the movement of ore forming fluids. Deposits within the Yilgarn Craton display evidence for fault-controlled fluid flow in ore genesis. Within the Koolyanobbing and

Weld Range deposits, strike-slip faults host the late stage microplaty-hematite mineralisation, which forms from later hydrothermal fluids. Iron ore bodies that generally occur in fold-thickened-hinge areas in rocks have most likely experienced ductile deformation. Thickened-hinge areas are often the key constraints on determining economic or uneconomic primary BIF deposits.

2.3.5 Ore forming fluids and metal precipitation

A variety of hydrothermal fluids are important for the upgrade of BIF (~30 wt% Fe) to high-grade iron ore (~65 wt% Fe). Within high-grade iron ore deposits hosted in BIF fluids are characteristically silica-poor and saline-rich, derived from deep-seated hydrothermal and supergene associated fluids. Fluids that have the ability to successfully dissolve large amounts of quartz within BIF must be derived from an external source due to under saturation of silica within the fluids. Hydrothermal fluids are derived from deep within the Earth's crust and depending on the deposits these fluids can derive from varying sources such as, deep-seated metamorphic, magmatic, basinal brines and ancient seawater. Supergene fluids include recent descending meteoric waters or 'supergene groundwater'. Dissolution of silica results from the large influx of low-silicate bearing fluids; many models exist to explain this process. Including the dewatering of sediments resulting in silica escaping up faults (Lascelles, 2006), Metamorphic fluids leaching gangue minerals (Morris, 1985), basinal brines dissolving chert (Angerer, submitted), and magmatic fluid interaction with country rock creating Fe-rich chlorite and talc (Duuring et al. 2012), Meteoric water occurs as both ancient deep, circulating fluids and surface derived meteoric waters. Supergene processes that upgrade BIF iron rich minerals are developed as deep supergene ground water interaction and weathering of near surface dehydration and hydration zones. This late stage enrichment (Lobato et al. 2008, Thorne et al. 2009) describes ascending deep supergene enrichment of iron within the BIF and descending shallow supergene destroying preserved BIF and BIF textures with goethite formation present. The sources and fluid rock conditions for ore forming processes are still under debate in many recent studies, the presence of more than one fluid is a favoured model in most studies.

Ore genesis models for these deposits are dominated by two processes, silica-loss and oxidation events. SiO₂ is removed as silica under-saturated fluids pass through the BIF in favourable pathways of high permeability. In turn, the subsequent oxidation of iron bearing

minerals is apparent within different alteration zones due to multiple fluid flows. Iron-bearing minerals are present within the BIF before ore-forming processes take place. Enrichment and upgrade of iron to high grade iron ore is controlled by ascending and descending saline fluids. Protolith BIF is dominated by microcrystalline hematite and Fe-rich siderite, silicate and ankerite. Major ore minerals within the enriched BIF include fine-grained hematite and martite, with minor amounts of magnetite, kenomagnetite, and/or goethite.

Table 2: Mineral systems approach to iron ore in Archean and Paleoproterozoic BIF of Western Australia (Angerer submitted)

Critical processes	Fe fertility (large accumulation of iron oxides facies in BIF with >25%wt FE)	Si-dissolving fluids	Permeability for fluid flow	Exhumation and surficial modification	Preservation
Principal processes	<ol style="list-style-type: none"> 1. Achaean to Paleoproterozoic granite-greenstone setting 2. Achaean to Paleoproterozoic basinal/continental shelf setting 3. Paleo-craton margins 	<ol style="list-style-type: none"> 1. 3>pH>9 Fluid on heating path 2. Brine from stratigraphic source rock 3. Fluid interacting with mafic-ultramafic rock 4. Fluid interacting with carbonaceous rocks 5. Long lasting oxidising groundwater flow 	<ol style="list-style-type: none"> 1. Focussed flow to achieve high fluid-rock ration 2. Source-sink connectivity 3. Mineralogical permeability 	<ol style="list-style-type: none"> 1. Long term surficial exposure to tropic-subtropic climate and discharge by groundwater 2. Minimised post-ore weathering 3. Exhumation history 	<ol style="list-style-type: none"> 1. Absence of glaciations 2. Hard capping 3. Extensional structural position 4. Sedimentary cover
Targeting elements	<ol style="list-style-type: none"> 1. Youanmi and Narryer terrane, greenstone successions (district) 2. Thick and laterally extensive BIF (camp, deposit) 3. Sutures(district) 	<ol style="list-style-type: none"> 1. Distal to proximal ultramafic rocks proximity to granites (fluid driver) carbonate rich/Si poor country rocks, evaporate in sequence 2. Evaporate in sequence, stratigraphy collapse by lithology dissolution 3. Mafic ultramafic country rock 4. Black shale as country rock 5. Surface-near, oxidised BIF 	<ol style="list-style-type: none"> 1. Lithology contrasts, fold patterns, lithology contrasts, structurally reactivated 2. Compressional faults, transcurrent faults, extensional faults, BIF grain size (metamorphism), complex gangue mineralogy 3. 	<ol style="list-style-type: none"> 1. low-mid paleolatitudes 2. climate modification after ore formation 3. exhumed prospective alteration zones 	<ol style="list-style-type: none"> 1. mid to low latitude 2. position in high morphological relief 3. position at extensional faults, in graben structures 4. colluvium basin, salt lakes

2.4 BIF-hosted iron ore deposits: ore forming fluids

2.4.1 Metamorphic, hypogene alteration and supergene alteration

Alteration studies have proved to be important indicators in providing insight into the nature of fluids and the formation of specific ore deposits. Determining characteristic alteration patterns and pathfinder minerals will aid exploration to become focused towards these parameters. The scarcity of studies in this area contributes to the difficulty in recognising these patterns within the supergene weathered BIF (Dalstra and Guedes 2004a). The most pronounced similarity of BIF-hosted high-grade iron ore deposits is their similar paragenetic sequence of iron oxides. In broad terms, iron oxides change from microcrystalline/dusty hematite, to hydrothermal magnetite within the distal alteration zones. Intermediate zones may be characterised by martite replacing magnetite, displaying kenomagnetite and hematite. Proximal zones are typically classified into textures of hematite (microplaty, platy, patchy, bladed and tabular) (Lobato et al. 2008).

Fluid alteration histories of high-grade iron ore deposits show very similar characteristics with at least two stages of hydrothermal alteration with a later stage of supergene enrichment. Hydrothermal alteration within different model deposits of significant high-grade iron ore show significant similarities in iron oxide paragenetic sequences with abundant open-spaced filling and replacement textures, lack of penetrative fabric in alteration lithology units and high grade iron ore and porosity and brecciation importance accommodating volume loss. Hydrothermal alteration stages include (1) removal of silica in the BIF protolith leaving a residual massive magnetite protore and (2) the formation of microplaty hematite ore and martitisation. Supergene alteration is a more recent stage of alteration of BIF which results in the dominance of soft hematite ore. Supergene processes typically overprint most hypogene deposits and show the final stages of enrichment and depletions. Remaining silicate minerals are removed by descending fluids and replaced with various clay minerals, along with the dissolution of apatite and phosphate minerals and the upgrade of hematite to goethite. (Figure 2) displays these characteristic enrichments and depletions of mineralogical assemblage alterations within the supergene-modified hypogene model (Barley 1999).

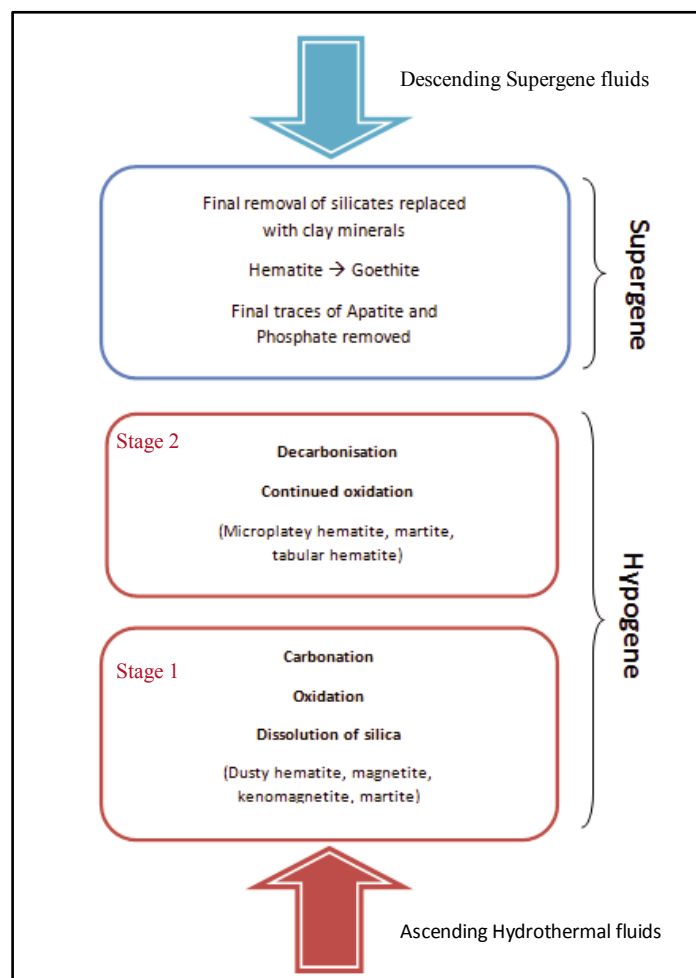


Figure 2: Major characteristics of hypogene and supergene alteration of BIF (Lobato et al. 2008, Angerer et al. submitted)

2.5 BIF-hosted iron ore in Yilgarn Craton, Western Australia: geological setting and ore forming processes

Recent attempts have been made to identify common Archean BIF-hosted iron ore deposits located within the Yilgarn Cratons, Paleo to Meso- Archean greenstone belts in the Narryer and Youanmi terranes. These studies attempt to focus on understanding the controls of greenstone belt-hosted iron ore and exploit the increasing number of depleted resources. High-grade iron ore deposits with the Yilgarn Craton are the result of several overlaying hypogene ore-forming stages. Koolyanobbing and Weld Ranges deposits contain significant high-grade deposits which show similar hydrothermal histories resulting in the enrichment of

BIF to iron ore. These deposits and other significant high-grade iron ore formations are displayed in Figure 3 (Fig. 4; Angerer et al. in press).

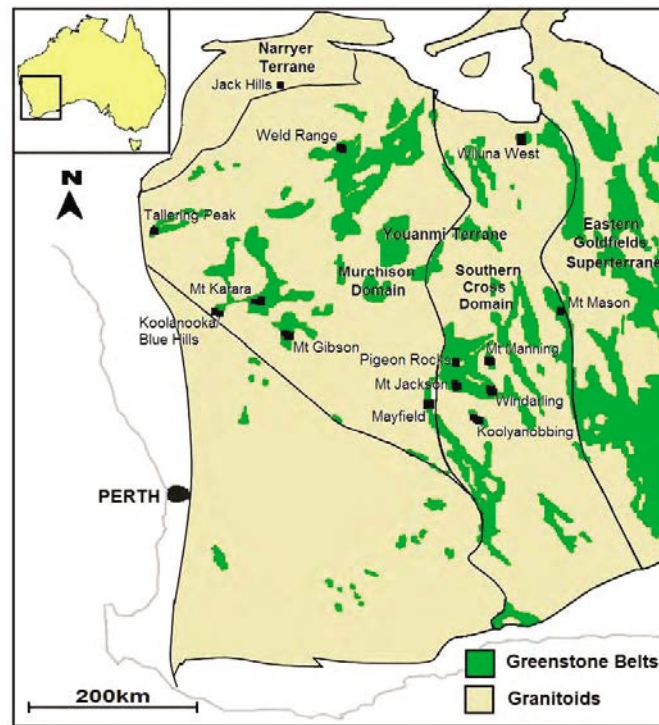


Figure 3: Simplified geological map of the Yilgarn Craton displaying important iron ore deposits (Lascelles 2007, Cooper 2009)

2.5.1 Koolyanobbing (Southern Cross Domain)

Koolyanobbing iron ore deposit is situated within the Koolyanobbing greenstone belt is hosted with the greenschist facies metamorphosed quartz-magnetite BIF within ~3.05-2.93 Ga greenstone succession. Four stages of ore formation and hydrothermal alteration took place at Koolyanobbing (Angerer & Hageman, 2010; Angerer et al 2012a). An early stage of Fe-Mg (\pm Ca) metasomatism caused localised alteration of the quartz-magnetite BIF to a Fe-rich carbonate-magnetite BIF. Subsequent localised hydrothermal quartz-magnetite mineralisation occurred in reverse faults breccia and fractures followed strike slip fault controlled late hydrothermal alteration involving formation of specular hematite and martitisation. A final stage of supergene enrichment sees the leaching of carbonate and quartz being replaced by goethite and oxidation of magnetite to martite (Angerer et al. 2010).

2.5.2 Beebyn and Madoonga (Murchison Domain)

Metamorphosed greenschist facies BIF in the Weld Range greenstone belt are host to two known high-grade iron ore deposits: Madoonga and Beebyn. These deposits are located within separate quartz-magnetite BIF units of the ~2752 Ma Wilgie Mia Formation. Beebyn high grade iron ore deposits BIF units are bounded by mafic volcanic rocks which intruded the original Wilgie Mia formation. Rocks in this area have been intensely deformed with three generations of folds with ductile shear zones, and several later stages of brittle faults (Duuring and Hagemann 2013b). Three main stages of hydrothermal fluid alteration is described by (Duuring and Hagemann 2010) with initial replacement of quartz-rich bands by ferroan dolomite. Dissolution of ferroan dolomite, followed by the local addition of hydrothermal magnetite-carbonate, and deposition of coarse-grained chlorite with specular hematite in fault zones, together with the martitisation of earlier magnetite-rich bands.

2.5.3 Yilgarn BIF-hosted high-grade iron ore: ore forming processes

Comparison of high-grade iron ore deposits within the Yilgarn Craton Paleo to meso-Archean greenstone belts in the Narryer and Youanmi terranes has demonstrated various similarities of hydrothermal alteration histories of mineralisation. Characteristic steps of enrichment display carbonate alteration replacing original quartz bands of BIF, hydrothermal leaching of carbonates and/or iron oxides parallel with the deposition of secondary magnetite in well developed zones of high permeability (reactivated faults or shear zones) which form along BIF margins. Dominate faults host specular hematite \pm carbonate \pm quartz alteration forming during late transpressional to transtentional deformation in the Yilgarn Craton. These processes do not appear to be greatly affected by the peak metamorphic facies conditions affecting the BIF (range from lower-greenschist to lower-amphibole facies), as well as the age of deposition. Koolyanobbing and Weld Range show similarities in the alteration styles and ore genesis processes, this may be a result of their comparable BIF depositional facies (BIF units surrounded by mafic volcanic rocks) and their similar tectonic evolution (Fig 4) (Angerer et al. 2010). Some regional variations exist such as growth of lepidoblastic hematite in Windarling form a result of varying redox conditions during formation fluid-rock interactions.

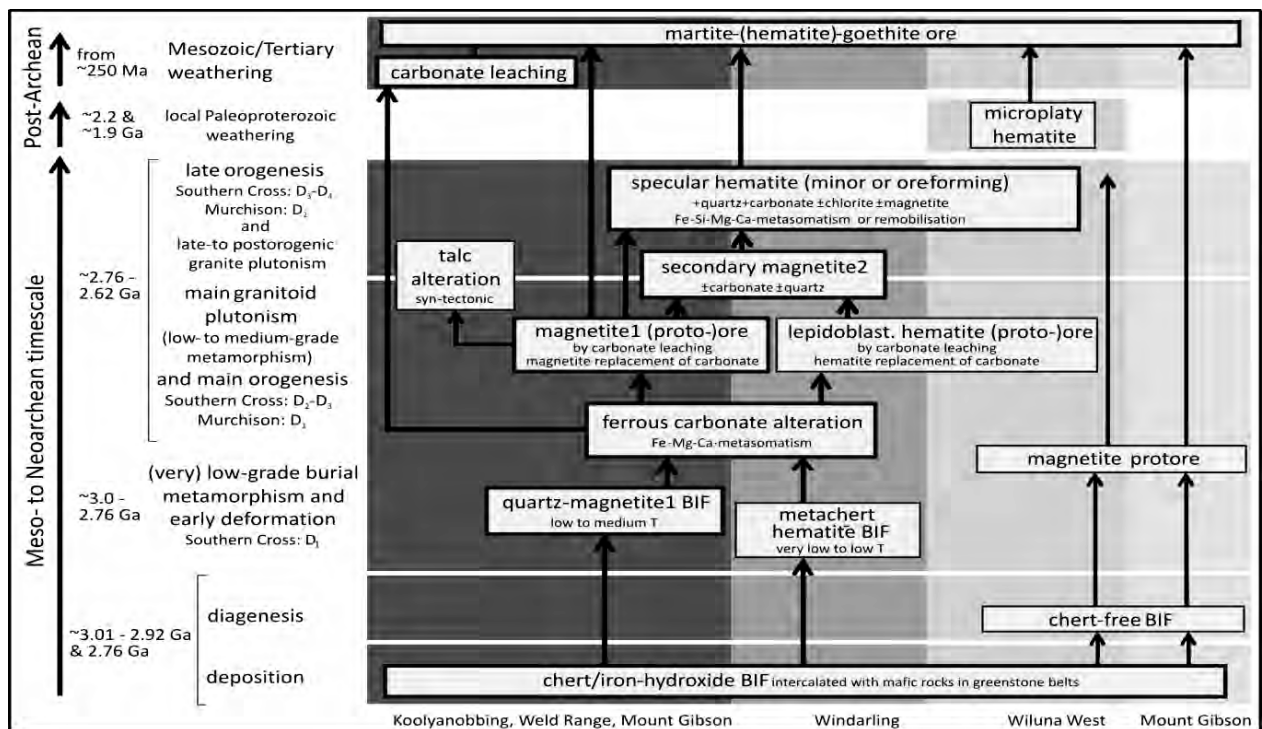


Figure 4: Integrated flow chart displaying processes of iron mineralisation for selected BIF-hosted deposits in the Yilgarn Craton. Grey shading corresponds to a series of iron-enrichment steps displayed in specific deposits, most common deposits in bolded boxes (Angerer and Hagemann 2010)

2.5.4 Discussion: ore forming processes of Yilgarn Craton BIF-hosted iron ore

Important ore forming processes in the Yilgarn Craton are a product of several hypogene ore-forming stages and later overprinting supergene enrichments which took place throughout the orogenic cycle during meso-late Archean time. Comparison of ore genesis models for high-grade iron ore deposits in the Yilgarn Province display similar processes of ore formation. Within the Yilgarn Craton similar critical processes of iron formation include an initial sedimentary iron fertility of the BIF, an Si dissolving fluid, high permeability at micro-to district scales, surficial modifications and preservation by colluvial cover, structures or surficial modifications. A description of common ore types within the Yilgarn Craton is given in Table 2, describing alteration mineral assemblages in the BIF and mafic country rock with relevant examples. Several distinct gaps in knowledge exist when describing the iron ore mineral system. Key unknowns include the (1) the favourable geodynamic setting for Fe BIF, (2) pre-ore BIF alterations facilitation ore formations, (3) successful detection of alteration haloes, (4) fluid source and fluid-rock conditions, (5) timing of alteration events, (6)

county rock studies in defining fluid-rock conditions, and (7) the preservation and detection of concealed ore. Driven by the increasing demand of steel worldwide and our constant need for new scientific ideas a successful mineral system analysis of iron ore genesis is needed to assist in predictable exploration of these significant deposits. Future work in the Yilgarn will concentrate on constraining hydrothermal fluid characteristics and possible sources for BIF-hosted deposits.

Table 3: Description of common ore types, defining their fluid origin, alteration mineral assemblages in BIF and mafic country rock with examples from the Yilgarn Craton.

Ore type	Fluid origin	Alteration mineral assemblage (BIF)	Yilgarn deposits	Alteration mineral assemblage in mafic country rock	Reference
Residual magnetite	Hypogene	Leaching of hypogene carbonate minerals and residual enrichment in magnetite Increase in K ₂ O, MgO, P ₂ O ₅ , Fe Decrease in SiO ₂	Madoonga deposit	Proximal zones: primary igneous minerals replaced by ferroan chlorite Local addition of talc and magnetite Increase in Fe, P ₂ O ₅ decrease in CaO, K ₂ O, Na ₂ O	(Duuring et al. 2012)
Magnetite veins	Hypogene	Addition of magnetite and talc loss of quartz	Weld range district Madoonga Beebyn	Proximal zones: primary igneous minerals replaced by ferroan chlorite Local addition of talc and magnetite Increase in Fe, P ₂ O decrease in CaO, K ₂ O, Na ₂ O	(Duuring and Hagemann 2013a, Kenworthy 2008)
Specular hematite	Hypogene	Addition of hematite, minor quartz and chlorite	Beebyn, Madoogna (weld range) Wiluna west (Joyner's Find greenstone belt) Koolyanobbing (Koolyanobbing greenstone belt)	Proximal zones: primary igneous minerals replaced by ferroan Chlorite (Duuring and Hagemann 2011) Local addition of talc and magnetite Increase in Fe, P ₂ O ₅ decrease in CaO, K ₂ O, Na ₂ O	(Duuring and Hagemann 2013b, Duuring and Hagemann 2013a)
Goethite-hematite	Supergene	Goethite and hematite-rich zones Increase in Fe, P ₂ O ₅ ; decrease in SiO ₂	Weld range district Matthews Ridge	Mafic igneous country rock (BIF) Replacement of primary and hypogene minerals by hematite, goethite, kaolinite	(Duuring et al. 2012)
Detrital	Supergene	Replacement of fragments by goethite and hematite; cemented by goethite Increase in Fe, , P ₂ O ₅ ; decrease in SiO ₂	Weld range district Madoonga Beebyn		(Duuring et al. 2012)

2.6 Examples of spectral studies applied to the exploration for BIF-hosted iron deposits

2.6.1 Weld Range greenstone belt, Western Australia: the use of ASTER data

ASTER has been previously used to map mineral and geochemical zonation associated with a variety of ore deposits. Recent application of ASTER have been directed towards mapping the mineral and geochemical alteration of high-grade iron ore deposits within the Yilgarn Craton (e.g., Koolyanobbing and Windarling, (Angerer and Hagemann 2010) Jack Hills deposit (Maskell 2010), Weld Range deposits (Duuring and Hagemann 2011). The Weld Range greenstone belt is host to several high-grade iron ore deposits, Beebyn and Madoonga, which are located in separate quartz- magnetite BIF units of the ~2752 Ma Wilgie Mia Formation (Angerer et al 2010). The use of ASTER image products where used in this district to locate outcrop, discriminate major rock types and locate Fe ore bodies (Figure 5). The iron ore bodies in Weld Range is best identified by their ferric iron to silica index and the opaques to silica index, ASTER images where useful in detection of surfaces which show enrichment of opaque Fe oxide minerals with low silica content. The study of Beebyn and Madoonga in the Weld Range district proved that remote spectral techniques are useful in district scale for the exploration of iron ore bodies hosted in BIF.

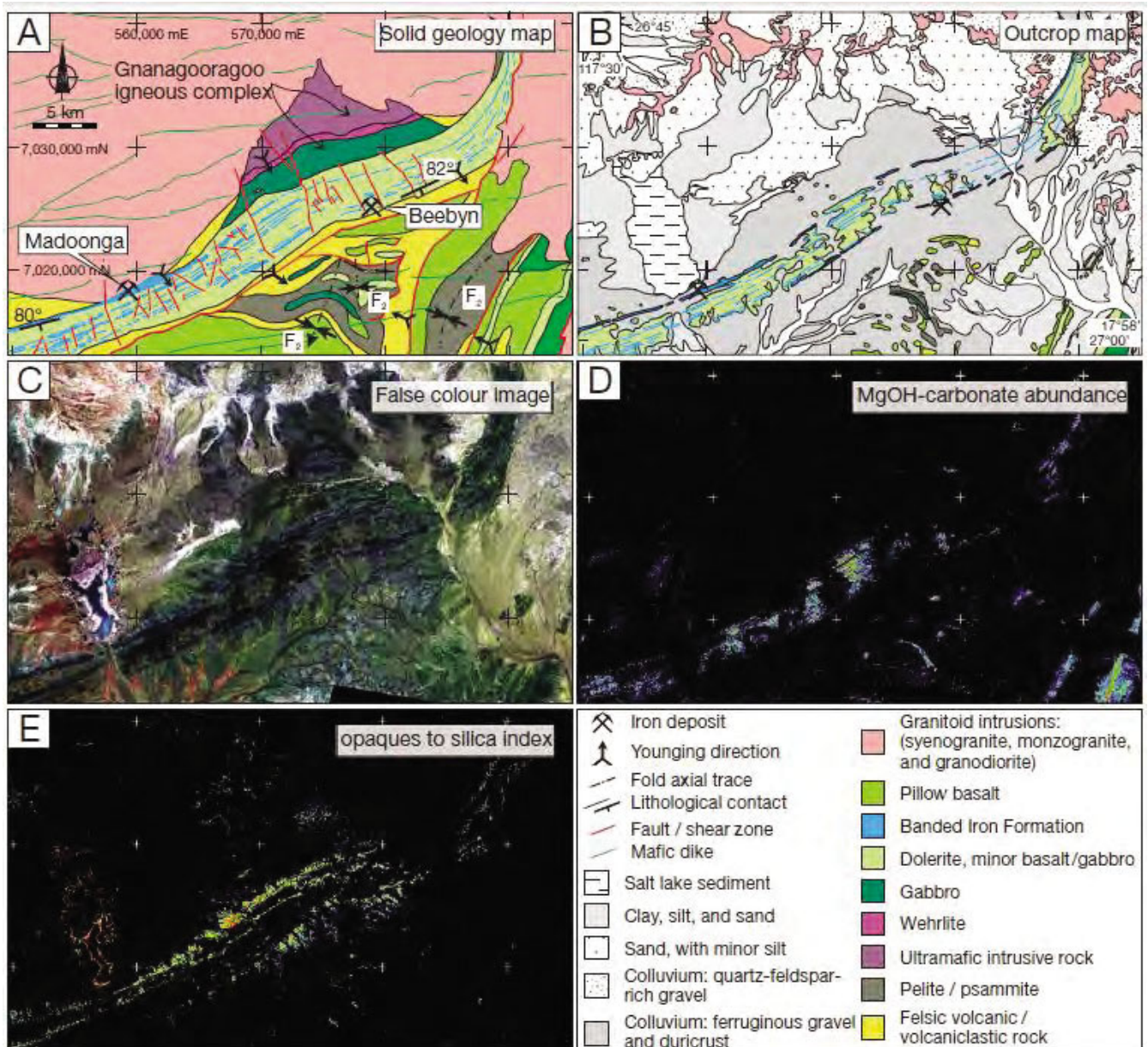


Figure 5: Geology and ASTER image products for Weld Range district A) geology map; B) outcrop geology map; C) ASTER false colour image; D) ASTER ferrous iron content in MgOH minerals and carbonates image product that shows the distribution of opaque objects (Fe and Mn oxides, carbon, sulphide minerals and fire scars (Duuring et al. 2012).

2.6.2 Delineation of Channel Iron Deposits at Rocklea Dome: using HyLogger data

Channel iron deposits (MacLeod, 1966) are the second most significant source of iron ore mined in north western part of Western Australia (Morris and Ramanaidou, 2007). Mineralogy of channel iron deposits of the Rocklea Dome have been studied with the use of the HyLogger system from 180 reverse circulation and 14 diamond drill cores (Haest et al. 2012a). Hyperspectral data were collected from drill core using the HyLogger system; this was used to map detailed surface and subsurface mineral zonation in the Rocklea Dome channel iron deposits of the Hamersley Province, Western Australia. The visible-near shortwave infrared reflectance spectra are designed to present accurate estimates of mineral abundances and compositions from infrared spectroscopic, reflectance data. Mineralogy determined from this study included a dominant goethite content of both vitreous and ochreous forms, lesser amounts of hematite and variable amounts of quartz, kaolinite, smectite, and some carbonates (Figure 6). Hyperspectral data were used to characterise the architecture of Rocklea Dome channel iron deposits, with some implications for exploration, mining and ore genesis.

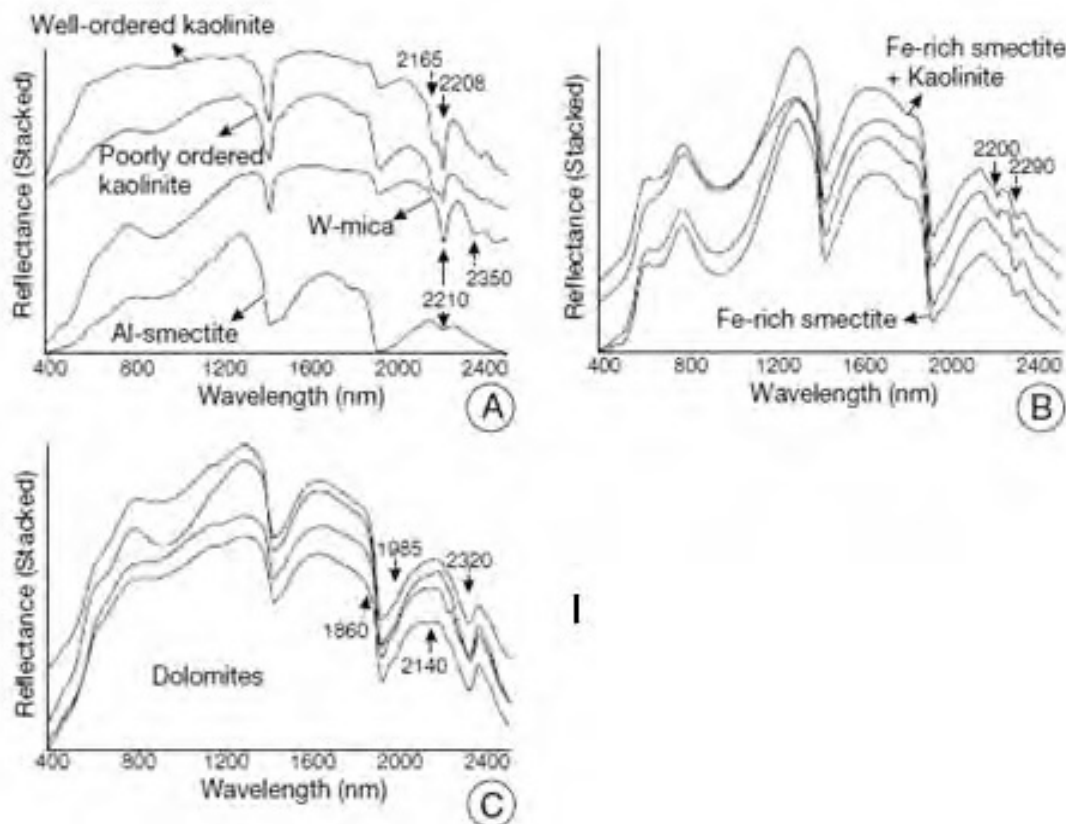


Figure 6: Rocklea channel iron ore deposits: Stacked reflectance plot of A) end-member spectra of Al- OH clay samples B) Fe-rich smectite spectra C) dolomite spectra with typical carbonate absorption features (Haest et al. 2012a)

2.6.3 Discussion: Integration of spectral technologies in ore deposit exploration

The past few decades have seen the rapid expansion of spectrometry in Earth sciences. A variety of spectral techniques are used in to aid the successful exploration of significant ore deposits, with recent application to high-grade iron ore deposits. Previous identification of mineral assemblages in BIF-hosted high grade iron ore with use of standard logging procedures does not provide us with all the critical information required to acquire of full understanding of the deposits. it is lacking accurate information on mineralogy, specifically contents and physicochemistries of iron oxides, clays, carbonates and silica (Haest et al. 2012b). Studies of Rocklea dome channel iron deposits display that spectra obtained from hyperspectral scanning, HyLogger, can be used to build the three-dimensional architecture of ore bodies with applications towards exploration and mining. ASTER data obtained from Weld Range demonstrate the rapid cost-effective and efficient means of producing and ranking exploration targets which are located in areas with restricted physical access. Both these studies show the importance of integrating remote spectral sensing, geological survey and hyperspectral scanning techniques to present a modern and efficient way of accurately searching for significant high-grade iron ore deposits on a global scale. Future exploration of ore bodies is expected to become more efficient with the rapid evolution of spectral technologies, and with this we can obtain a better understanding of the ore forming processes which are present in the mineralisation of significant ore bodies

3. Aims and objectives

This study will test for the presence of pathfinder minerals associated with high-grade iron ore in BIF and mafic country rocks at Mt Richardson in the Yilgarn Craton. One representative diamond drill hole that intersects high-grade iron ore will be scanned with the HyLogger and the resulting spectra interpreted. Scanning of the core will allow the accurate determination of indicator alteration mineral and mineral chemistry from the recorded spectra. The results will help constrain the composition of the ore fluids responsible for mineralisation and provide important information for refining genetic models for iron ore deposits.

4. Significance and Outcomes

The characterisation of alteration minerals and mineral chemistry in alteration halos to BIF-hosted iron ore will help constrain genetic models and provide a list of pathfinder minerals for exploration. The interpretation of HyLogger data will aid the interrogation of existing remotely acquired spectral datasets (e.g. ASTER and HyMap) for the Mt Richardson area. The existing interpretations presently suffer from a lack of mineral chemistry input constraints, which are derived from sample analysis (e.g. HyLogger and hand-held analytical spectral devices, ASD).

5. Methodology

PK11DD001). The hole will be transported from Mt Richardson to the GSWA's Core Library in Carlisle, Perth. The core will be prepared, washed, fitted and dried before it undergoes hyperspectral scanning with CSIRO's HyLogging device. The core will experience a non-destructive, complete scan with the HyLogger, which collects spectra for the core to use in determining hydrothermal alteration zonation and relate them to changes in geochemistry of the rocks. Each spectra represents electromagnetic radiation that is projected at the core, reflected by the surface of the core, and detected by the HyLogger. Each mineral has a characteristic spectral signature and with the aid of spectral devices these signatures can be determined by observing troughs and peaks in the spectra equate to minerals present and their chemistry. The spectral will be interpreted in conjunction with conventional detailed logging of the core (i.e. lithological descriptions, alteration zonation, structures). The spectral data will be interpreted using specialised software ('The Spectral Geologist', TSG software).

Samples will be taken from the drill core for geochemical analysis and thin section preparation. Identified alteration zones in BIF and mafic country rocks will be tested independently by the selection of hand specimens for geochemical analysis, thin section preparation, and potentially X-ray diffraction (XRD) analysis. Selected samples of both the least altered protolith and hypogene, supergene altered rock will be crushed into powders and analysed to determined major iron oxides and trace elements in the rocks. In testing the protolith we aim to determine the primary chemistry and rock type of original rock which will give us something to compare to the altered rocks. Hypogene and supergene altered rocks are

tested with a combination of immobile and mobile element geochemistry using methods described by Grant 1986 mass balance equation. Doing this we will calculate the net additions and losses in major and trace elements which in turn can determine the changes in rock chemistry of the alteration zones.

The scanning electron microscope (SEM) will be used to validate the presence of minerals which have been previously identified by the HyLogger as well as their chemical composition. Using the SEM I will determine mineral abundance and relationships in alteration zones while the EDS will identify quantitative mineral compositions. Integrating conventional logging of core, thin section petrography and data obtained from the use of spectral technologies will provide this project with accurate data to identify the alteration zonation and their mineral assemblages and chemistries.

6. Timeline

Table 4: General Timeline of this research project throughout the year and the ordering and estimated occurrence of methods used.

Activity	J	F	M	A	M	J	J	A	S	O	N	D
Shipment of core to Perth			X									
Project outline			X									
Research proposal			X									
Preparation of core (washing, drying, fitting)			X									
Logging core				X								
Scanning core				X								
Detailed logging and sample collection for geochemical analysis					X							
Preparing samples (cut core, packing, send to labs)					X							
Thin section processing					X	X						
Geochemical analysis					X	X						
XRD (training and sample preparation)						X						
SEM							X					
Final research thesis											X	
Research seminar											X	

7. Budget

Table 5: Estimate of research project budget, individual methodology estimations present.

Task/methods	Anticipated Expenditure	Total cost
Transport of core to Perth	\$300	\$300
Scanning core (200m)	\$3,000 per 100m	\$6000
Thin section preparation	\$50 per slide	Maximum of 30 slides
		\$1,500
Geochemical analysis (XRF, ICPMS)	\$100 per sample	Maximum 20 samples
		\$2,000
XRD and SEM analysis	\$2,000 per 12 months	\$2,000
Thesis preparations (printing, stationary, tools etc)	\$200	\$200
Approximated cost of project		\$12,000

8. Appendix

**References follow the style of the Australian Journal of Earth
Sciences (AJES)**

9. References

- ADAMS J. B. & FLILIC A. L. 1967 Spectral reflectance 0.4 to 0.2 microns of silicate rock powders, *Journal of geophysical research*, vol. 72, pp. 5705-5715.
- ANGERER T., *et al.* 2010 BIF-related iron ore in the Yilgarn Craton, Western Australia: Geological setting and ore forming processes. In TYLER I. M. & KNOX-ROBINSON C. M. eds. 5th International Archean Symposium: Abstracts. pp. 277-280. Perth, Western Australia: Geological Survey of Western Australia.
- ANGERER T., DUURING P., HAGEMANN S.G., THRONE W. AND MCCUAIG, T. submitted A mineral system approach to iron ore in Archaean and Paleoproterozoic BIF of Western Australia. In: Ore Deposits in an Evolving Earth, Geological Society, London, Special Publication, vol. 393.
- ANGERER T. & HAGEMANN S. G. 2010 The BIF-hosted high-grade iron ore deposits in the Archaean Koolyanobbing greenstone belt, Western Australia: Structural control on synorogenic- and weathering-related magnetite-, hematite-, and goethite-rich iron ore, *Economic Geology*, vol. 105, pp. 917-945.
- ANGERER T., HAGEMANN S. G. & DANYUSHEVSKY L. V. 2012 Geochemical evolution of the Banded Iron Formation-hosted high-grade iron ore system in the Koolyanobbing greenstone belt, Western Australia, *Economic Geology*, vol. 107, pp. 599-644.
- ARNDT N. T., NALDRETT A. J. & HUNTER D. R. 1997 Ore deposits associated with mafic magmas in the Kaapvaal Craton, *Mineralium Deposita*, vol. 32, no. 4, pp. 323-334.
- BARLEY M. E., *et al.* 1999 Hydrothermal origin for the 2 billion year old Mount Tom Price giant iron ore deposit, Hamersley Province, Western Australia, *Mineralium Deposita*, vol. 34, no. 8, pp. 784-789.
- BAU M. & ALEXANDER B. W. 2009 Distribution of high field strength elements (Y, Zr, REE, Hf, Ta, Th, U) in adjacent magnetite and chert bands and in reference standards FeR-3 and FeR-4 from the Temagami iron-formation, Canada, and the redox level of the Neoarchean ocean, *Precambrian Research*, vol. 174, pp. 337-346.
- BEUKES N. J. 1986 The Transvaal sequence in Griqualand West. In ANHAEUSSER C. R. & MASKE S. eds. Mineral Deposits of Southern Africa. pp. 819-828. Johannesburg: Geological Society of South Africa.
- BEUKES N. J., GUTZMER J. & MUKHOPADHYAY J. 2002 The geology and genesis of high-grade hematite iron ore deposits, *Australian Institute of Mining and Metallurgy Publication Series 7/2002*, pp. 23-29.
- BROWN P. E. 2008 Brief History of High-Grade Iron Ore Mining in North America (1848-2008). In HAGEMANN S. G., *et al.* eds. Banded Iron Formation-Related High-Grade Iron Ore. pp. 22-45. Reviews in Economic Geology.
- CASSIDY K. C., *et al.* 2006 A revised geological framework for the Yilgarn Craton, Western Australia. pp. 8. Perth: Geological Survey of Western Australia.
- CHEN S. F. 2004 Geology of Marmion and Richardson 1:000000 sheets, *1:100000 Geological Series Explanatory Notes*, vol. Western Australia Geological Survey, p. 27.
- CLARK A. M. 1993 Hey's Mineral Index, Mineral Species, Varieties and Synonyms. (3rd edition). Chapman and Hall, London.
- CLARK R. N., & ROUSH, T.L 1984 Reflectance Spectroscopy: Quantitative Analysis Techniques for Remote Sensing Applications, *J. Geophys. Res.*, vol. 89, pp. 6329-6340.
- CLOUT J. M. F. & SIMONSON B. M. 2005 Precambrian iron formations and iron formation-hosted iron ore deposits, *Economic Geology*, vol. 100, pp. 643-679.
- COOPER R. W. F. D. J. 2009 Iron ore deposits of the Yilgarn Craton - 2009 (1:1500000), *Geological Survey of Western Australia*.
- CUDAHY T. & BARRY P. S. 2002 Earth magmatic-seawater hydrothermal alteration revealed through satellite-borne Hyperion imagery at Panorama, Western Australia. IEEE 2002 International Conference on Geoscience and Remote Sensing. pp. 590-592. Toronto.

- CUDAHY T. J. 1997 PIMA-II spectral characteristics of natural kaolins, *Exploration and mining report CSIRO/AMIRA*.
- CUDAHY T. J., *et al.* 2008 Next Generation Mineral Mapping: Queensland Airborne HyMap and Satellite ASTER Surveys 2006-2008. CSIRO report P2007/364. pp. 153.
- CUDAHY T. J., *et al.* 2001 Mapping porphyry-skarn alteration at Yerington, Nevada, using airborne hyperspectral VNIR-SWIR-TIR imaging data, *Igarss 2001: Scanning the Present and Resolving the Future, Vols 1-7, Proceedings*, pp. 631-633.
- DALSTRA H. & GUEDES S. T. 2004a Giant hydrothermal hematite deposits with Mg-Fe metasomatism: A comparison of the Carajas, Hamersley, and other iron ores, *Economic Geology*, vol. 99, no. 8, pp. 1793-1800.
- DALSTRA H. J. & GUEDES S. 2004b Giant hydrothermal hematite deposits with Mg-Fe metasomatism: A comparison of the Carajas, Hamersley, and other iron ores, *Economic Geology*, vol. 99, no. 1793-1800.
- DANIELSON A., MOLLER P. & DULSKI P. 1992 The europium anomalies in banded iron formations and the thermal history of the oceanic crust, *Chemical Geology*, vol. 97, pp. 89-100.
- DI TOMMASO I. & RUBINSTEIN N. 2007 Hydrothermal alteration mapping using ASTER data in the Infiernillo porphyry deposit, Argentina, *Ore Geology Reviews*, vol. 32, no. 1-2, pp. 275-290.
- DORR J. V., II, 1965 Nature and origin of the high-grade hematite ores of Minas Gerais, Brazil, *Economic Geology*, vol. 60, pp. 1-46.
- DUURING P. AND HAGEMANN, S. 2013 Controls for iron mineralisation hosted by Banded Iron Formation in the Mount Richardson district, Yilgarn Craton, Western Australia, Unpublished University of Western Australia report to Cliffs Natural Resources, 28p.
- DUURING P. & HAGEMANN S. G. 2010 High-grade iron mineralisation at the Beebyn deposit, Weld Range, Western Australia. In TYLER I. M. & KNOX-ROBINSON C. M. eds. 5th International Archean Symposium: Abstracts. pp. 291-293. Perth, Western Australia: Geological Survey of Western Australia.
- DUURING P. & HAGEMANN S. G. 2011 Contrasting styles of high-grade iron mineralisation at Weld Range, Western Australia. Iron Ore 2011 Proceedings, Perth: The Australasian Institute of Mining and Metallurgy, pp. 87-92.
- DUURING P. & HAGEMANN S. G. 2013a Genesis of superimposed hypogene and supergene Fe orebodies in BIF at the Madoonga deposit, Yilgarn Craton, Western Australia, *Mineralium Deposita*, vol. 48, pp. 371-395
- DUURING P. & HAGEMANN S. G. 2013b Leaching of silica bands and concentration of magnetite in Archean BIF by hypogene fluids: Beebyn Fe ore deposit, Yilgarn Craton, Western Australia, *Mineralium Deposita*, vol. 48, pp. 341-370.
- DUURING P., HAGEMANN S., NOVIKOVA Y., CUDAHY T. AND LAUKAMP C. 2012 Targeting iron ore in Banded Iron Formation using ASTER data: Weld Range greenstone belt, Yilgarn Craton, Western Australia, *Economic Geology*, vol. 107, no. 4, pp. 585-597.
- DYMEK R. F. & KLEIN C. 1988 Chemistry, petrology and origin by banded iron-formation lithologies from the 3800 Ma Isua supracrustal belt, West Greenland, *Precambrian Research*, vol. 39, pp. 247-302.
- FIGUEIREDO E SILVA R. C., *et al.* 2008 A Hydrothermal origin for the jasperlite-hosted, giant Serra Norte iron ore deposits in the Carajas Mineral Province, Para State, Brazil. In HAGEMANN S. G., *et al.* eds. Banded Iron Formation-Related High-Grade Iron Ore. pp. 255-290. Reviews in Economic Geology, vol. 15.
- FU B., *et al.* 2007 Mapping hydrocarbon-induced mineralogical alteration in the northern Tian Shan using ASTER multispectral data, *Terra Nova*, vol. 19, no. 4, pp. 225-231.
- GABR S., GHULAM A. & KUSKY T. 2010 Detecting areas of high-potential gold mineralization using ASTER data, *Ore Geology Reviews*, vol. 38, no. 1-2, pp. 59-69.
- GALLAGHER R. 2013 Hashimoto high-grade martite-goethite (M-G), martite-microplatey hematite (M-(mplH)) iron ore deposit- towards understanding ore genesis and associated alteration zoning, *Research project report*.

- GOLE M. J. 1981 Archean Banded Iron-Formations, Yilgarn Block, Western Australia, *Economic Geology*, vol. 76, pp. 1954-1974.
- GRANT S. L. 1997 Geochemical, radiogenic tracer isotopic, and U-Pb geochronological studies of Yukon Tanana Terrane rocks from the Money Klippe, southeastern Yukon, Canada. Edmonton: University of Alberta.
- GRESENS R. L. 1967 Composition-volume relationships of metasomatism, *Chemical Geology*, vol. 2, pp. 47-65.
- GRIFKINS C., HERRMANN W. & LARGE R. R. 2005 Altered volcanic rocks: a guide to description and interpretation: Hobart, Tasmania, Australia, *Centre for Ore Deposit Research*, p. 275.
- GROSS G. A. 1995 Algoma-type iron formation. In ECKSTRAND O. R., SINCLAIR W. D. & THORPE R. I. eds. *Geology of Canadian Mineral Deposit Types*. pp. 66-73. Geological Society of Canada, *Geology of Canada*.
- GUTZMER J., BENNY, C. CHISONGA, NICOLAS J. BEUKES 2008 The Geochemistry of Banded Iron Formation-Hosted High-Grade Hematite-Martite Iron Ores, *Society of Economic Geologists, Reviews in Economic Geology*, vol. 15, pp. 157-183.
- GUTZMER J., NETSHIOZWI S. & BEUKES N. J. 2002 Hydrothermal origin of high-grade iron orebodies hosted by the Paleoproterozoic Penge Iron Formation, Thambazimbi, South Africa, 16th International Sedimentological Congress. Auckland Park, South Africa.
- HAEST M., CUDAHY, T., LAUKAMP, C. and GREGORY, S. 2012a Quantitative mineralogy from infrared spectroscopic data: (I) Validation of mineral abundance and composition scripts at the Rocklea channel iron deposit in Western Australia, *Economic Geology*, vol. 107, pp. 209-228.
- HAEST M., CUDAHY, T., LAUKAMP, C. and GREGORY, S. 2012b Quantitative mineralogy from infrared spectroscopic data: (II) Three-dimensional mineralogical characterization of the Rocklea channel iron deposit, Western Australia, *Economic Geology*, vol. 107, pp. 229-249.
- HAEST M., LAUKAMP, C., CUDAHY, T., GESSNER, K. AND GREGORY, S. 2010 Hyperspectral insights in the 3D mineralogy of a channel iron ore deposit: implications to exploration, mining and ore genesis. In: *Earth Systems: change, sustainability, vulnerability*. Australian Earth Science Convention (AESC) 2010, Geological Society of Australia Abstracts No 98, pp. 155-156.
- HEWSON R. D., *et al.* 2006 Mapping geology associated with manganese mineralisation using spectral sensing techniques at Woodie Woodie, East Pilbara, *Exploration Geophysics*, vol. 37, no. 4, pp. 389-400.
- HUNT G. R. 1977 Spectral Signatures Of Particulate Minerals In The Visible And Near Infrared, *Geophysics*, vol. 42, pp. 502-513.
- JAMES H. L. & TRENDALL A. F. 1982 Banded iron formation: distribution in time and paleoenvironmental significance. In HOLLAND H. D. & SCHIDLOWSKI M. eds. *Mineral Deposits and the Evolution of the Biosphere*. pp. 199-218. New York: Springer-Verlag.
- JENSEN L. S. 1976 A new cation plot for classifying subalkalic volcanic rocks, *Ontario Geological Survey Miscellaneous Paper*, vol. 66, p. 22.
- KAHLE A. B., *et al.* 1991 The advanced spaceborne thermal emission reflectance radiometer (ASTER). *International Journal of Imaging Systems Technology*, vol. 3, no. 2, pp. 144-156.
- KENWORTHY S. 2008 Mineralisation study at the Beebyn and Madoonga orebodies, Weld Range. pp. 66. Perth: SRK Consulting (Australasia) Pty Ltd.
- KERRICH R. 1989 Lithophile element systematics of gold vein deposits in Archean greenstone belts; implications for source processes. In KEAYS R. R., RAMSAY W. R. H. & GROVES D. I. eds. *The geology of gold deposits; the perspective in 1988*. pp. 508-519. Chur, Switzerland: Harwood Academic Publishers.
- KLEIN C. 2005 Some Precambrian banded iron-formations (BIFs) from around the world: Their age, geologic setting, mineralogy, metamorphism, geochemistry, and origin, *American Mineralogist*, vol. 90, pp. 1473-1499.
- LASCELLES D. 2007 A possible origin of pisolitic iron ore deposits from raindrops and sheetwash in a semi-arid environment, *Iron Ore Conference 2007 Proceedings*, Australasian Institute of Mining and Metallurgy, Publication Series 6/2007, pp. 113-121

- LASCELLES D. F. 2002 A new look at old rocks - an alternative model for the origin of in situ iron ore deposits derived from banded iron formation, *Australian Institute of Mining and Metallurgy Publication Series 7/2002*, pp. 107-126.
- LASCELLES D. F. 2006a The Mount Gibson banded iron formation-hosted magnetite deposit: Two distinct processes for the origin of high-grade iron ore, *Economic Geology*, vol. 101, no. 3, pp. 651-666.
- LASCELLES D. F. 2006b The Mount Gibson banded iron formation-hosted magnetite deposit; two distinct processes for the origin of high-grade iron ore, *Economic Geology and the Bulletin of the Society of Economic Geologists*, vol. 101, no. 3, pp. 651-666.
- LAUKAMP C. 2011a Short wave infrared functional groups of rock-forming minerals, CSIRO Report EP115222.
- LAUKAMP C. C., T.J., CLEVERLY, J. S., OLIVER N.H.S., AND HEWSON, R., 2011b Airborne hyperspectral imaging of hydrothermal alteration zones in granitoids of the Eastern fold belt, Mount Isa inlier, Australia, *Geochemistry: Exploration, Environmental Analysis*, vol. 11, no. 3-24.
- LESHER C. M., *et al.* 2001 Trace-element geochemistry and petrogenesis of barren and ore-associated komatiites. In BARNES S.-J., CROCKET J. H. & MARTIN R. F. eds. International Geological Correlation Program 427 field conference ; Ore-forming processes in dynamic magmatic systems. pp. 673-696. Rouyn-Noranda, PQ, Canada.
- LOBATO L. M., FIGUEIREDO E SILVA, R.C., HAGEMANN, S., THORNE, W AND ZUCCHETTI, M. 2008 Hypogene Alteration Associated with High-Grade Banded Iron Formation- Related Iron Ore, *Banded Iron Formation-Related High-Grade Iron Ore. Society of Economic Geologist, Reviews in Economic Geology*, vol. 15, pp. 107-128.
- MASKELL A. 2010 Multi-stage structural controls and hypogene alteration of high-grade Fe-mineralisation at Matthew Ridge prospect, Jack Hills greenstone belt, Yilgarn craton. Faculty of Natural and Agricultural Sciences. pp. 50. Perth, Australia: The University of Western Australia.
- MCDONOUGH W. F. & SUN S. S. 1995 The composition of the Earth, *Chemical Geology*, vol. 120, pp. 223-253.
- MHOPJENI K. 2012 Integrated remote sensing an geological mapping of Quaternary to Recent surficial sediments of central Namib Uranium district, *Dissertation*
- MOGHADERI A., MOORE F. & MOHAMMADZADEH A. 2007 The application of advanced space-borne thermal emission and reflection (ASTER) radiometer data in the detection of alteration in the Chadormalu paleocrater, Bafq region, Central Iran, *Journal of Asian Earth Sciences*, vol. 30, no. 2, pp. 238-252.
- MORRIS R. C. 1980 A textural and mineralogical study of the relationship of iron ore to banded iron-formation in the Hamersley iron province of Western Australia, *Economic Geology*, vol. 75, pp. 184-279.
- MORRIS R. C. 1985 Genesis of iron ore in banded iron-formation by supergene and supergene-metamorphic processes - a conceptual model. In WOLFF K. H. ed. Handbook of strata-bound and stratiform ore deposits. pp. 73-75. Amsterdam: Elsevier.
- MORRIS R. C., AND RAMANAIDOU, E.R., 2007 Genesis of channel iron deposits (CID) of the Pilbara Region, Western Australia, *Australian Journal of Earth Sciences*, vol. 54, pp. 733-756.
- MORRIS R. V., *et al.* 1985 spectral and other physiochemical properties of submicron powders of hematite (Fe₂O₃), maghemite (Fe₂O₃), magnetite(Fe₃O₄), goethite (FeOOH), *journal of geophysical research*, vol. 90, pp. 3126-3144.
- MUKHOPADHYAY J., *et al.* 2008 Geology and genesis of the major banded iron formation-hosted high-grade iron ore deposits of India. In HAGEMANN S. G., *et al.* eds. Banded Iron Formation-Related High-Grade Iron Ore. pp. 291-316. Reviews in Economic Geology, vol. 15.
- RAMANAIDOU C. 1997 Measurement of the hematite:goethite ratio using field visible and near-infrared reflectance spectrometry in channel iron deposits, Western Australia, *Australian Journal of Earth Sciences*, vol. 44, pp. 411-420.

- RENNER R., *et al.* 1994 Komatiite flows from the Reliance Formation, Belingwe Belt, Zimbabwe; I, Petrography and mineralogy, *Journal of Petrology*, vol. 35, no. 2, pp. 361-400.
- ROWAN L. C., SCHMIDT R. G. & MARS J. C. 2006 Distribution of hydrothermally altered rocks in the Reko Diq, Pakistan mineralized area based on spectral analysis of ASTER data, *Remote Sensing of Environment*, vol. 104, pp. 74-87.
- SHERMAN D. M. & BURNS R. G. 1982 spectral characteristics of the iron oxides with application to the Martian Bright region mineralogy, *Journal of geophysical research*, vol. 87, pp. 169-180.
- SINGER R. B. & ROUSH T. L. 1985 Effects of temperature on remotely sensed mineral absorption features, *Journal of geophysical research*, vol. 90, pp. 434-444.
- SONNTAG I., LAUKAMP C. & HAGEMANN S. 2012 Low potassium hydrothermal alteration in low sulfidation epithermal systems detected by IRS and XRD: an example from the Co-O Mine, Eastern Mindanao, Philippines, *Ore Geology Reviews*, vol. 45, pp. 47-60.
- TAYLOR D., *et al.* 2001a Genesis of high-grade hematite orebodies of the Hamersley Province, Western Australia, *Economic Geology*, vol. 96, pp. 837-873.
- TAYLOR D., *et al.* 2001b Genesis of high-grade hematite orebodies of the Hamersley province. Western Australia, *Economic Geology*, vol. 96, pp. 837-873.
- THORNE W., *et al.* 2009 Oxygen Isotope Compositions of Iron Oxides from High-Grade BIF-Hosted Iron Ore Deposits of the Central Hamersley Province Western Australia: Constraints on the Evolution of Hydrothermal Fluids, *Economic Geology*, vol. 104, no. 7, pp. 1019-1035.
- WINCHESTER J. A. & FLOYD P. A. 1977 Geochemical discrimination of different magma series and their differentiation products using immobile elements, *Chemical Geology*, vol. 20, no. 4, pp. 325-343.
- WYBORN L. A. I., HEINRICH C. A. & JAKES A. L. 1994 Australian Proterozoic Mineral Systems – Essential Ingredients and Mappable Criteria, *1994 AusIMM Annual Conference: Australian Mining Looks North - the Challenges and Choices*, vol. 94, no. 5, pp. 109-115.

APPENDIX 2: GEOCHEMICAL ANALYSIS RESULTS

Sample No.	LCMR09	LCMR10	LCMR13			
Prospect	Mount Richardson	Mount Richardson	Mount Richardson			
Drill hole	PKD11001	PKD11001	PKD11001			
Depth (m)	48.500	55.500	69.600			
Rock type	BIF	BIF	BIF			
Alteration	least altered	least altered	least altered			
Analyte Symbol				Unit Symbol	Detection Limit	Analysis Method
SiO2	43.47	49.68	49.07	%	0.01	FUS-ICP
TiO2	0.004	0.003	0.007	%	0.001	FUS-ICP
Al2O3	0.48	0.39	0.46	%	0.01	FUS-ICP
Fe2O3(T)	54.03	48.66	49.36	%	0.01	FUS-ICP
MnO	0.047	0.022	0.039	%	0.001	FUS-ICP
MgO	0.04	0.03	0.05	%	0.01	FUS-ICP
CaO	0.08	0.06	0.09	%	0.01	FUS-ICP
Na2O	0.01	0.01	0.02	%	0.01	FUS-ICP
K2O	0.005	0.005	0.005	%	0.01	FUS-ICP
P2O5	0.28	0.13	0.11	%	0.01	FUS-ICP
FeO	11	1.3	1.4	%	0.1	TITR
Fe2O3	52.8	47.22	47.6	%	0.01	FUS-ICP
LOI	1.91	1.52	1.48	%		FUS-ICP
LOI2	1.79	1.37	132	%		FUS-ICP
Total	100.4	1:>0.5	1:>0.7	%	0.01	FUS-ICP
Total 2	100.2	100.4	100.5	%	0.01	FUS-ICP
C-Total	0.02	0.005	0.005	%	0.01	IR
Total S	0.02	0.02	0.02	%	0.01	IR
Tl	0.025	0.025	0.025	ppm	0.05	TD-MS
Ag	0.06	0.07	0.025	ppm	0.05	TD-MS
Al	0.05	0.03	0.06	%	0.01	TD-MS
As	9.5	3.1	10.1	ppm	0.1	TD-MS
Ba	3	2	5	ppm	1	TD-MS
Be	0.7	0.3	0.7	ppm	0.1	TD-MS
Bi	0.03	0.04	0.02	ppm	0.02	TD-MS
Ca	0.01	0.01	0.03	%	0.01	TD-MS
Cd	0.05	0.05	0.05	ppm	0.1	TD-MS
Co	13.1	5.8	21	ppm	0.1	TD-MS
Co				%	0.002	FUS-Na2O2
Cr	20.7	20.8	24.1	ppm	0.5	TD-MS
Cs	0.025	0.025	0.025	ppm	0.05	TD-MS
Cu	242	19.1	15.7	ppm	0.2	TD-MS
Fe	362	32.2	31.2	%	0.01	TD-MS
Ga	0.6	0.4	0.5	ppm	0.1	TD-MS
Ge	4.3	3.9	4	ppm	0.5	FUS-MS
Hf	0.05	0.05	0.05	ppm	0.1	FUS-MS
K	0.005	0.005	0.005	%	0.01	TD-MS
Li	17	11	0.7	ppm	0.5	TD-MS
In	0.05	0.05	0.05	ppm	0.1	TD-MS
Mg	0.01	0.005	0.02	%	0.01	TD-MS
Mn	358	240	267	ppm	1	TD-MS
Mo	0.5	0.9	0.6	ppm	0.1	TD-MS
Na	0.005	0.005	0.01	%	0.01	TD-MS
Ni	12.5	5.8	39.2	ppm	0.5	TD-MS
Nb	0.1	0.1	0.1	ppm	0.2	FUS-MS
Pb	15	11	2.3	ppm	0.5	TD-MS
Rb	0.1	0.1	0.1	ppm	0.2	TD-MS
Re	0.01	0.003	0.003	ppm	0.001	TD-MS
Sb	1.5	0.9	17	ppm	0.2	FUS-MS
Se	0.3	0.5	0.9	ppm	0.1	TD-MS
Sn	0.05	0.05	0.05	ppm	1	TD-MS
Sr	0.8	1.4	11	ppm	0.2	TD-MS
Ta	0.005	0.005	0.005	ppm	0.01	FUS-MS
Te	0.05	0.05	0.05	ppm	0.1	TD-MS
Th	0.13	0.09	0.07	ppm	0.05	FUS-MS
U	0.07	0.04	0.05	ppm	0.01	FUS-MS
V	4	3	6	ppm	1	TD-MS
W	0.7	1	0.6	ppm	0.1	TD-MS
Zn	18.8	12.5	16.9	ppm	0.2	TD-MS
Zr	1	1	1	ppm	1	FUS-MS
Sc	2	1	2	ppm	1	FUS-ICP
Y	5.7	4.5	7.5	ppm	0.5	FUS-MS
La	2.52	3.04	2.11	ppm	0.05	FUS-MS
Ce	4.42	4.19	2.95	ppm	0.05	FUS-MS
Pr	0.52	0.69	0.47	ppm	0.01	FUS-MS
Nd	2.33	2.76	222	ppm	0.05	FUS-MS
Sm	0.51	0.49	0.51	ppm	0.01	FUS-MS
Eu	0.36	0.299	0.347	ppm	0.005	FUS-MS
Gd	0.66	0.49	0.71	ppm	0.01	FUS-MS
Tb	0.11	0.09	0.13	ppm	0.01	FUS-MS
Dy	0.7	0.55	0.84	ppm	0.01	FUS-MS
Ho	0.16	12	0.19	ppm	0.01	FUS-MS
Er	0.49	0.37	0.61	ppm	0.01	FUS-MS
Tm	0.074	0.056	0.1	ppm	0.005	FUS-MS
Yb	0.5	0.38	0.7	ppm	0.01	FUS-MS
Lu	0.082	0.062	0.124	ppm	0.002	FUS-MS

Sample No.	LCMR02	LCMR03	LCMR16			
Prospect	Mount Richardson	Mount Richardson	Mount Richardson			
Drill hole	PKD11001	PKD11001	PKD11001			
Depth (m)	26	32.5	75			
Rock type	BIF	BIF	BIF			
Alteration	supergene	supergene	supergene			
Analyte Symbol				Unit Symbol	Detection Limit	Analysis Method
SiO2	2.12	3.72	2.06	%	0.01	FUS-ICP
TiO2	0.01	0.006	0.004	%	0.001	FUS-ICP
Al2O3	1.8	0.75	1.56	%	0.01	FUS-ICP
Fe2O3(T)	91.44	84.5	84.61	%	0.01	FUS-ICP
MnO	0.035	0.046	3.502	%	0.001	FUS-ICP
MgO	0.03	0.005	0.05	%	0.01	FUS-ICP
CaO	0.08	0.05	0.1	%	0.01	FUS-ICP
Na2O	0.03	0.1	0.04	%	0.01	FUS-ICP
K2O	0.02	0.005	0.08	%	0.01	FUS-ICP
P2O5	0.32	0.16	0.26	%	0.01	FUS-ICP
FeO	0.1	0.2	<0.1	%	0.1	TITR
Fe2O3	91.33	84.27	94.5	%	0.01	FUS-ICP
LOI	4.94	8.75	5.87	%		FUS-ICP
LOI2	4.93	8.73	5.86	%		FUS-ICP
Total	100.8	98.09	98.11	%	0.01	FUS-ICP
Total 2	100.8	98.07	98.1	%	0.01	FUS-ICP
C-Total	0.08	0.07	0.01	%	0.01	IR
Total S	0.04	0.02	0.02	%	0.01	IR
Tl	0.025	0.025	2.7	ppm	0.05	TD-MS
Ag	0.43	0.22	0.14	ppm	0.05	TD-MS
Al	0.62	0.33	0.5	%	0.01	TD-MS
As	19.9	9.7	212	ppm	0.1	TD-MS
Ba	6	9	4760	ppm	1	TD-MS
Be	1.3	0.8	3.7	ppm	0.1	TD-MS
Bi	0.02	0.05	0.09	ppm	0.02	TD-MS
Ca	0.01	0.02	0.04	%	0.01	TD-MS
Cd	0.05	0.05	0.4	ppm	0.1	TD-MS
Co	4.5	7.8	1710	ppm	0.1	TD-MS
Co			0.173	%	0.002	FUS-Na2O2
Cr	100	14.7	7.3	ppm	0.5	TD-MS
Cs	0.025	0.025	0.06	ppm	0.05	TD-MS
Cu	102	23.6	163	ppm	0.2	TD-MS
Fe	60.9	56.8	56.9	%	0.01	TD-MS
Ga	0.6	0.3	0.05	ppm	0.1	TD-MS
Ge	5.4	5.5	4.6	ppm	0.5	FUS-MS
Hf	0.05	0.05	0.05	ppm	0.1	FUS-MS
K	0.01	0.005	0.03	%	0.01	TD-MS
Li	2.6	0.8	24.4	ppm	0.5	TD-MS
In	0.05	0.05	0.05	ppm	0.1	TD-MS
Mg	0.01	0.01	0.03	%	0.01	TD-MS
Mn	218	303	26600	ppm	1	TD-MS
Mo	0.5	0.5	3.8	ppm	0.1	TD-MS
Na	0.02	0.02	0.02	%	0.01	TD-MS
Ni	14.4	11.7	1090	ppm	0.5	TD-MS
Nb	0.2	0.2	0.1	ppm	0.2	FUS-MS
Pb	1.7	1.7	3.8	ppm	0.5	TD-MS
Rb	0.5	0.2	1.2	ppm	0.2	TD-MS
Re	0.005	0.005	0.005	ppm	0.001	TD-MS
Sb	2.8	1.5	2.3	ppm	0.2	FUS-MS
Se	0.9	0.8	1.9	ppm	0.1	TD-MS
Sn	0.05	0.05	0.05	ppm	1	TD-MS
Sr	6.2	1.6	36.4	ppm	0.2	TD-MS
Ta	0.02	0.03	0.005	ppm	0.01	FUS-MS
Te	0.05	0.05	0.05	ppm	0.1	TD-MS
Th	0.15	0.06	0.12	ppm	0.05	FUS-MS
U	0.24	0.18	0.64	ppm	0.01	FUS-MS
V	13	7	50	ppm	1	TD-MS
W	3.4	0.9	0.3	ppm	0.1	TD-MS
Zn	16.6	11.1	241	ppm	0.2	TD-MS
Zr	2	2	1	ppm	1	FUS-MS
Sc	25	13	11	ppm	1	FUS-ICP
Y	10.2	10	41.3	ppm	0.5	FUS-MS
La	7.92	4.65	11.7	ppm	0.05	FUS-MS
Ce	13	22.4	48.2	ppm	0.05	FUS-MS
Pr	1.13	0.81	5.81	ppm	0.01	FUS-MS
Nd	3.6	3.31	31.4	ppm	0.05	FUS-MS
Sm	0.78	0.82	9.82	ppm	0.01	FUS-MS
Eu	0.432	0.587	4.75	ppm	0.005	FUS-MS
Gd	0.98	1.12	10.1	ppm	0.01	FUS-MS
Tb	0.17	0.19	1.62	ppm	0.01	FUS-MS
Dy	1.23	1.26	9.43	ppm	0.01	FUS-MS
Ho	0.29	0.27	1.85	ppm	0.01	FUS-MS
Er	0.95	0.8	5.44	ppm	0.01	FUS-MS
Tm	0.148	0.12	0.828	ppm	0.005	FUS-MS
Yb	0.98	0.78	5.84	ppm	0.01	FUS-MS
Lu	0.157	0.125	1.04	ppm	0.002	FUS-MS

Sample No.	LCMR05	LCMR07	LCMR08			
Prospect	Mount Richardson	Mount Richardson	Mount Richardson			
Drill hole	PKD11001	PKD11001	PKD11001			
Depth (m)	38	46	46.5			
Rock type	BIF	BIF	BIF			
Alteration	hypogene	hypogene	hypogene			
Analyte Symbol				Unit Symbol	Detection Limit	Analysis Method
SiO2	9.23	28.29	31.49	%	0.01	FUS-ICP
TiO2	0.003	0.002	0.003	%	0.001	FUS-ICP
Al2O3	2.23	2.52	0.88	%	0.01	FUS-ICP
Fe2O3(T)	86.42	63.26	66.93	%	0.01	FUS-ICP
MnO	0.213	1.296	0.023	%	0.001	FUS-ICP
MgO	0.03	0.005	0.02	%	0.01	FUS-ICP
CaO	0.06	0.04	0.08	%	0.01	FUS-ICP
Na2O	0.02	0.07	0.01	%	0.01	FUS-ICP
K2O	0.005	0.005	0.005	%	0.01	FUS-ICP
P2O5	0.15	0.15	0.16	%	0.01	FUS-ICP
FeO	<0.1	<0.1	0.7	%	0.1	TITR
Fe2O3	86.31	63.15	66.01	%	0.01	FUS-ICP
LOI	2.01	2.89	1.36	%		FUS-ICP
LOI2	1.99	2.87	1.28	%		FUS-ICP
Total	100.4	98.52	101	%	0.01	FUS-ICP
Total 2	100.3	98.51	100.7	%	0.01	FUS-ICP
C-Total	0.005	0.005	0.005	%	0.01	IR
Total S	0.03	0.02	0.02	%	0.01	IR
TI	0.025	0.025	0.025	ppm	0.05	TD-MS
Ag	0.4	0.13	0.09	ppm	0.05	TD-MS
Al	0.79	1.19	0.2	%	0.01	TD-MS
As	10.1	6.3	8.8	ppm	0.1	TD-MS
Ba	25	12	7	ppm	1	TD-MS
Be	0.6	0.7	0.6	ppm	0.1	TD-MS
Bi	0.01	0.01	0.01	ppm	0.02	TD-MS
Ca	0.005	0.01	0.01	%	0.01	TD-MS
Cd	0.05	0.05	0.05	ppm	0.1	TD-MS
Co	62	899	4.7	ppm	0.1	TD-MS
Co				%	0.002	FUS-Na2O2
Cr	6.5	6.4	6.8	ppm	0.5	TD-MS
Cs	0.025	0.05	0.07	ppm	0.05	TD-MS
Cu	51.7	65.5	10.6	ppm	0.2	TD-MS
Fe	54.3	43	43.1	%	0.01	TD-MS
Ga	0.2	0.3	0.3	ppm	0.1	TD-MS
Ge	6.4	4.6	4.2	ppm	0.5	FUS-MS
Hf	0.05	0.05	0.05	ppm	0.1	FUS-MS
K	0.005	0.005	0.005	%	0.01	TD-MS
Li	15	122	1.4	ppm	0.5	TD-MS
In	0.05	0.05	0.05	ppm	0.1	TD-MS
Mg	0.01	0.01	0.005	%	0.01	TD-MS
Mn	1380	9840	127	ppm	1	TD-MS
Mo	0.5	0.6	0.3	ppm	0.1	TD-MS
Na	0.01	0.005	0.005	%	0.01	TD-MS
Ni	51.4	364	7	ppm	0.5	TD-MS
Nb	0.1	0.1	0.1	ppm	0.2	FUS-MS
Pb	1.2	0.7	0.25	ppm	0.5	TD-MS
Rb	0.1	0.1	0.2	ppm	0.2	TD-MS
Re	0.009	0.007	0.007	ppm	0.001	TD-MS
Sb	1.6	0.6	0.9	ppm	0.2	FUS-MS
Se	0.4	0.6	0.6	ppm	0.1	TD-MS
Sn	0.05	0.05	0.05	ppm	1	TD-MS
Sr	8.8	7.1	4	ppm	0.2	TD-MS
Ta	0.43	0.1	0.005	ppm	0.01	FUS-MS
Te	0.05	0.05	0.05	ppm	0.1	TD-MS
Th	0.1	0.05	0.1	ppm	0.05	FUS-MS
U	0.07	0.04	0.04	ppm	0.01	FUS-MS
V	10	7	5	ppm	1	TD-MS
W	4.8	0.8	0.9	ppm	0.1	TD-MS
Zn	12.3	54.4	8.2	ppm	0.2	TD-MS
Zr	0.05	0.05	2	ppm	1	FUS-MS
Sc	7	3	2	ppm	1	FUS-ICP
Y	11.4	9.5	7.4	ppm	0.5	FUS-MS
La	42	23.1	10.6	ppm	0.05	FUS-MS
Ce	51.5	66.8	17	ppm	0.05	FUS-MS
Pr	7.05	4.15	2.02	ppm	0.01	FUS-MS
Nd	23	14.4	8.11	ppm	0.05	FUS-MS
Sm	3.4	2.37	1.61	ppm	0.01	FUS-MS
Eu	1.21	1.01	0.749	ppm	0.005	FUS-MS
Gd	1.76	1.9	1.31	ppm	0.01	FUS-MS
Tb	0.27	0.23	0.19	ppm	0.01	FUS-MS
Dy	1.65	1.37	1.09	ppm	0.01	FUS-MS
Ho	0.34	0.29	23	ppm	0.01	FUS-MS
Er	1	0.87	0.68	ppm	0.01	FUS-MS
Tm	0.153	0.133	0.103	ppm	0.005	FUS-MS
Yb	1.02	0.88	0.67	ppm	0.01	FUS-MS
Lu	0.163	0.14	0.109	ppm	0.002	FUS-MS

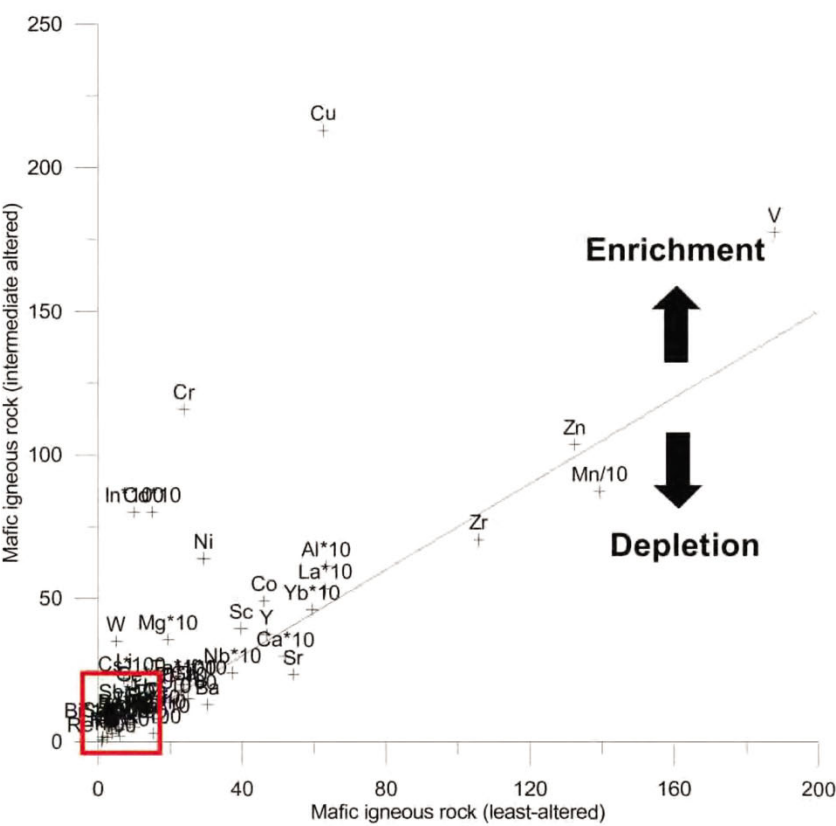
Sample No.	LCMR22	LCMR23			
Prospect	Mount Richardson	Mount Richardson			
Drill hole	PKD11001	PKD11001			
Depth (m)	134	153			
Rock type	gabbro	gabbro			
Alteration	least altered	least altered			
Analyte Symbol	distal	distal	Unit Symbol	Detection Limit	Analysis Method
SiO2	56.19	54.34	%	0.01	FUS-ICP
TiO2	1.51	1.394	%	0.001	FUS-ICP
Al2O3	11.85	11.78	%	0.01	FUS-ICP
Fe2O3(T)	17.38	16.88	%	0.01	FUS-ICP
MnO	0.194	0.211	%	0.001	FUS-ICP
MgO	3.31	3.19	%	0.01	FUS-ICP
CaO	6.14	9.97	%	0.01	FUS-ICP
Na2O	2.38	1.56	%	0.01	FUS-ICP
K2O	0.17	0.19	%	0.01	FUS-ICP
P2O5	0.22	0.21	%	0.01	FUS-ICP
FeO	11.4	10.1	%	0.1	TITR
Fe2O3	4.7	5.65	%	0.01	FUS-ICP
LOI	1.44	1.23	%		FUS-ICP
LOI2	0.16	0.1	%		FUS-ICP
Total	100.8	100.9	%	0.01	FUS-ICP
Total 2	99.51	99.82	%	0.01	FUS-ICP
C-Total	0.005	0.03	%	0.01	IR
Total S	0.08	0.15	%	0.01	IR
Tl	0.025	0.025	ppm	0.05	TD-MS
Ag	0.025	0.025	ppm	0.05	TD-MS
Al	6.68	6.15	%	0.01	TD-MS
As	2.4	5.4	ppm	0.1	TD-MS
Ba	36	21	ppm	1	TD-MS
Be	0.8	0.7	ppm	0.1	TD-MS
Bi	0.02	0.03	ppm	0.02	TD-MS
Ca	4.56	6.85	%	0.01	TD-MS
Cd	0.1	0.3	ppm	0.1	TD-MS
Co	45.9	44	ppm	0.1	TD-MS
Co			%	0.002	FUS-Na2O2
Cr	14.1	37.6	ppm	0.5	TD-MS
Cs	0.07	0.14	ppm	0.05	TD-MS
Cu	45.1	88.6	ppm	0.2	TD-MS
Fe	11	10.7	%	0.01	TD-MS
Ga	22.5	26.6	ppm	0.1	TD-MS
Ge	1	1.6	ppm	0.5	FUS-MS
Hf	3.1	2.6	ppm	0.1	FUS-MS
K	0.14	0.16	%	0.01	TD-MS
Li	8.6	4.7	ppm	0.5	TD-MS
In	0.1	0.1	ppm	0.1	TD-MS
Mg	1.92	1.75	%	0.01	TD-MS
Mn	1260	1410	ppm	1	TD-MS
Mo	0.2	0.7	ppm	0.1	TD-MS
Na	1.95	122	%	0.01	TD-MS
Ni	21.2	32.1	ppm	0.5	TD-MS
Nb	4.4	3.4	ppm	0.2	FUS-MS
Pb	1.7	3.9	ppm	0.5	TD-MS
Rb	1.1	1.2	ppm	0.2	TD-MS
Re	0.006	0.009	ppm	0.001	TD-MS
Sb	0.7	1.2	ppm	0.2	FUS-MS
Se	1.7	1.8	ppm	0.1	TD-MS
Sn	0.05	0.05	ppm	1	TD-MS
Sr	60.9	52.3	ppm	0.2	TD-MS
Ta	0.32	0.16	ppm	0.01	FUS-MS
Te	0.05	0.05	ppm	0.1	TD-MS
Th	1.26	1.05	ppm	0.05	FUS-MS
U	0.28	0.24	ppm	0.01	FUS-MS
V	154	184	ppm	1	TD-MS
W	0.05	0.05	ppm	0.1	TD-MS
Zn	145	155	ppm	0.2	TD-MS
Zr	119	99	ppm	1	FUS-MS
Sc	38	38	ppm	1	FUS-ICP
Y	50.9	44.3	ppm	0.5	FUS-MS
La	6.24	6.5	ppm	0.05	FUS-MS
Ce	16.3	15.8	ppm	0.05	FUS-MS
Pr	2.43	2.18	ppm	0.01	FUS-MS
Nd	12.3	11	ppm	0.05	FUS-MS
Sm	4.28	3.66	ppm	0.01	FUS-MS
Eu	1.63	1.46	ppm	0.005	FUS-MS
Gd	6.24	5.21	ppm	0.01	FUS-MS
Tb	1.26	1.03	ppm	0.01	FUS-MS
Dy	8.55	7.18	ppm	0.01	FUS-MS
Ho	1.9	1.62	ppm	0.01	FUS-MS
Er	6.06	5.12	ppm	0.01	FUS-MS
Tm	0.957	0.802	ppm	0.005	FUS-MS
Yb	6.49	5.49	ppm	0.01	FUS-MS
Lu	1.1	0.937	ppm	0.002	FUS-MS

Sample No.	LCMR19	LCMR20			
Prospect	Mount Richardson	Mount Richardson			
Drill hole	PKD11001	PKD11001			
Depth (m)	96.5	100.5			
Rock type	mafic Igneous rock	mafic igneous rock			
Alteration	hypogene	hypogene			
Analyte Symbol	Intermediate	intermediate	Unit Symbol	Detection Limit	Analysis Method
SiO2	53.85	47.34	%	0.01	FUS-ICP
TiO2	1.56	0.541	%	0.001	FUS-ICP
Al2O3	11.66	12.54	%	0.01	FUS-ICP
Fe2O3(T)	19.76	11.9	%	0.01	FUS-ICP
MnO	0.088	0.165	%	0.001	FUS-ICP
MgO	6.41	7.21	%	0.01	FUS-ICP
CaO	0.45	7.88	%	0.01	FUS-ICP
Na2O	0.07	1.83	%	0.01	FUS-ICP
K2O	0.02	0.05	%	0.01	FUS-ICP
P2O5	0.24	0.08	%	0.01	FUS-ICP
FeO	12.8	9.2	%	0.1	TITR
Fe2O3	5.53	1.67	%	0.01	FUS-ICP
LOI	5.96	10.86	%		FUS-ICP
LOI2	4.52	9.83	%		FUS-ICP
Total	100	100.4	%	0.01	FUS-ICP
Total 2	98.62	99.37	%	0.01	FUS-ICP
C-Total	0.02	1.61	%	0.01	IR
Total S	0.01	0.01	%	0.01	IR
Tl	0.025	0.025	ppm	0.05	TD-MS
Ag	0.025	0.025	ppm	0.05	TD-MS
Al	5.77	6.47	%	0.01	TD-MS
As	6.4	3.6	ppm	0.1	TD-MS
Ba	8	18	ppm	1	TD-MS
Be	1.1	0.5	ppm	0.1	TD-MS
Bi	0.06	0.04	ppm	0.02	TD-MS
Ca	0.3	5.64	%	0.01	TD-MS
Cd	0.05	0.1	ppm	0.1	TD-MS
Co	49.8	48.3	ppm	0.1	TD-MS
Co			%	0.002	FUS-Na2O2
Cr	28.6	203	ppm	0.5	TD-MS
Cs	0.31	0.11	ppm	0.05	TD-MS
Cu	294	132	ppm	0.2	TD-MS
Fe	12.7	8.08	%	0.01	TD-MS
Ga	21.7	14.4	ppm	0.1	TD-MS
Ge	2.2	1.3	ppm	0.5	FUS-MS
Hf	3	1	ppm	0.1	FUS-MS
K	0.02	0.04	%	0.01	TD-MS
Li	30.3	14	ppm	0.5	TD-MS
In	0.1	0.05	ppm	0.1	TD-MS
Mg	3.38	3.75	%	0.01	TD-MS
Mn	585	1160	ppm	1	TD-MS
Mo	0.1	0.3	ppm	0.1	TD-MS
Na	0.03	1.3	%	0.01	TD-MS
Ni	34	93.6	ppm	0.5	TD-MS
Nb	3.8	1	ppm	0.2	FUS-MS
Pb	1.6	1.5	ppm	0.5	TD-MS
Rb	2.2	1.3	ppm	0.2	TD-MS
Re	0.002	0.007	ppm	0.001	TD-MS
Sb	2.3	0.6	ppm	0.2	FUS-MS
Se	1.1	0.5	ppm	0.1	TD-MS
Sn	0.05	0.05	ppm	1	TD-MS
Sr	7.6	39.3	ppm	0.2	TD-MS
Ta	0.36	0.04	ppm	0.01	FUS-MS
Te	0.05	0.05	ppm	0.1	TD-MS
Th	1.07	0.36	ppm	0.05	FUS-MS
U	0.22	0.07	ppm	0.01	FUS-MS
V	169	186	ppm	1	TD-MS
W	0.6	0.1	ppm	0.1	TD-MS
Zn	129	78.2	ppm	0.2	TD-MS
Zr	106	35	ppm	1	FUS-MS
Sc	40	39	ppm	1	FUS-ICP
Y	53.5	21.3	ppm	0.5	FUS-MS
La	7.69	2.97	ppm	0.05	FUS-MS
Ce	18.2	5.8	ppm	0.05	FUS-MS
Pr	2.61	0.88	ppm	0.01	FUS-MS
Nd	13.2	4.5	ppm	0.05	FUS-MS
Sm	4.24	1.43	ppm	0.01	FUS-MS
Eu	1.37	0.585	ppm	0.005	FUS-MS
Gd	6.49	2.25	ppm	0.01	FUS-MS
Tb	1.33	0.46	ppm	0.01	FUS-MS
Dy	8.92	3.27	ppm	0.01	FUS-MS
Ho	1.99	0.74	ppm	0.01	FUS-MS
Er	6.3	2.38	ppm	0.01	FUS-MS
Tm	0.962	0.379	ppm	0.005	FUS-MS
Yb	6.65	2.56	ppm	0.01	FUS-MS
Lu	1.13	0.404	ppm	0.002	FUS-MS

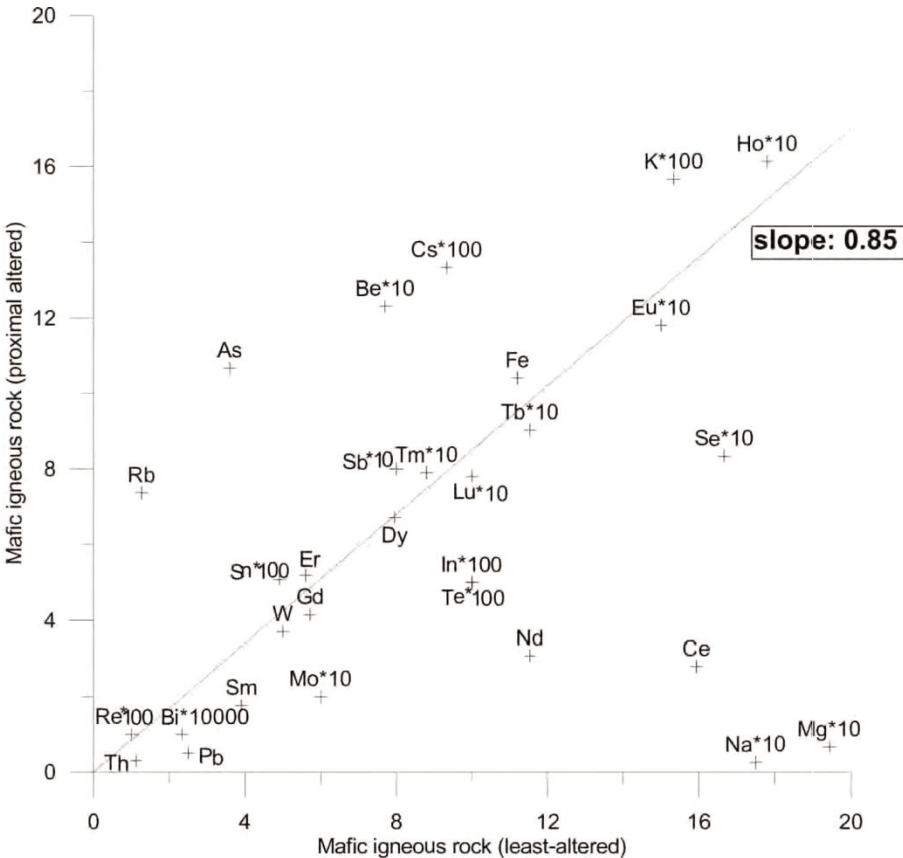
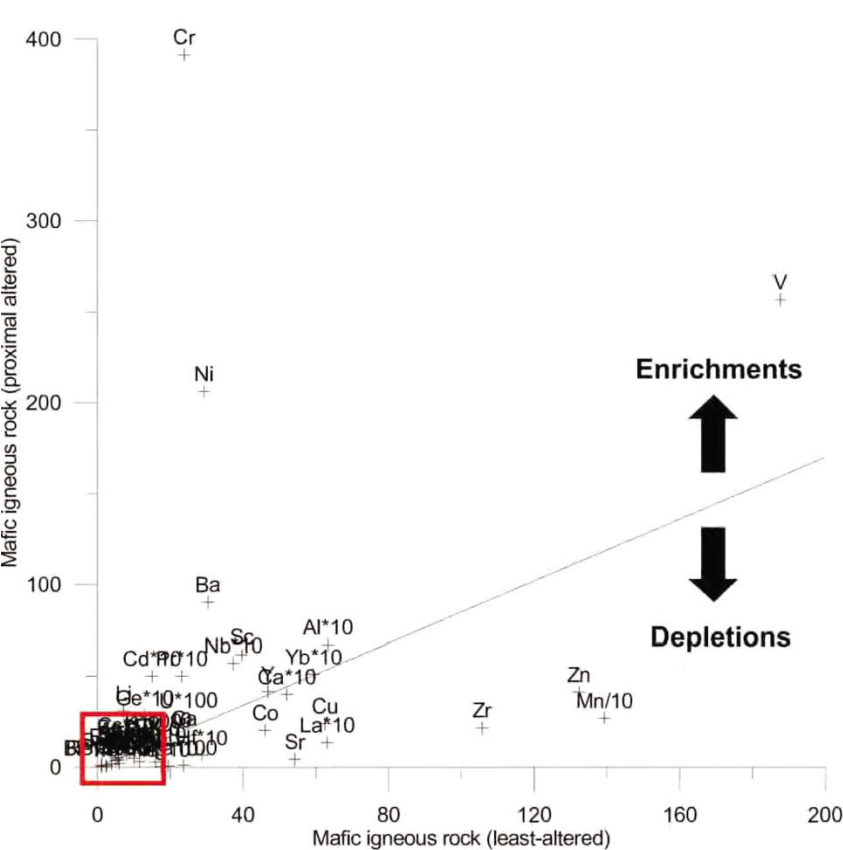
Sample No.	LCMR17	LCMR18	LCMR01			
Prospect	Mount Richardson	Mount Richardson	Mount Richardson			
Drill hole	PKD11001	PKD11001	PKD11001			
Depth (m)	86	90.5	24.1			
Rock type	mafic igneous rock	mafic igneous rock	mafic igneous rock			
Alteration	supergene	supergene	supergene			
Analyte Symbol	proximal	proximal	proximal	Unit Symbol	Detection Limit	Analysis Method
SiO2	61.6	61.24	37.85	%	0.01	FUS-ICP
TiO2	0.349	0.364	0.687	%	0.001	FUS-ICP
Al2O3	14.75	14.73	31.74	%	0.01	FUS-ICP
Fe2O3(T)	16.91	16.46	15.47	%	0.01	FUS-ICP
MnO	0.014	0.073	0.021	%	0.001	FUS-ICP
MgO	0.07	0.17	0.13	%	0.01	FUS-ICP
CaO	0.06	0.08	0.05	%	0.01	FUS-ICP
Na2O	0.03	0.04	0.04	%	0.01	FUS-ICP
K2O	0.01	0.11	0.43	%	0.01	FUS-ICP
P2O5	0.09	0.1	0.13	%	0.01	FUS-ICP
FeO	<0.1	<0.1	<0.1	%	0.1	TITR
Fe2O3	16.8	16.35	15.36	%	0.01	FUS-ICP
LOI	6.67	7.38	12.58	%		FUS-ICP
LOI2	6.66	7.37	12.56	%		FUS-ICP
Total	100.6	100.7	99.12	%	0.01	FUS-ICP
Total 2	100.5	100.7	99.11	%	0.01	FUS-ICP
C-Total	0.005	0.005	0.02	%	0.01	IR
Total S	0.02	0.02	0.02	%	0.01	IR
Tl	0.025	0.06	0.025	ppm	0.05	TD-MS
Ag	0.025	0.025	0.09	ppm	0.05	TD-MS
Al	6.58	6.83	>10.0	%	0.01	TD-MS
As	14.7	11.2	6.1	ppm	0.1	TD-MS
Ba	9	72	190	ppm	1	TD-MS
Be	1.4	0.8	15	ppm	0.1	TD-MS
Bi	0.01	0.01	0.01	ppm	0.02	TD-MS
Ca	0.04	0.05	0.04	%	0.01	TD-MS
Cd	0.05	0.05	0.05	ppm	0.1	TD-MS
Co	9.3	50	1.6	ppm	0.1	TD-MS
Co				%	0.002	FUS-Na2O2
Cr	286	375	513	ppm	0.5	TD-MS
Cs	0.06	0.12	0.22	ppm	0.05	TD-MS
Cu	24.8	20.8	26.1	ppm	0.2	TD-MS
Fe	10.7	10.8	9.72	%	0.01	TD-MS
Ga	12.9	13.3	25.1	ppm	0.1	TD-MS
Ge	3.4	2.4	2.7	ppm	0.5	FUS-MS
Hf	0.5	0.5	1	ppm	0.1	FUS-MS
K	0.01	0.08	0.38	%	0.01	TD-MS
Li	47.1	34.1	11.4	ppm	0.5	TD-MS
In	0.05	0.05	0.05	ppm	0.1	TD-MS
Mg	0.04	0.09	0.07	%	0.01	TD-MS
Mn	99	546	164	ppm	1	TD-MS
Mo	0.1	0.2	0.3	ppm	0.1	TD-MS
Na	0.02	0.03	0.03	%	0.01	TD-MS
Ni	145	84.7	389	ppm	0.5	TD-MS
Nb	0.3	0.2	1.2	ppm	0.2	FUS-MS
Pb	0.25	0.25	1	ppm	0.5	TD-MS
Rb	0.4	3.8	17.9	ppm	0.2	TD-MS
Re	0.013	0.01	0.003	ppm	0.001	TD-MS
Sb	0.4	0.9	1.1	ppm	0.2	FUS-MS
Se	0.6	0.5	1.4	ppm	0.1	TD-MS
Sn	0.05	0.05	0.05	ppm	1	TD-MS
Sr	4.4	5.5	3	ppm	0.2	TD-MS
Ta	0.005	0.005	0.02	ppm	0.01	FUS-MS
Te	0.05	0.05	0.05	ppm	0.1	TD-MS
Th	0.22	0.22	0.48	ppm	0.05	FUS-MS
U	0.13	0.33	0.36	ppm	0.01	FUS-MS
V	184	171	415	ppm	1	TD-MS
W	0.6	0.3	0.2	ppm	0.1	TD-MS
Zn	34	40.6	49.3	ppm	0.2	TD-MS
Zr	15	17	33	ppm	1	FUS-MS
Sc	43	44	98	ppm	1	FUS-ICP
Y	98.9	8.9	16.9	ppm	0.5	FUS-MS
La	1.06	1.47	1.55	ppm	0.05	FUS-MS
Ce	1.25	3.18	3.94	ppm	0.05	FUS-MS
Pr	0.53	0.47	0.51	ppm	0.01	FUS-MS
Nd	4.23	2.39	2.58	ppm	0.05	FUS-MS
Sm	3.63	0.82	0.84	ppm	0.01	FUS-MS
Eu	2.7	0.457	0.385	ppm	0.005	FUS-MS
Gd	9.76	1.1	1.57	ppm	0.01	FUS-MS
Tb	2.15	0.21	0.35	ppm	0.01	FUS-MS
Dy	16.1	1.47	2.58	ppm	0.01	FUS-MS
Ho	3.88	0.33	0.63	ppm	0.01	FUS-MS
Er	12.5	1.06	1.99	ppm	0.01	FUS-MS
Tm	1.89	0.171	0.316	ppm	0.005	FUS-MS
Yb	11.9	1.24	2.16	ppm	0.01	FUS-MS
Lu	12.72	0.24	0.382	ppm	0.002	FUS-MS

APPENDIX 3: GRANT PLOT

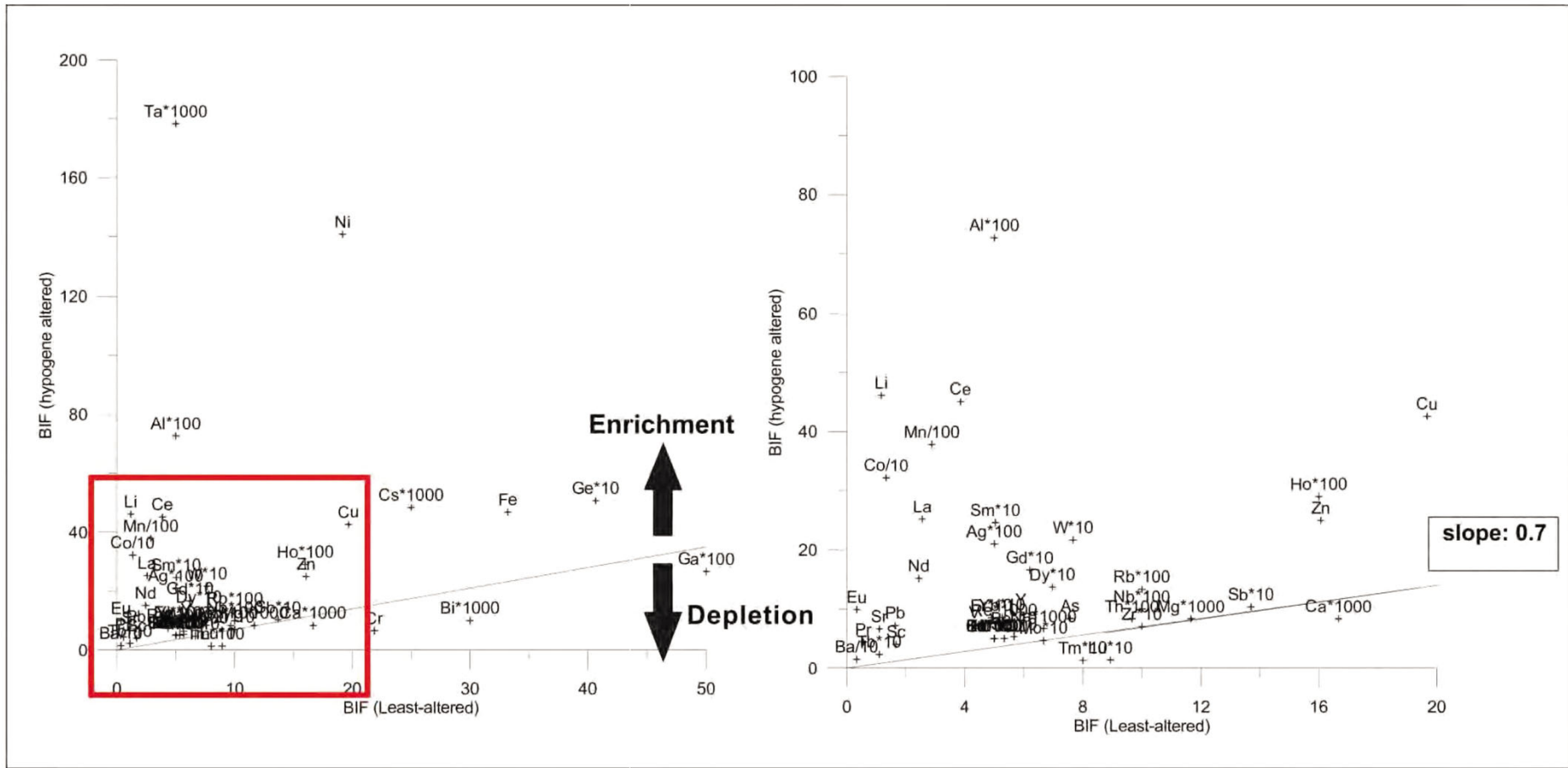
Grant plot: Intermediate alteration mafic igneous rocks



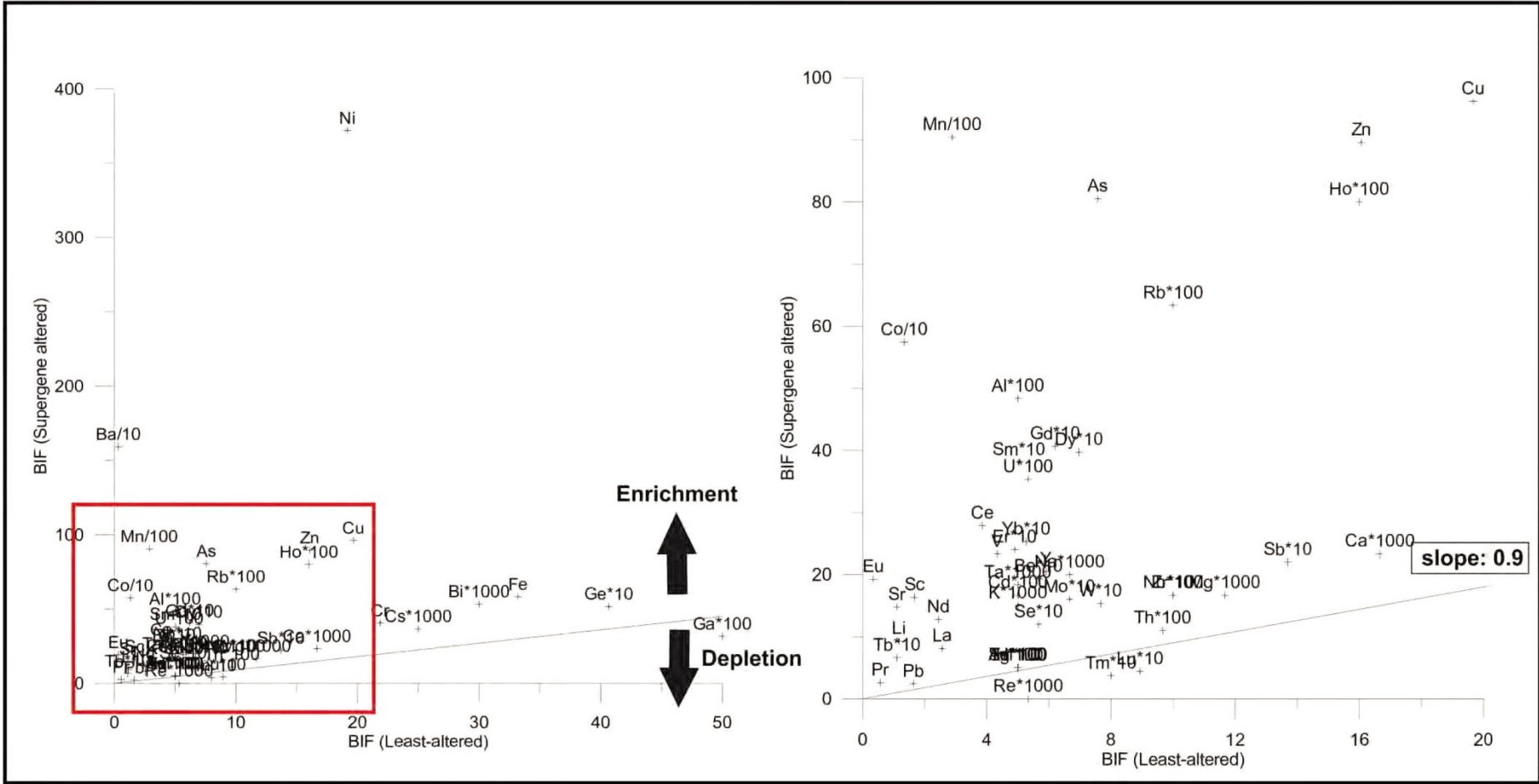
Grant plot: Proximal alteration mafic igneous rocks



Grant plot: Hypogene altered BIF rocks



Grant plot: Supergene altered BIF rocks



APPENDIX 4: MASS BALANCE ANALYSIS DATA

Sample No. Prospect	LCMR09 Mount Richardson	LCMR10 Mount Richardson	LCMR13 Mount Richardson	AVERAGE Mount Richardson	STAND_DEV Mount Richardson
Drill hole	PKD11001	PKD11001	PKD11001	PKD11001	PKD11001
Depth (m)	48.500	55.500	69.600		
Rock type	BIF	BIF	BIF		
Alteration	least altered	least altered	least altered	BIF	BIF
Analyte Symbol					
SiO2	43.470	49.680	49.070	47.407	3.423
TiO2	0.004	0.003	0.007	0.005	0.002
Al2O3	0.480	0.390	0.460	0.443	0.047
Fe2O3(T)	54.030	48.660	49.360	50.683	2.919
MnO	0.047	0.022	0.039	0.036	0.013
MgO	0.040	0.030	0.050	0.040	0.010
CaO	0.080	0.060	0.090	0.077	0.015
Na2O	0.010	0.010	0.020	0.013	0.006
K2O	0.005	0.005	0.005	0.005	0.000
P2O5	0.280	0.130	0.110	0.173	0.093
FeO	1.100	1.300	1.400	1.267	0.153
Fe2O3	52.800	47.220	47.800	49.273	3.068
Tl	0.025	0.025	0.025	0.025	0.000
Ag	0.060	0.070	0.025	0.052	0.024
Al	0.050	0.030	0.060	0.047	0.015
As	9.500	3.100	10.100	7.567	3.880
Ba	3.000	2.000	5.000	3.333	1.528
Be	0.700	0.300	0.700	0.567	0.231
Bi	0.030	0.040	0.020	0.030	0.010
Ca	0.010	0.010	0.030	0.017	0.012
Cd	0.050	0.050	0.050	0.050	0.000
Co	13.100	5.800	21.000	13.300	7.602
Co					
Cr	20.700	20.800	24.100	21.867	1.935
Cs	0.025	0.025	0.025	0.025	0.000
Cu	24.200	19.100	15.700	19.667	4.278
Fe	36.200	32.200	31.200	33.200	2.646
Ga	0.600	0.400	0.500	0.500	0.100
Ge	4.300	3.900	4.000	4.067	0.208
Hf	0.050	0.050	0.050	0.050	0.000
K	0.005	0.005	0.005	0.005	0.000
Li	1.700	1.100	0.700	1.167	0.503
In	0.050	0.050	0.050	0.050	0.000
Mg	0.010	0.005	0.020	0.012	0.008
Mn	358.000	240.000	267.000	288.333	61.825
Mo	0.500	0.900	0.600	0.667	0.208
Na	0.005	0.005	0.010	0.007	0.003
Ni	12.500	5.800	39.200	19.167	17.670
Nb	0.100	0.100	0.100	0.100	0.000
Pb	1.500	1.100	2.300	1.633	0.611
Rb	0.100	0.100	0.100	0.100	0.000
Re	0.010	0.003	0.003	0.005	0.004
Sb	1.500	0.900	1.700	1.367	0.416
Se	0.300	0.500	0.900	0.567	0.306
Sn	0.050	0.050	0.050	0.050	0.000
Sr	0.800	1.400	1.100	1.100	0.300
Ta	0.005	0.005	0.005	0.005	0.000
Te	0.050	0.050	0.050	0.050	0.000
Th	0.130	0.090	0.070	0.097	0.031
U	0.070	0.040	0.050	0.053	0.015
V	4.000	3.000	6.000	4.333	1.528
W	0.700	1.000	0.600	0.767	0.208
Zn	18.800	12.500	16.900	16.067	3.232
Zr	1.000	1.000	1.000	1.000	0.000
Sc	2.000	1.000	2.000	1.667	0.577
Y	5.700	4.500	7.500	5.900	1.510
La	2.520	3.040	2.110	2.557	0.466
Ce	4.420	4.190	2.950	3.853	0.791
Pr	0.520	0.690	0.470	0.560	0.115
Nd	2.330	2.760	2.220	2.437	0.285
Sm	0.510	0.490	0.510	0.503	0.012
Eu	0.360	0.299	0.347	0.335	0.032
Gd	0.660	0.490	0.710	0.620	0.115
Tb	0.110	0.090	0.130	0.110	0.020
Dy	0.700	0.550	0.840	0.697	0.145
Ho	0.160	0.120	0.190	0.157	0.035
Er	0.490	0.370	0.610	0.490	0.120
Tm	0.074	0.056	0.100	0.077	0.022
Yb	0.500	0.380	0.700	0.527	0.162
Lu	0.082	0.062	0.124	0.089	0.032

LCMR02 Mount Richardson	LCMR03 Mount Richardson	LCMR16 Mount Richardson	AVERAGE Mount Richardson	STAND_DEV Mount Richardson	NET LOSS % Mount Richardson
PKD11001 26.000 BIF supergene	PKD11001 32.500 BIF supergene	PKD11001 75.000 BIF supergene	PKD11001 BIF	PKD11001 BIF	PKD11001 BIF
					0.900
2.120	3.720	2.060	2.633	0.942	-93.828
0.010	0.006	0.004	0.007	0.003	58.730
1.800	0.750	1.560	1.370	0.550	243.358
91.440	84.500	84.610	86.850	3.975	90.398
0.035	0.046	3.502	1.194	1.999	3586.214
0.030	0.005	0.050	0.028	0.023	-21.296
0.080	0.050	0.100	0.077	0.025	11.111
0.030	0.100	0.040	0.057	0.038	372.222
0.020	0.005	0.060	0.028	0.028	529.630
0.320	0.160	0.260	0.247	0.081	58.120
0.100	0.200	0.050	0.117	0.076	-89.766
91.330	84.270	84.500	86.700	4.011	95.508
0.025	0.025	2.700	0.917	1.544	3974.074
0.430	0.220	0.140	0.263	0.150	466.308
0.620	0.330	0.500	0.483	0.146	1050.794
19.900	9.700	212.000	80.533	113.968	1082.575
6.000	9.000	4760.000	1591.667	2743.858	52955.556
1.300	0.800	3.700	1.933	1.550	279.085
0.020	0.050	0.090	0.053	0.035	97.531
0.010	0.020	0.040	0.023	0.015	55.556
0.050	0.050	0.400	0.167	0.202	270.370
4.500	7.800	1710.000	574.100	983.720	4696.157
		0.173	0.173		
100.000	14.700	7.300	40.667	51.517	106.640
0.025	0.025	0.060	0.037	0.020	62.963
102.000	23.600	163.000	96.200	69.881	443.503
60.900	56.800	56.900	58.200	2.339	94.779
0.600	0.300	0.050	0.317	0.275	-29.630
5.400	5.500	4.600	5.167	0.493	41.166
0.050	0.050	0.050	0.050	0.000	11.111
0.010	0.005	0.030	0.015	0.013	233.333
2.600	0.800	24.400	9.267	13.137	782.540
0.050	0.050	0.050	0.050	0.000	11.111
0.010	0.010	0.030	0.017	0.012	58.730
218.000	303.000	26600.000	9040.333	15207.177	3383.751
0.500	0.500	3.800	1.600	1.905	166.667
0.020	0.020	0.020	0.020	0.000	233.333
14.400	11.700	1090.000	372.033	621.779	2056.715
0.200	0.200	0.100	0.167	0.058	85.185
1.700	1.700	3.800	2.400	1.212	63.265
0.500	0.200	1.200	0.633	0.513	603.704
0.001	0.005	0.005	0.004	0.003	-27.083
2.800	1.500	2.300	2.200	0.656	78.862
0.900	0.800	1.900	1.200	0.608	135.294
0.050	0.050	0.050	0.050	0.000	11.111
6.200	1.600	36.400	14.733	18.904	1388.215
0.020	0.030	0.005	0.018	0.013	307.407
0.050	0.050	0.050	0.050	0.000	11.111
0.150	0.060	0.120	0.110	0.046	26.437
0.240	0.180	0.640	0.353	0.250	636.111
13.000	7.000	50.000	23.333	23.288	498.291
3.400	0.900	0.300	1.533	1.644	122.222
16.600	11.100	241.000	89.567	131.174	519.410
2.000	2.000	1.000	1.667	0.577	85.185
25.000	13.000	11.000	16.333	7.572	988.889
10.200	10.000	41.300	20.500	18.014	286.064
7.920	4.650	11.700	8.090	3.528	251.586
13.000	22.400	48.200	27.867	18.226	703.537
1.130	0.810	5.810	2.583	2.799	412.566
3.600	3.310	31.400	12.770	16.135	482.307
0.780	0.820	9.820	3.807	5.208	740.324
0.432	0.587	4.750	1.923	2.449	537.177
0.980	1.120	10.100	4.067	5.225	628.793
0.170	0.190	1.620	0.660	0.831	566.667
1.230	1.260	9.430	3.973	4.726	533.705
0.290	0.270	1.850	0.803	0.906	469.740
0.950	0.800	5.440	2.397	2.637	443.462
0.148	0.120	0.828	0.365	0.401	429.469
0.980	0.780	5.840	2.533	2.865	434.459
0.157	0.125	1.040	0.441	0.519	448.093

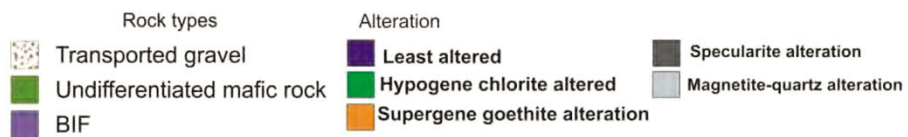
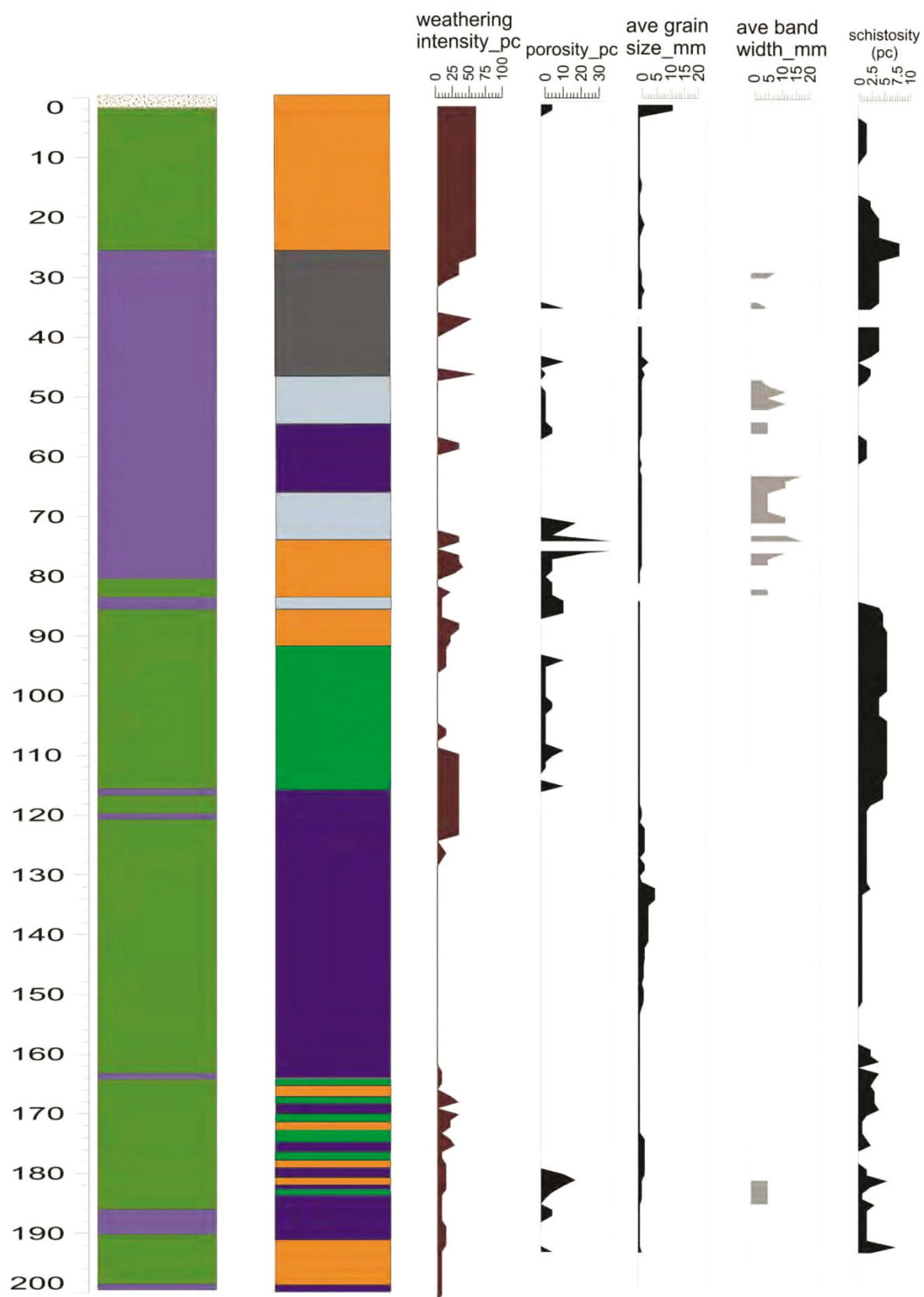
LCMR05 Mount Richardson	LCMR07 Mount Richardson	LCMR08 Mount Richardson	AVERAGE Mount Richardson	STAND_DEV Mount Richardson	NET LOSS % Mount Richardson
PKD11001 38.000 BIF hypogene	PKD11001 46.000 BIF hypogene	PKD11001 46.500 BIF hypogene	PKD11001 BIF	PKD11001 BIF	PKD11001 BIF
					0.700
9.230	28.290	31.490	23.003	12.035	-30.681
0.003	0.002	0.003	0.003	0.001	-18.367
2.230	2.520	0.880	1.877	0.875	504.726
86.420	63.260	66.930	72.203	12.448	103.514
0.213	1.296	0.023	0.511	0.687	1926.455
0.030	0.005	0.020	0.018	0.013	-34.524
0.060	0.040	0.080	0.060	0.020	11.801
0.020	0.070	0.010	0.033	0.032	257.143
0.005	0.005	0.005	0.005	0.000	42.857
0.150	0.150	0.160	0.153	0.006	26.374
0.050	0.050	0.700	0.267	0.375	-69.925
86.310	63.150	66.010	71.823	12.627	108.236
0.025	0.025	0.025	0.025	0.000	42.857
0.400	0.130	0.090	0.207	0.169	471.429
0.790	1.190	0.200	0.727	0.498	2124.490
10.100	6.300	8.800	8.400	1.931	58.590
25.000	12.000	7.000	14.667	9.292	528.571
0.600	0.700	0.600	0.633	0.058	59.664
0.010	0.010	0.010	0.010	0.000	-52.381
0.005	0.010	0.010	0.008	0.003	-28.571
0.050	0.050	0.050	0.050	0.000	42.857
62.000	899.000	4.700	321.900	500.604	3357.573
6.500	6.400	6.800	6.567	0.208	-57.099
0.025	0.050	0.070	0.048	0.023	176.190
51.700	65.500	10.600	42.600	28.559	209.443
54.300	43.000	43.100	46.800	6.495	101.377
0.200	0.300	0.300	0.267	0.058	-23.810
6.400	4.600	4.200	5.067	1.172	77.986
0.050	0.050	0.050	0.050	0.000	42.857
0.005	0.005	0.005	0.005	0.000	42.857
15.000	122.000	1.400	46.133	66.053	5548.980
0.050	0.050	0.050	0.050	0.000	42.857
0.010	0.010	0.005	0.008	0.003	2.041
1380.000	9840.000	127.000	3782.333	5283.370	1773.988
0.500	0.600	0.300	0.467	0.153	0.000
0.010	0.005	0.005	0.007	0.003	42.857
51.400	364.000	7.000	140.800	194.568	949.441
0.100	0.100	0.100	0.100	0.000	42.857
1.200	0.700	0.250	0.717	0.475	-37.318
0.100	0.100	0.200	0.133	0.058	90.476
0.009	0.007	0.007	0.008	0.001	105.357
1.600	0.600	0.900	1.033	0.513	8.014
0.400	0.600	0.600	0.533	0.115	34.454
0.050	0.050	0.050	0.050	0.000	42.857
8.800	7.100	4.000	6.633	2.434	761.472
0.430	0.100	0.005	0.178	0.223	4995.238
0.050	0.050	0.050	0.050	0.000	42.857
0.100	0.050	0.100	0.083	0.029	23.153
0.070	0.040	0.040	0.050	0.017	33.929
10.000	7.000	5.000	7.333	2.517	141.758
4800.000	0.800	0.900	2.167	2.281	303.727
12.300	54.400	8.200	24.967	25.572	121.992
0.050	0.050	2.000	0.700	1.126	0.000
7.000	3.000	2.000	4.000	2.646	242.857
11.400	9.500	7.400	9.433	2.001	128.410
42.000	23.100	10.600	25.233	15.808	1309.946
51.500	66.800	17.000	45.100	25.509	1572.022
7.050	4.150	2.020	4.407	2.525	1024.150
23.000	14.400	8.110	15.170	7.475	789.388
3.400	2.370	1.610	2.460	0.898	598.202
1.210	1.010	0.749	0.990	0.231	321.613
1.760	1.900	1.310	1.657	0.308	281.720
0.270	0.230	0.190	0.230	0.040	198.701
1.650	1.370	1.090	1.370	0.280	180.930
0.340	0.290	0.230	0.287	0.055	161.398
1.000	0.870	0.680	0.850	0.161	147.813
0.153	0.133	0.103	0.130	0.025	141.615
1.020	0.880	0.670	0.857	0.176	132.369
0.163	0.140	0.109	0.137	0.027	119.616

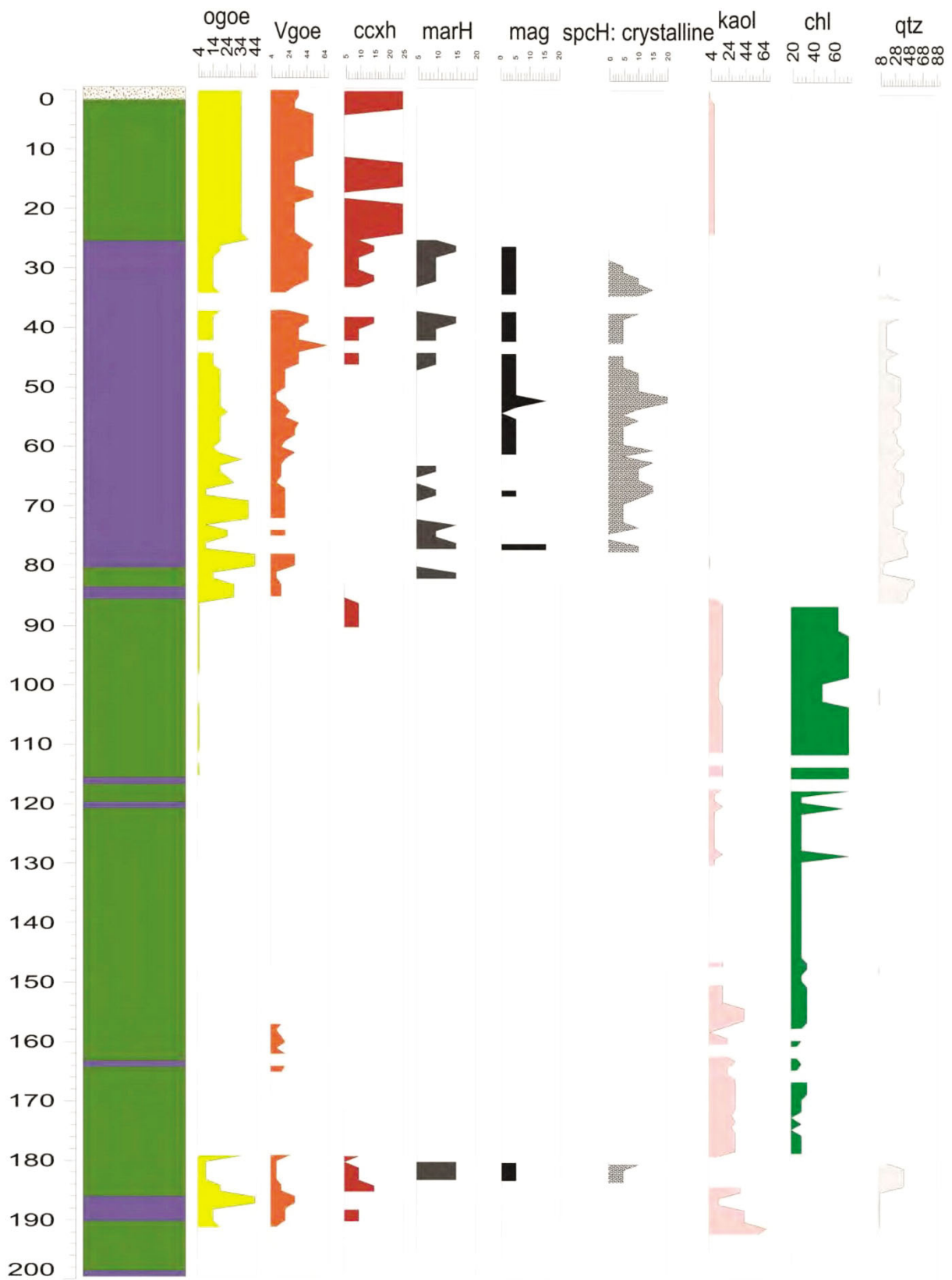
LCMR21 Mount Richardson	LCMR22 Mount Richardson	LCMR23 Mount Richardson	AVERAGE Mount Richardson	STAND_DEV Mount Richardson	LCMR19 Mount Richardson
PKD11001 127.500 gabbro least altered	PKD11001 134.000 gabbro least altered	PKD11001 153.000 gabbro least altered	PKD11001 gabbro	PKD11001 gabbro	PKD11001 96.500 mafic igneous rock supergene/hypogene
distal	distal	distal			intermediate
54.670	56.190	54.340	55.067	0.987	53.850
1.604	1.510	1.394	1.503	0.105	1.560
11.980	11.850	11.780	11.870	0.101	11.660
17.770	17.380	16.880	17.343	0.446	19.760
0.213	0.194	0.211	0.206	0.010	0.088
3.840	3.310	3.190	3.447	0.346	6.410
5.810	6.140	9.970	7.307	2.312	0.450
2.890	2.380	1.560	2.277	0.671	0.070
0.180	0.170	0.190	0.180	0.010	0.020
0.210	0.220	0.210	0.213	0.006	0.240
11.900	11.400	10.100	11.133	0.929	12.800
4.540	4.700	5.650	4.963	0.600	5.530
0.025	0.025	0.025	0.025	0.000	0.025
0.025	0.025	0.025	0.025	0.000	0.025
6.170	6.680	6.150	6.333	0.300	5.770
3.000	2.400	5.400	3.600	1.587	6.400
34.000	36.000	21.000	30.333	8.145	8.000
0.800	0.800	0.700	0.767	0.058	1.100
0.020	0.020	0.030	0.023	0.006	0.060
4.200	4.560	6.850	5.203	1.437	0.300
0.050	0.100	0.300	0.150	0.132	0.050
48.300	45.900	44.000	46.067	2.155	49.800
19.900	14.100	37.600	23.867	12.242	28.600
0.070	0.070	0.140	0.093	0.040	0.310
53.800	45.100	88.600	62.500	23.018	294.000
11.900	11.000	10.700	11.200	0.624	12.700
22.200	22.500	26.600	23.767	2.458	21.700
1.300	1.000	1.600	1.300	0.300	2.200
2.900	3.100	2.600	2.867	0.252	3.000
0.160	0.140	0.160	0.153	0.012	0.020
8.100	8.600	4.700	7.133	2.122	30.300
0.100	0.100	0.100	0.100	0.000	0.100
2.160	1.920	1.750	1.943	0.206	3.380
1510.000	1260.000	1410.000	1393.333	125.831	585.000
0.900	0.200	0.700	0.600	0.361	0.100
2.080	1.950	1.220	1.750	0.464	0.030
34.500	21.200	32.100	29.267	7.088	34.000
3.400	4.400	3.400	3.733	0.577	3.800
1.900	1.700	3.900	2.500	1.217	1.600
1.500	1.100	1.200	1.267	0.208	2.200
0.024	0.006	0.009	0.013	0.010	0.002
0.500	0.700	1.200	0.800	0.361	2.300
1.500	1.700	1.800	1.667	0.153	1.100
0.050	0.050	0.050	0.050	0.000	0.050
49.500	60.900	52.300	54.233	5.941	7.600
0.230	0.320	0.160	0.237	0.080	0.360
0.200	0.050	0.050	0.100	0.087	0.050
1.040	1.260	1.050	1.117	0.124	1.070
0.230	0.280	0.240	0.250	0.026	0.220
225.000	154.000	184.000	187.667	35.642	169.000
0.050	0.050	0.050	0.050	0.000	0.600
97.000	145.000	155.000	132.333	31.005	129.000
99.000	119.000	99.000	105.667	11.547	106.000
43.000	38.000	38.000	39.667	2.887	40.000
45.300	50.900	44.300	46.833	3.557	53.500
6.190	6.240	6.500	6.310	0.166	7.690
15.700	16.300	15.800	15.933	0.321	18.200
2.340	2.430	2.180	2.317	0.127	2.610
11.300	12.300	11.000	11.533	0.681	13.200
3.770	4.280	3.660	3.903	0.331	4.240
1.420	1.630	1.460	1.503	0.112	1.370
5.710	6.240	5.210	5.720	0.515	6.490
1.170	1.260	1.030	1.153	0.116	1.330
8.140	8.550	7.180	7.957	0.703	8.920
1.820	1.900	1.620	1.780	0.144	1.990
5.630	6.060	5.120	5.603	0.471	6.300
0.878	0.957	0.802	0.879	0.078	0.962
5.840	6.490	5.490	5.940	0.507	6.650
0.958	1.100	0.937	0.998	0.089	1.130

LCMR20	AVERAGE	STAND_DEV	NET LOSS %	LCMR17	LCMR18
Mount Richardson	Mount Richardson	Mount Richardson	Mount Richardson	Mount Richardson	Mount Richardson
PKD11001	PKD11001	PKD11001	PKD11001	PKD11001	PKD11001
100.500				86.000	90.500
mafic igneous rock	mafic igneous rock	mafic igneous rock	mafic igneous rock	mafic igneous rock	mafic igneous rock
supergene/hypogene				supergene	supergene
intermediate			0.750	proximal	proximal
47.340	50.595	4.603	22.506	61.600	61.240
0.541	1.051	0.721	-6.788	0.349	0.364
12.540	12.100	0.622	35.917	14.750	14.730
11.900	15.830	5.558	21.699	16.910	16.460
0.165	0.127	0.054	-18.123	0.014	0.073
7.210	6.810	0.566	163.443	0.070	0.170
7.880	4.165	5.254	-23.996	0.060	0.080
1.830	0.950	1.245	-44.363	0.030	0.040
0.050	0.035	0.021	-74.074	0.010	0.110
0.080	0.160	0.113	0.000	0.090	0.100
9.200	11.000	2.546	31.737	0.050	0.050
1.670	3.600	2.729	-3.291	16.800	16.350
0.025	0.025	0.000	33.333	0.025	0.060
0.025	0.025	0.000	33.333	0.025	0.025
6.470	6.120	0.495	28.842	6.580	6.830
3.600	5.000	1.980	85.185	14.700	11.200
18.000	13.000	7.071	-42.857	9.000	72.000
0.500	0.800	0.424	39.130	1.400	0.800
0.040	0.050	0.014	185.714	0.010	0.010
5.640	2.970	3.776	-23.895	0.040	0.050
0.100	0.075	0.035	-33.333	0.050	0.050
48.300	49.050	1.061	41.968	9.300	50.000
203.000	115.800	123.319	546.927	286.000	375.000
0.110	0.210	0.141	200.000	0.060	0.120
132.000	213.000	114.551	354.400	24.800	20.800
8.080	10.390	3.267	23.690	10.700	10.800
14.400	18.050	5.162	1.262	12.900	13.300
1.300	1.750	0.636	79.487	3.400	2.400
1.000	2.000	1.414	-6.977	0.500	0.500
0.040	0.030	0.014	-73.913	0.010	0.080
14.000	22.150	11.526	314.019	47.100	34.100
0.050	0.075	0.035	0.000	0.050	0.050
3.750	3.565	0.262	144.597	0.040	0.090
1160.000	872.500	406.586	-16.507	99.000	546.000
0.300	0.200	0.141	-55.556	0.100	0.200
1.300	0.665	0.898	-49.333	0.020	0.030
93.600	63.800	42.144	190.661	145.000	84.700
1.000	2.400	1.980	-14.286	0.300	0.200
1.500	1.550	0.071	-17.333	0.250	0.250
1.300	1.750	0.636	84.211	0.400	3.800
0.007	0.005	0.004	-53.846	0.013	0.010
0.600	1.450	1.202	141.667	0.400	0.900
0.500	0.800	0.424	-36.000	0.600	0.500
0.050	0.050	0.000	33.333	0.050	0.050
39.300	23.450	22.415	-42.348	4.400	5.500
0.040	0.200	0.226	12.676	0.005	0.005
0.050	0.050	0.000	-33.333	0.050	0.050
0.360	0.715	0.502	-14.627	0.220	0.220
0.070	0.145	0.106	-22.667	0.130	0.330
186.000	177.500	12.021	26.110	184.000	171.000
0.100	0.350	0.354	833.333	0.600	0.300
78.200	103.600	35.921	4.383	34.000	40.600
35.000	70.500	50.205	-11.041	15.000	17.000
39.000	39.500	0.707	32.773	43.000	44.000
21.300	37.400	22769.000	6.477	98.900	8.900
2.970	5.330	3.338	12.625	1.060	1.470
5.800	12.000	8.768	0.418	1.250	3.180
0.880	1.745	1.223	0.432	0.530	0.470
4.500	8.850	6.152	2.312	4.230	2.390
1.430	2.835	1.987	-3.160	3.630	0.820
0.585	0.978	0.555	-13.304	2.700	0.457
2.250	4.370	2.998	1.865	9.760	1.100
0.460	0.895	0.615	3.468	2.150	0.210
3.270	6.095	3.995	2.137	16.100	1.470
0.740	1.365	0.884	2.247	3.880	0.330
2.380	4.340	2.772	3.272	12.500	1.060
0.379	0.671	0.412	1.706	1.890	0.171
2.560	4.605	2.892	3.367	11.900	1.240
0.404	0.767	0.513	2.437	1.720	0.240

AVERAGE Mount Richardson PKD11001	STAND_DEV Mount Richardson PKD11001	NET LOSS % Mount Richardson PKD11001	Unit Symbol	Detection Limit	Analysis Method
mafic igneous rock	mafic igneous rock	mafic igneous rock			
0.850					
61.420	0.255	31.221	%	0.01	FUS-ICP
0.357	0.011	-72.089	%	0.001	FUS-ICP
14.740	0.014	46092.000	%	0.01	FUS-ICP
16.685	0.318	13.181	%	0.01	FUS-ICP
0.044	0.042	-75.157	%	0.001	FUS-ICP
0.120	0.071	-95.904	%	0.01	FUS-ICP
0.070	0.014	-98.873	%	0.01	FUS-ICP
0.035	0.007	-98.191	%	0.01	FUS-ICP
0.060	0.071	-60.784	%	0.01	FUS-ICP
0.095	0.007	-47.610	%	0.01	FUS-ICP
0.050	0.000	-99.472	%	0.1	TITR
16.575	0.318	292.881	%	0.01	FUS-ICP
0.043	0.025	100.000	ppm	0.05	TD-MS
0.025	0.000	17.647	ppm	0.05	TD-MS
6.705	0.177	24.551	%	0.01	TD-MS
12.950	2.475	323.203	ppm	0.1	TD-MS
40.500	44.548	57.078	ppm	1	TD-MS
1.100	0.424	68.798	ppm	0.1	TD-MS
0.010	0.000	-49.580	ppm	0.02	TD-MS
0.045	0.007	-98.983	%	0.01	TD-MS
0.050	0.000	-60.784	ppm	0.1	TD-MS
29.650	28.779	-24.279	ppm	0.1	TD-MS
			%	0.002	FUS-Na2O2
330.500	62.933	15213.149	ppm	0.5	TD-MS
0.090	0.042	13.445	ppm	0.05	TD-MS
22.800	2.828	-57.082	ppm	0.2	TD-MS
10.750	0.071	12.920	%	0.01	TD-MS
13.100	0.283	-35.154	ppm	0.1	TD-MS
2.900	0.707	162.443	ppm	0.5	FUS-MS
0.500	0.000	-79.480	ppm	0.1	FUS-MS
0.045	0.049	-65.473	%	0.01	TD-MS
40.600	9.192	569.599	ppm	0.5	TD-MS
0.050	0.000	-41.176	ppm	0.1	TD-MS
0.065	0.035	-96.065	%	0.01	TD-MS
322.500	316.077	-72.769	ppm	1	TD-MS
0.150	0.071	-70.588	ppm	0.1	TD-MS
0.025	0.007	-98.319	%	0.01	TD-MS
114.850	42.639	361.678	ppm	0.5	TD-MS
0.250	0.071	-92.122	ppm	0.2	FUS-MS
0.250	0.000	-88.235	ppm	0.5	TD-MS
2.100	2.404	95.046	ppm	0.2	TD-MS
0.012	0.002	4.072	ppm	0.001	TD-MS
0.650	0.354	-4.412	ppm	0.2	FUS-MS
0.550	0.071	-61.176	ppm	0.1	TD-MS
0.050	0.000	17.647	ppm	1	TD-MS
4.950	0.778	-89.262	ppm	0.2	TD-MS
0.005	0.000	-97.514	ppm	0.01	FUS-MS
0.050	0.000	-41.176	ppm	0.1	TD-MS
0.220	0.000	-76.822	ppm	0.05	FUS-MS
0.230	0.141	8.35	ppm	0.01	FUS-MS
177.500	9.192	11.274	ppm	1	TD-MS
0.450	0.212	958.824	ppm	0.1	TD-MS
37.300	4.667	-66.840	ppm	0.2	TD-MS
16.000	1.414	-82.186	ppm	1	FUS-MS
43.500	0.707	29.016	ppm	1	FUS-ICP
53.900	63.640	35.399	ppm	0.5	FUS-MS
1.265	0.290	-76.415	ppm	0.05	FUS-MS
2.215	1.365	-83.645	ppm	0.05	FUS-MS
0.500	0.042	-74.609	ppm	0.01	FUS-MS
3.310	1.301	-66.236	ppm	0.05	FUS-MS
2.225	1.987	-32.938	ppm	0.01	FUS-MS
1.579	1.586	23.529	ppm	0.005	FUS-MS
5.430	6.124	11.682	ppm	0.01	FUS-MS
1.180	1.372	20.367	ppm	0.01	FUS-MS
8.785	10.345	29.895	ppm	0.01	FUS-MS
2.105	2.510	39.128	ppm	0.01	FUS-MS
6.780	8.089	42.352	ppm	0.01	FUS-MS
1.031	1.216	37.924	ppm	0.005	FUS-MS
6.570	7.538	30.125	ppm	0.01	FUS-MS
0.980	1.047	15.487	ppm	0.002	FUS-MS

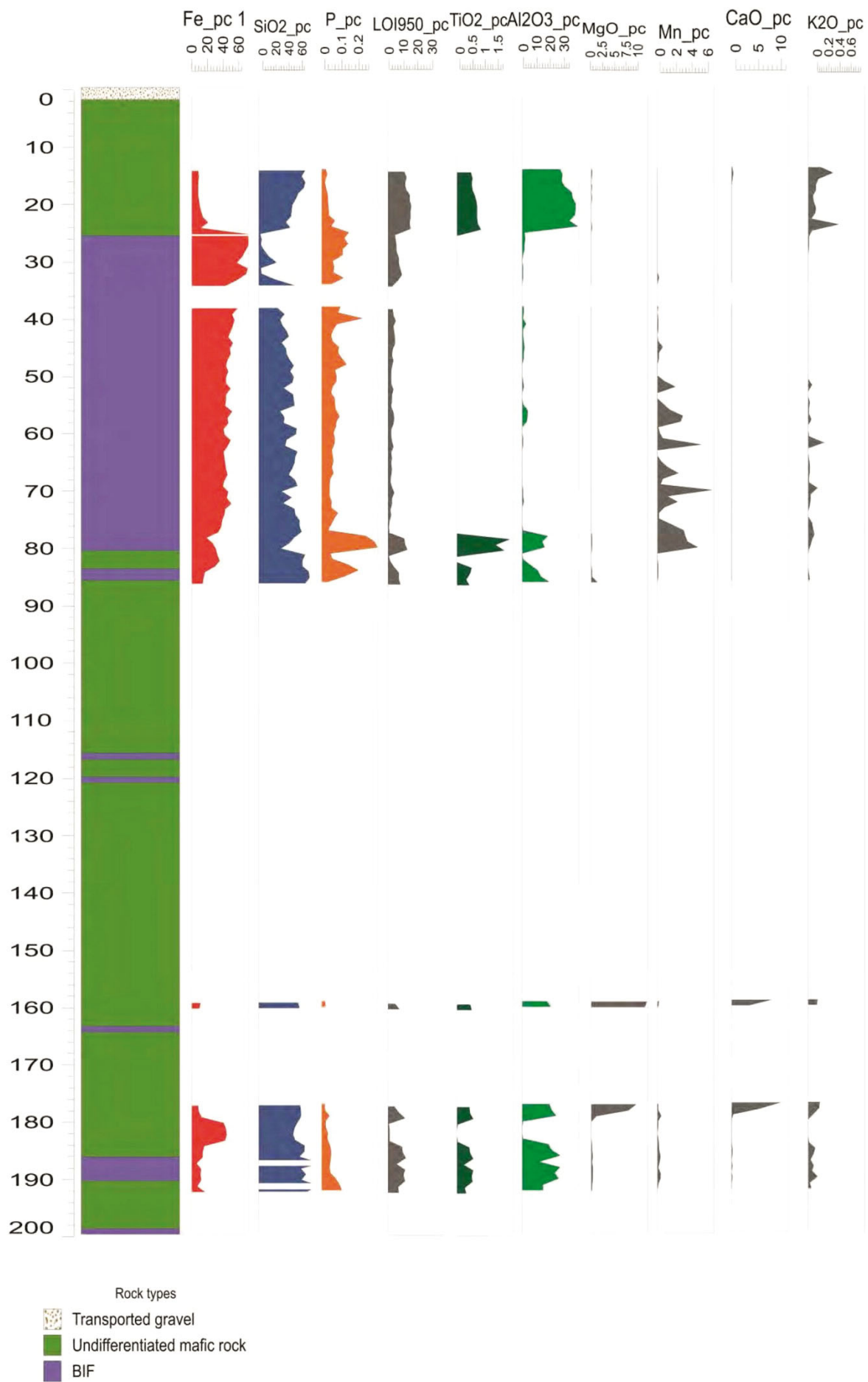
APPENDIX 5: DIAMOND DRILL HOLE LOG

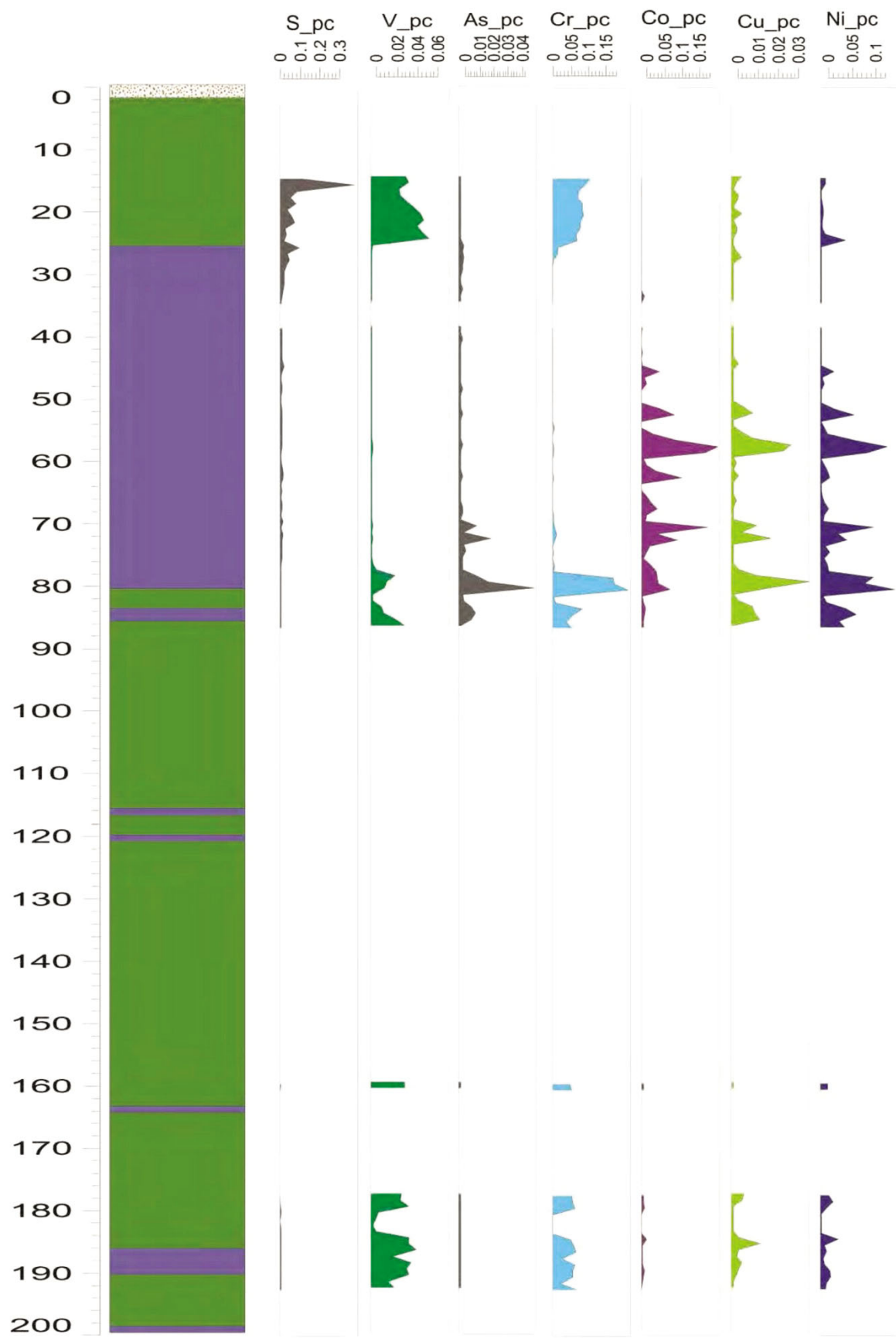




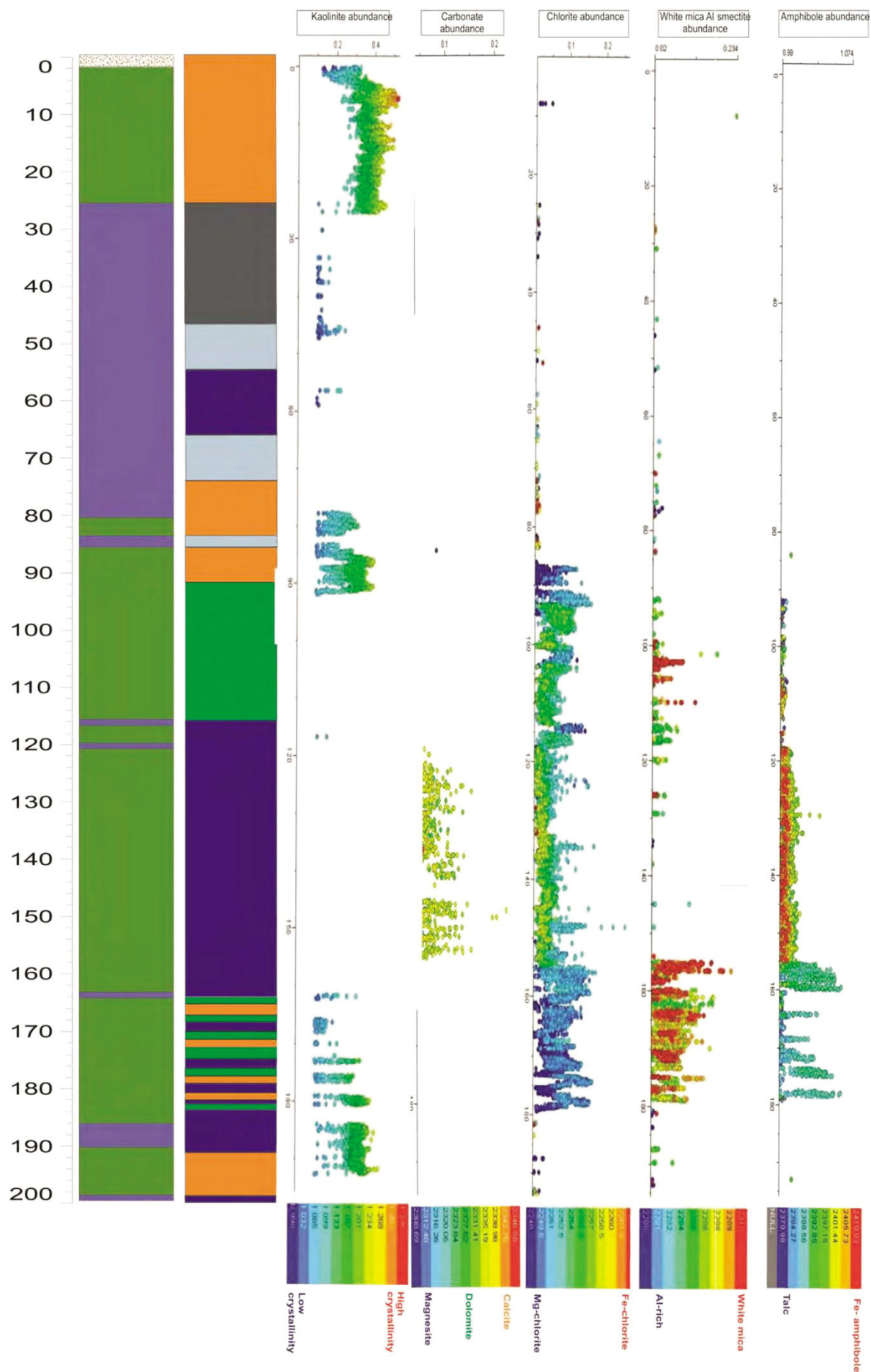
Rock types

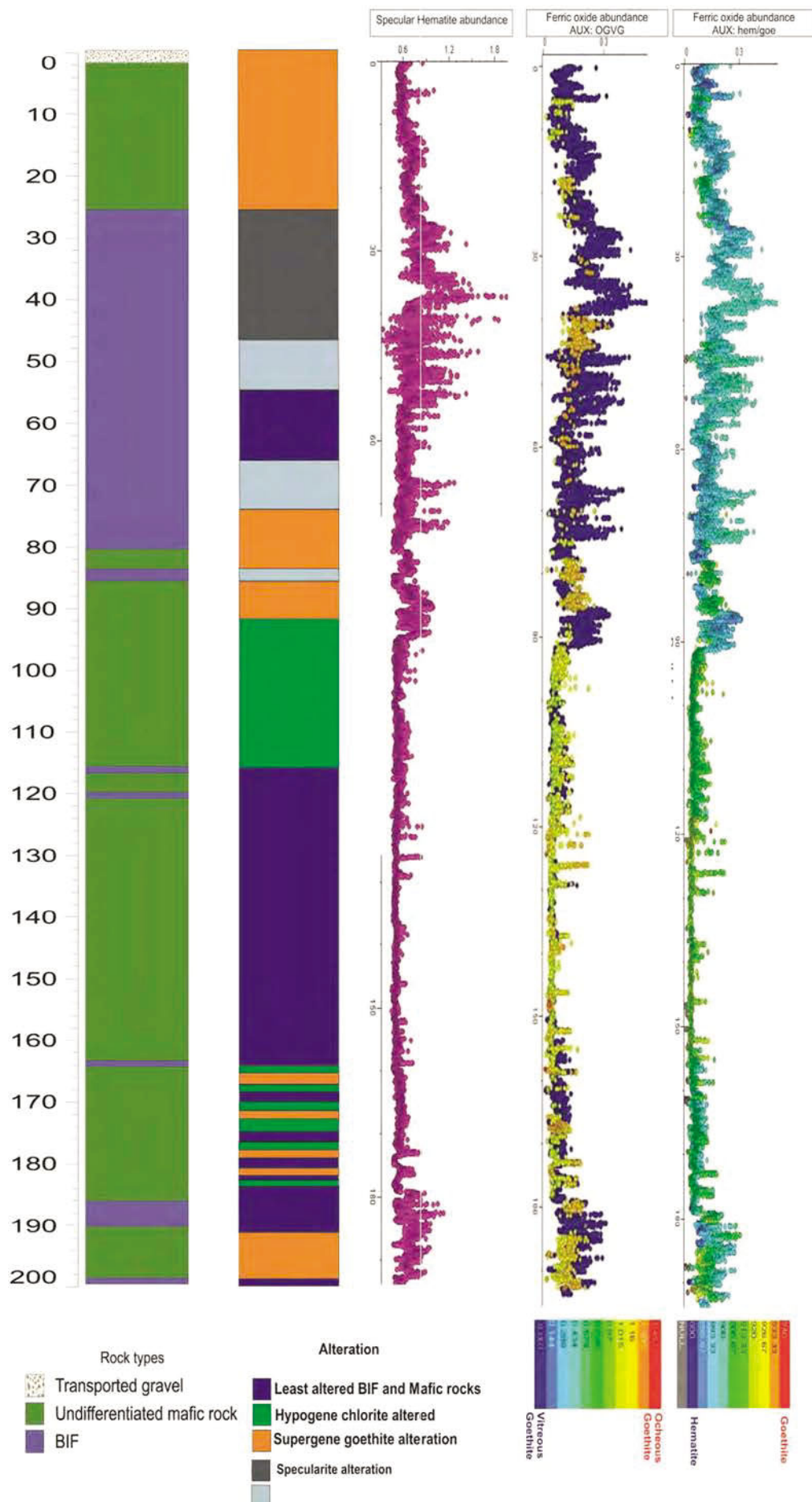
- Transported gravel
- Undifferentiated mafic rock
- BIF





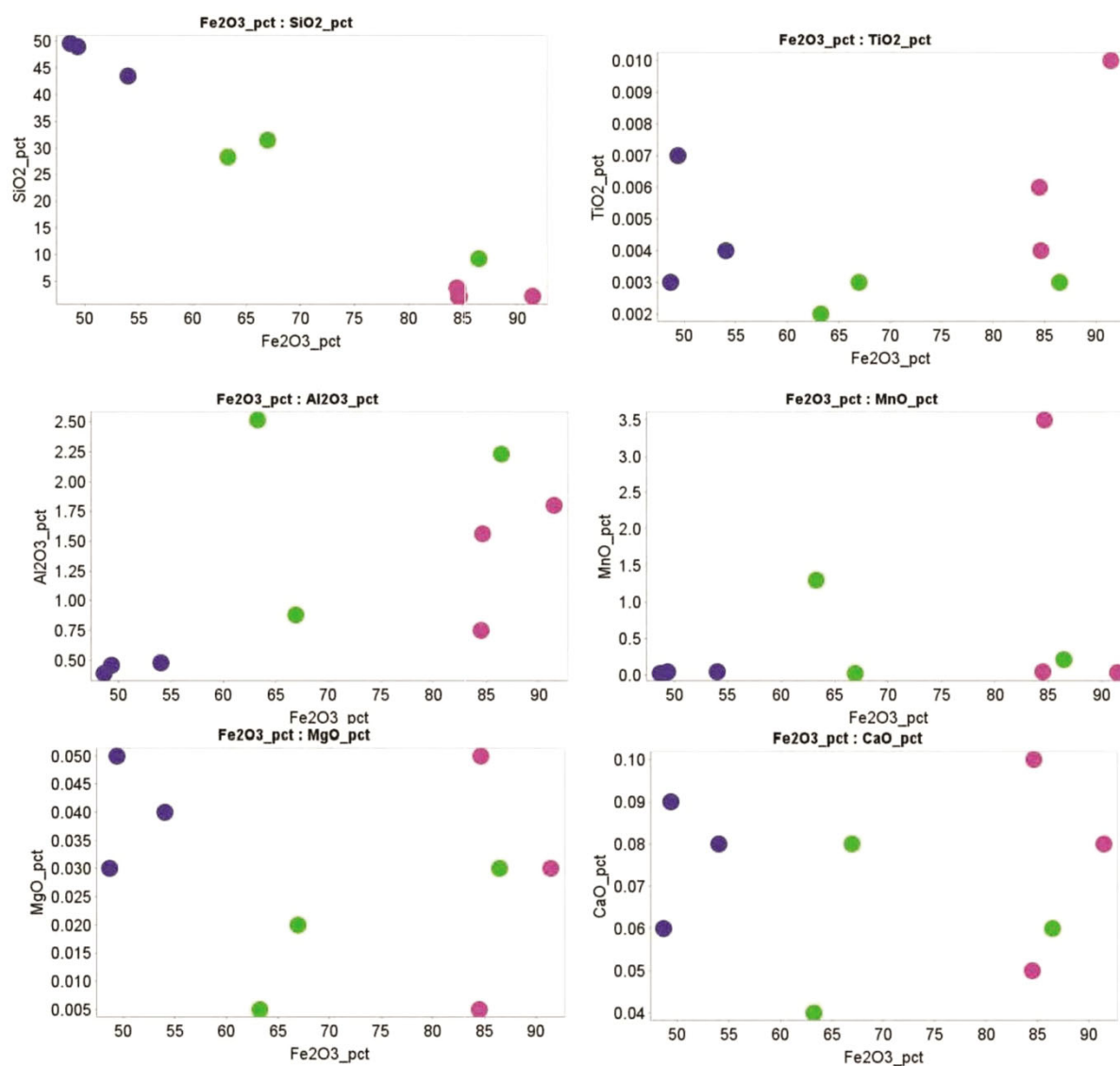
APPENDIX 7: DIAMOND DRILL HOLE HYPERSPECTRAL DATA



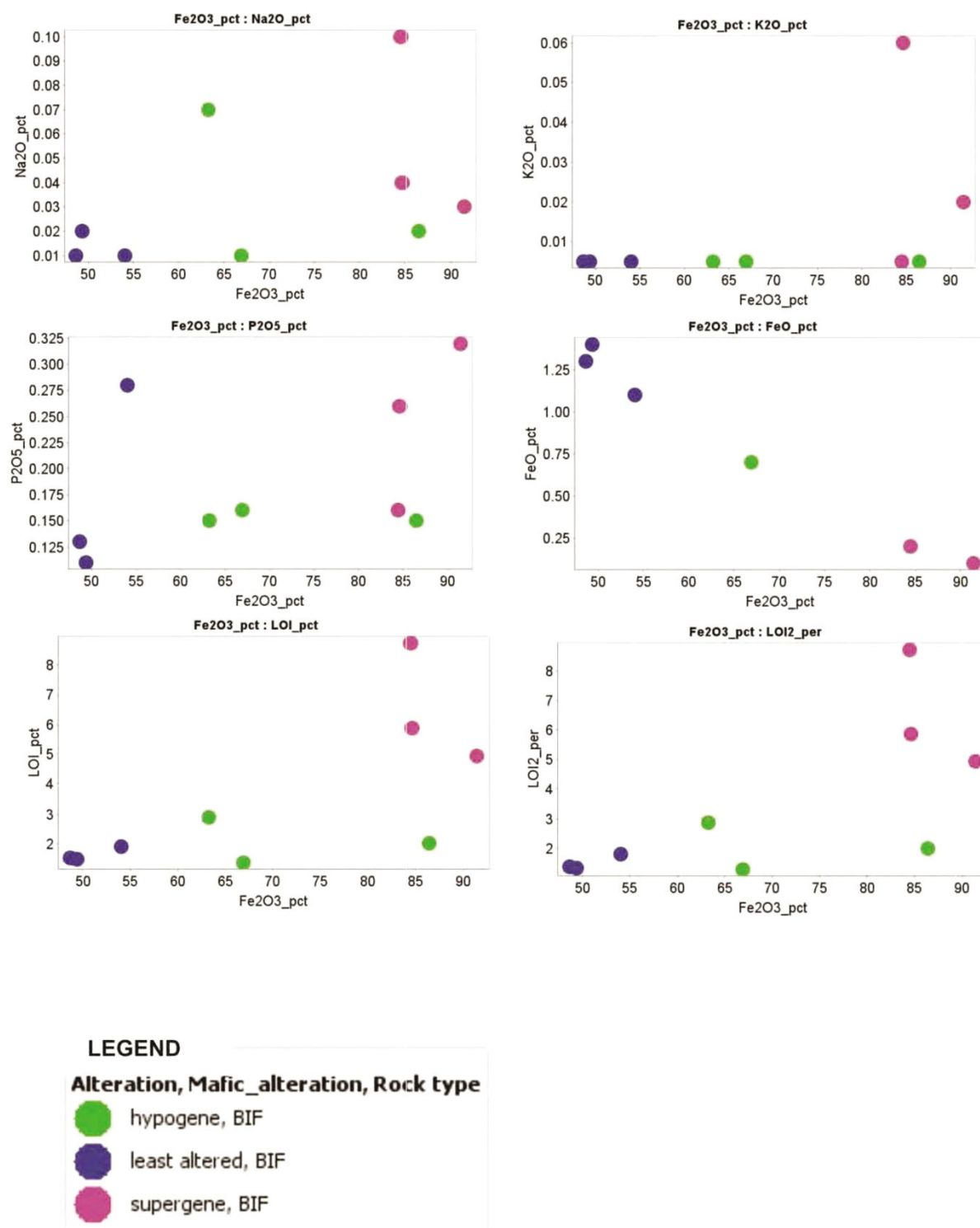


APPENDIX 7: WHOLE ROCK AND TRACE ELEMENT GEOCHEMISTRY

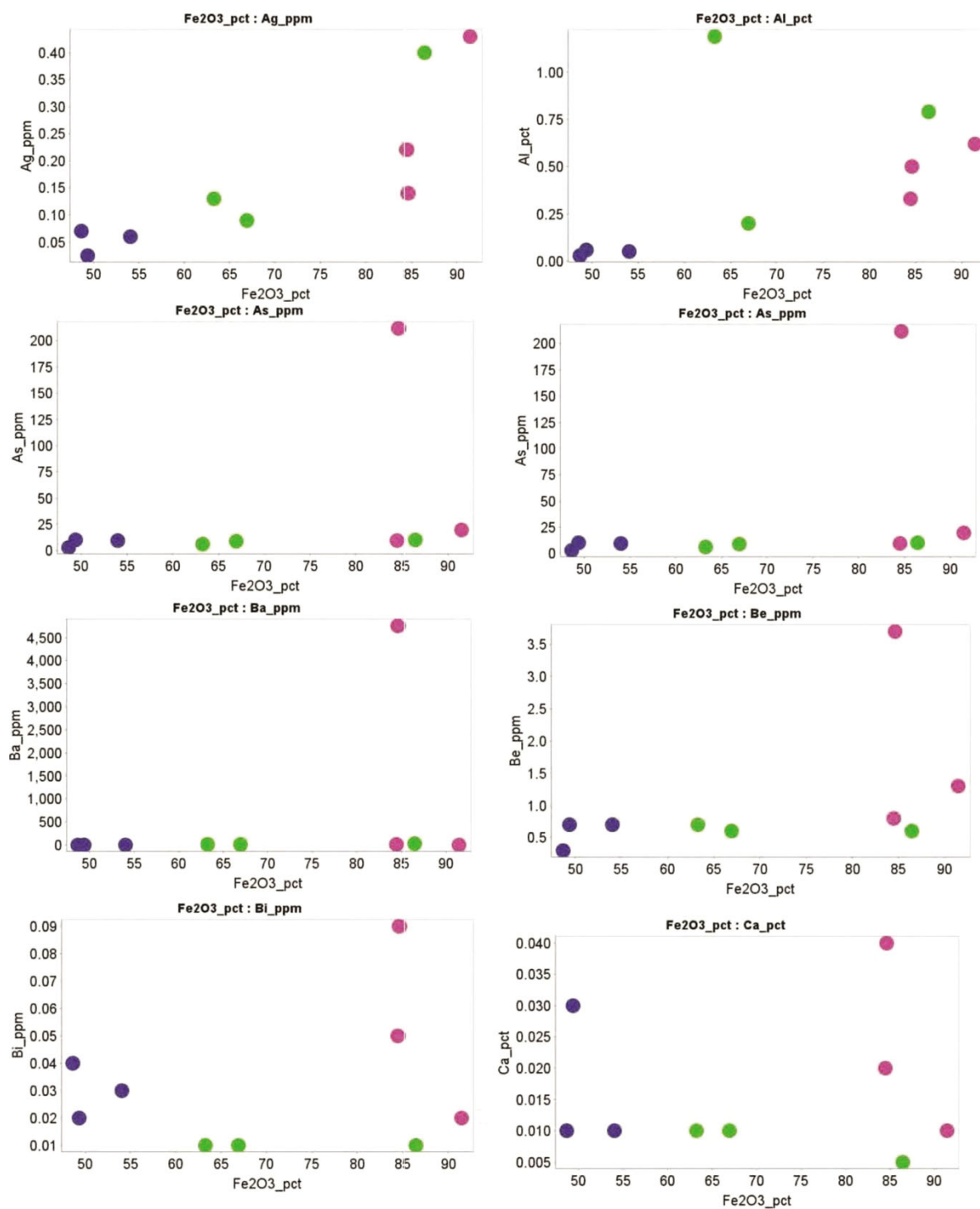
Binary plot showing $\text{Fe}_2\text{O}_{3\text{Total}}$ versus other major element oxides for BIF.



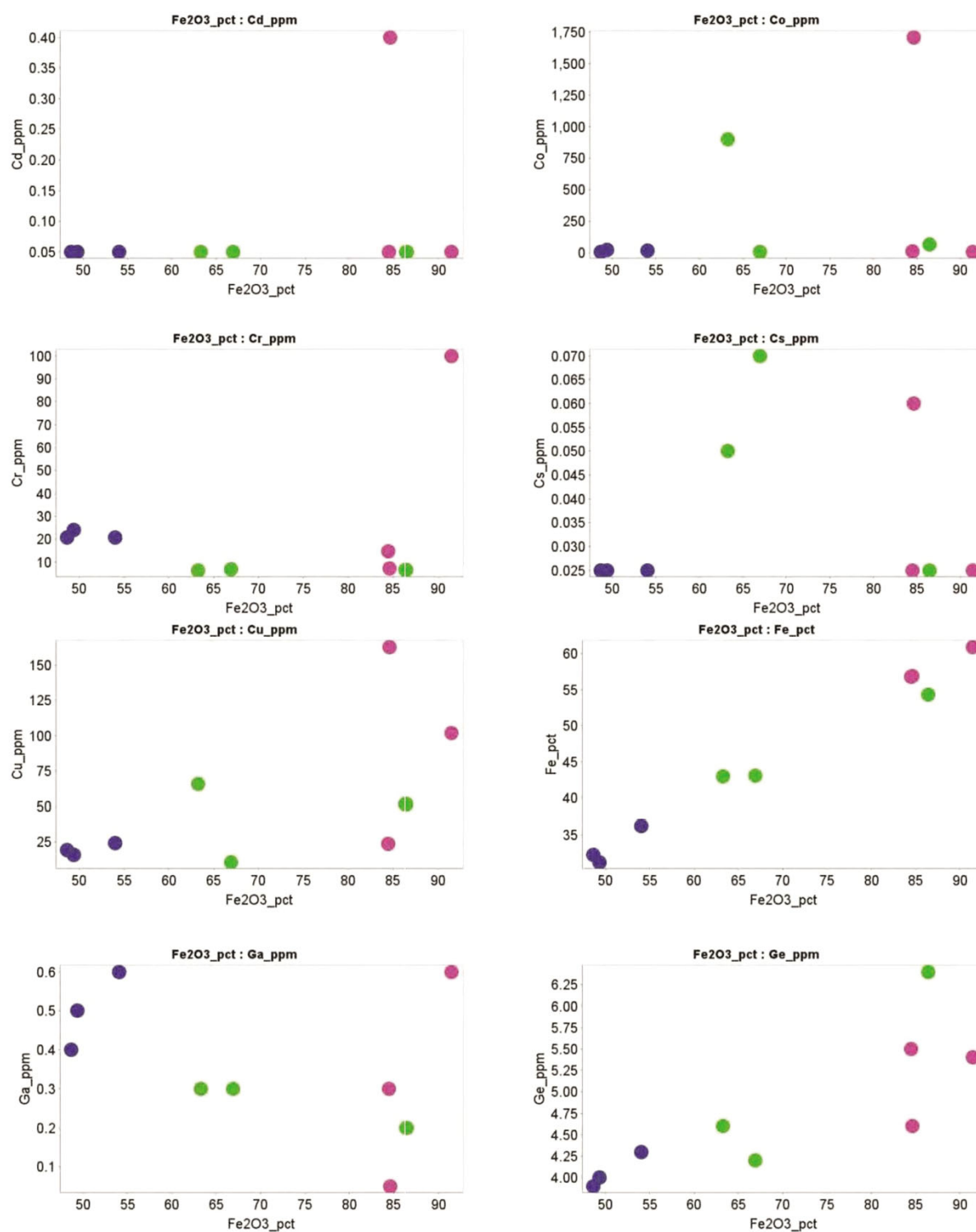
Binary plot showing $\text{Fe}_2\text{O}_{3\text{Total}}$ versus other major element oxides for BIF.



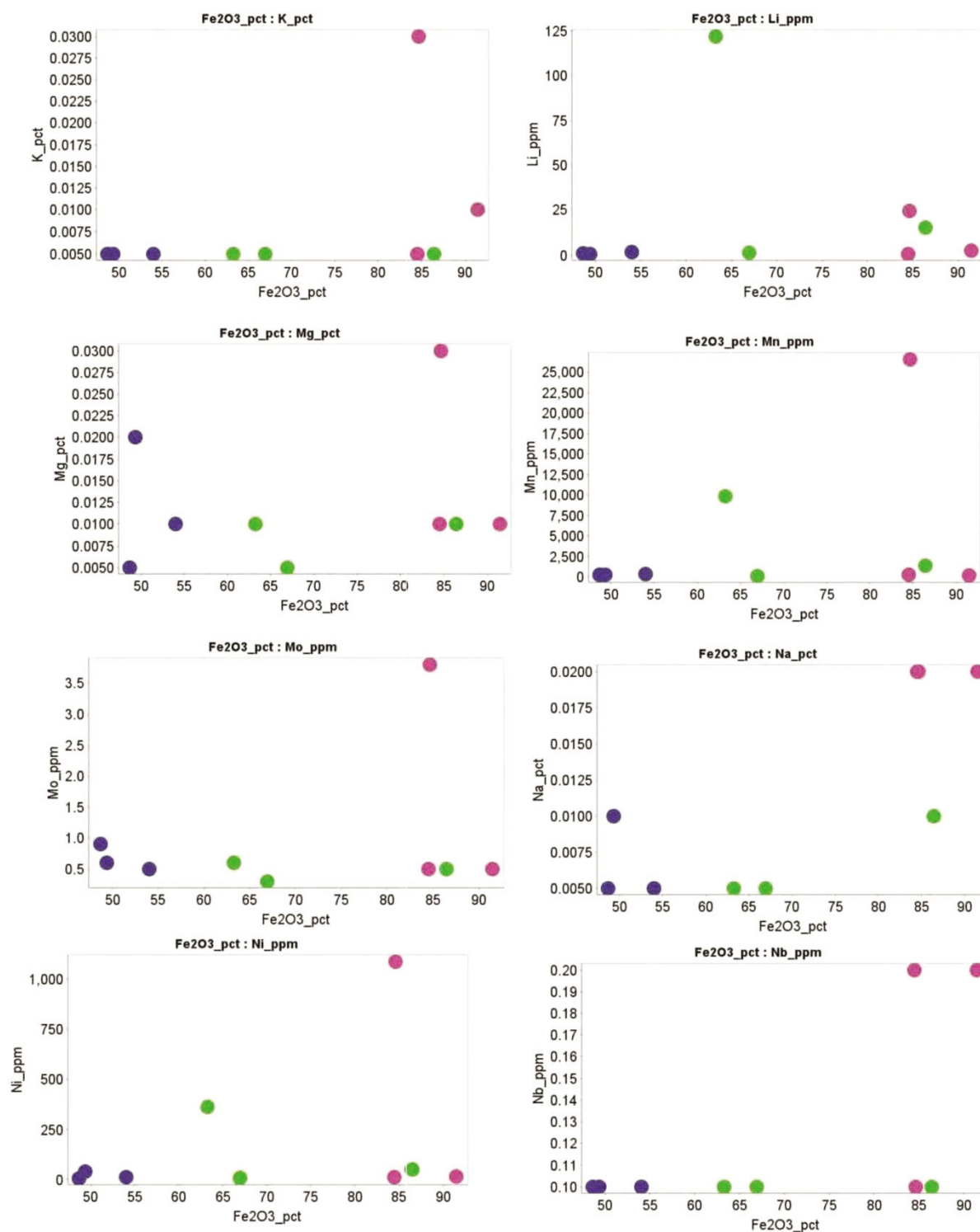
Binary plot showing $\text{Fe}_2\text{O}_{3\text{Total}}$ versus trace elements for BIF.



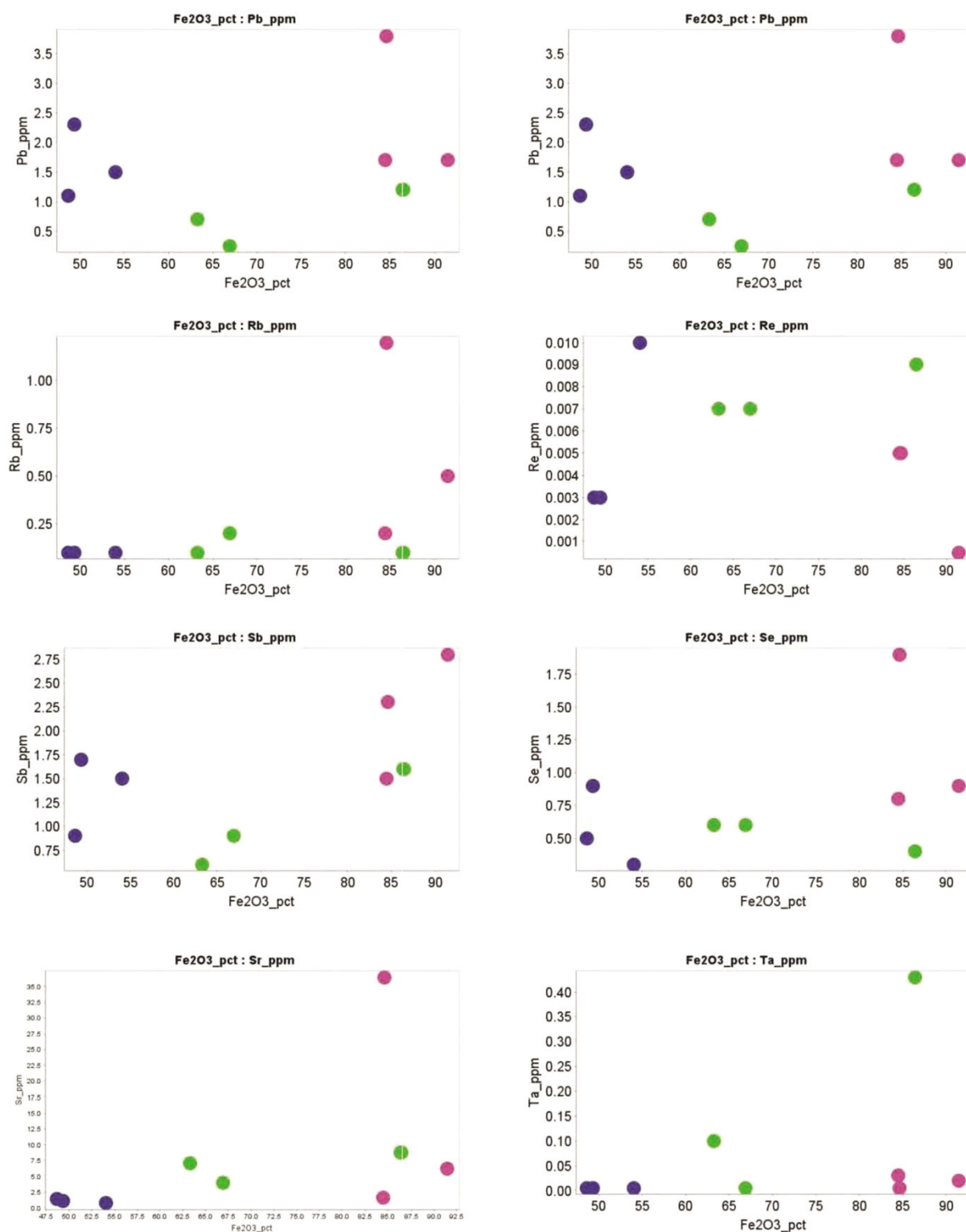
Binary plot showing $\text{Fe}_2\text{O}_{3\text{Total}}$ versus trace elements for BIF.



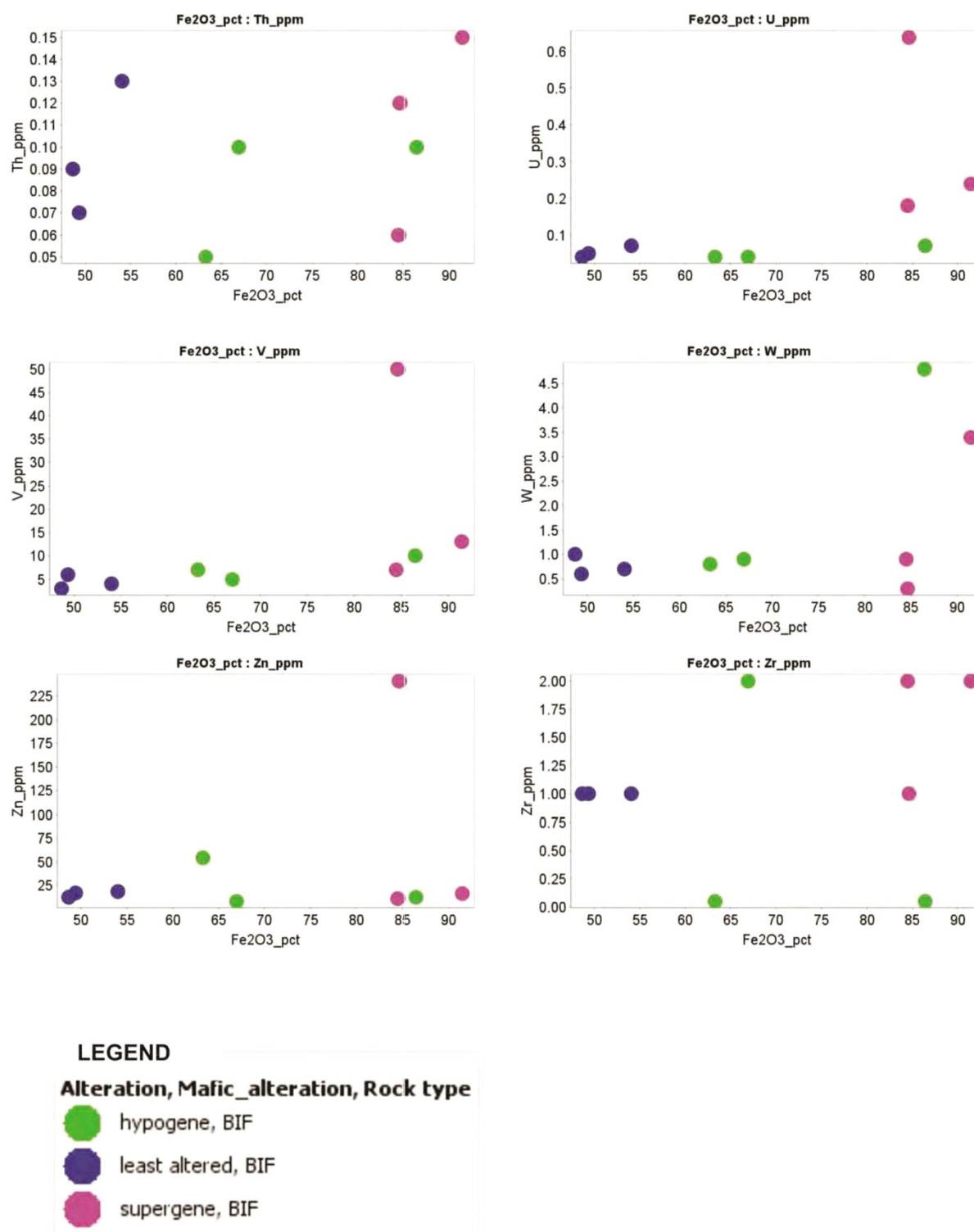
Binary plot showing $\text{Fe}_2\text{O}_{3\text{Total}}$ versus trace elements for BIF.



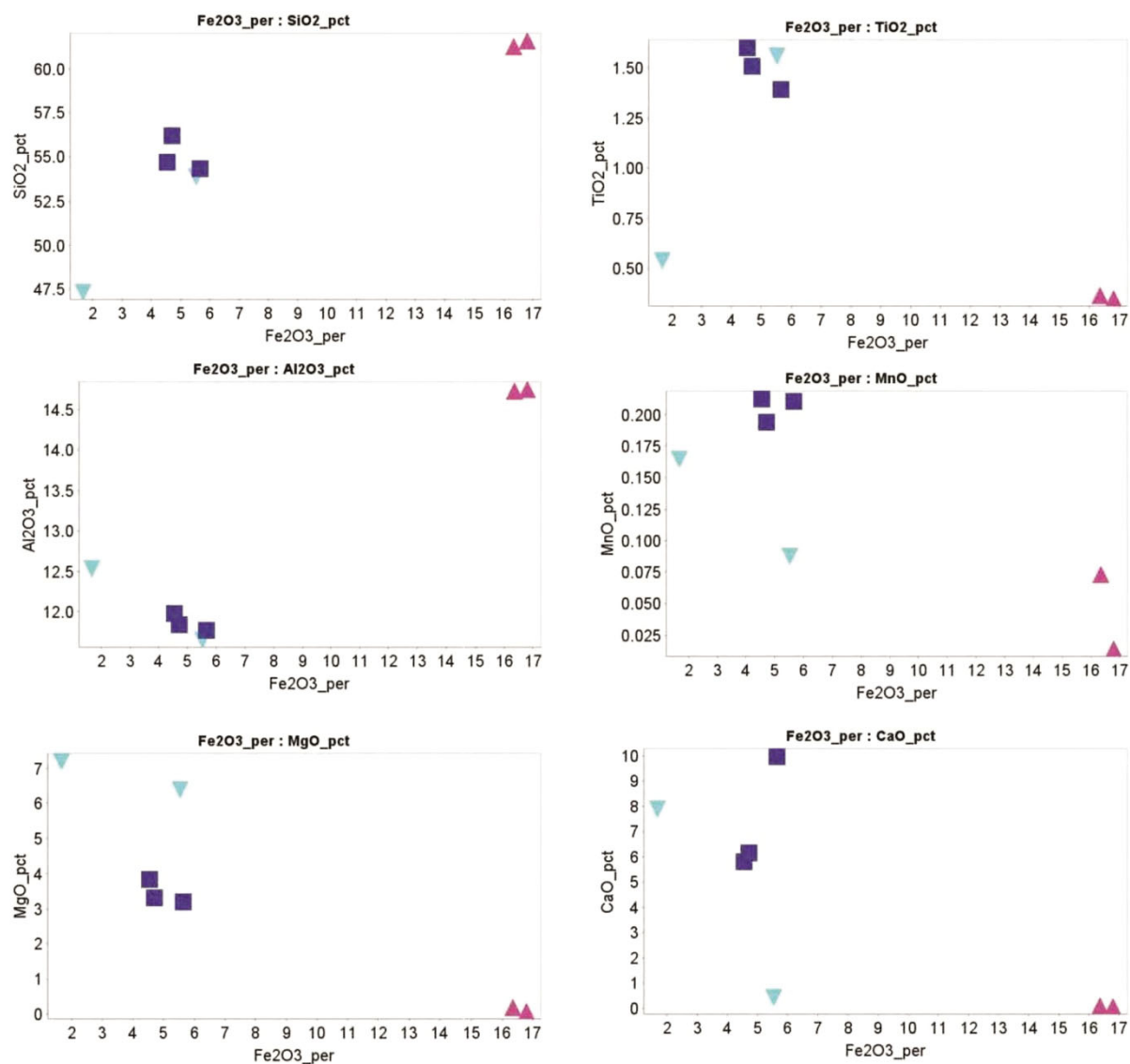
Binary plot showing $\text{Fe}_2\text{O}_{3\text{Total}}$ versus trace elements for BIF.



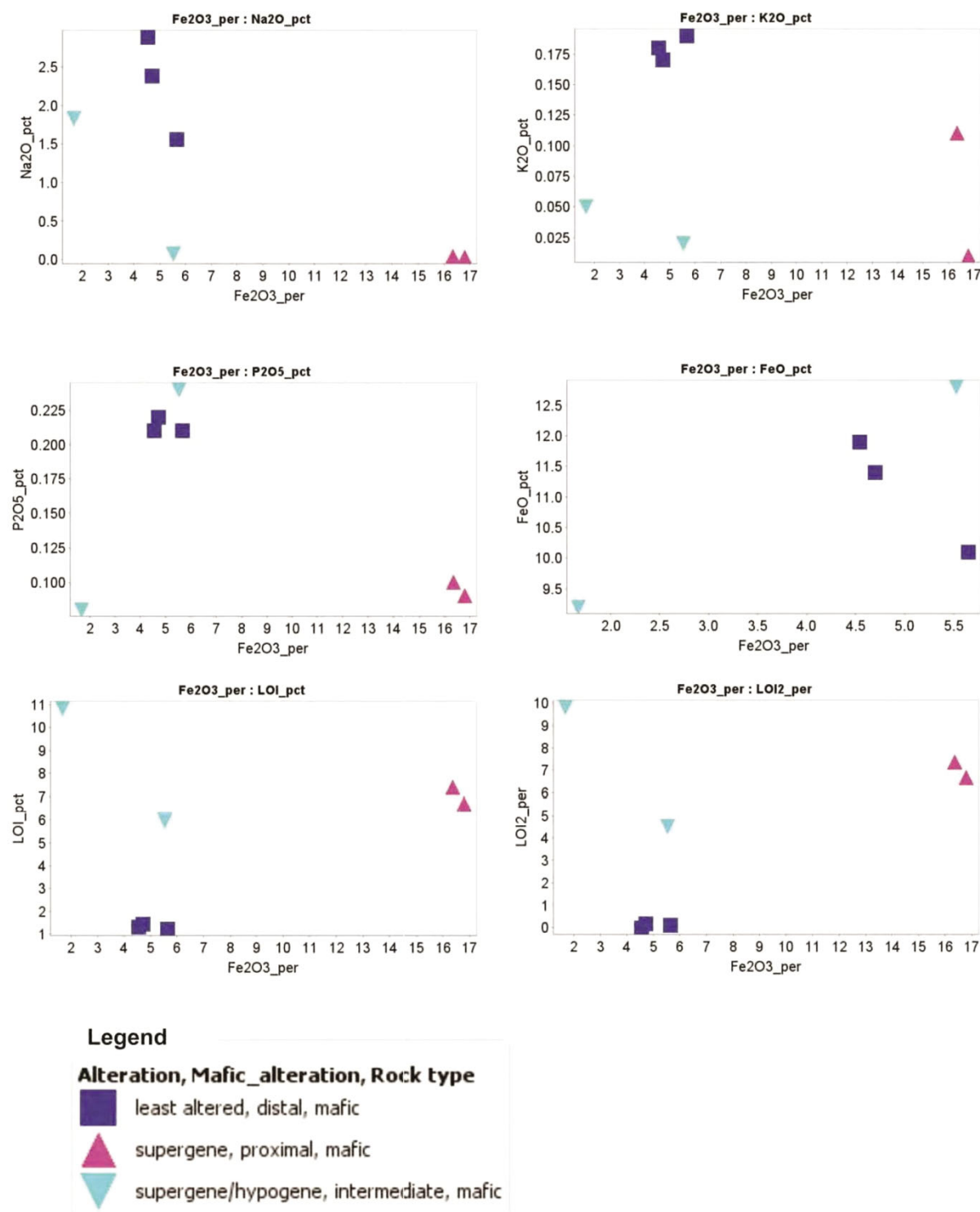
Binary plot showing $\text{Fe}_2\text{O}_{3\text{Total}}$ versus trace elements for BIF.



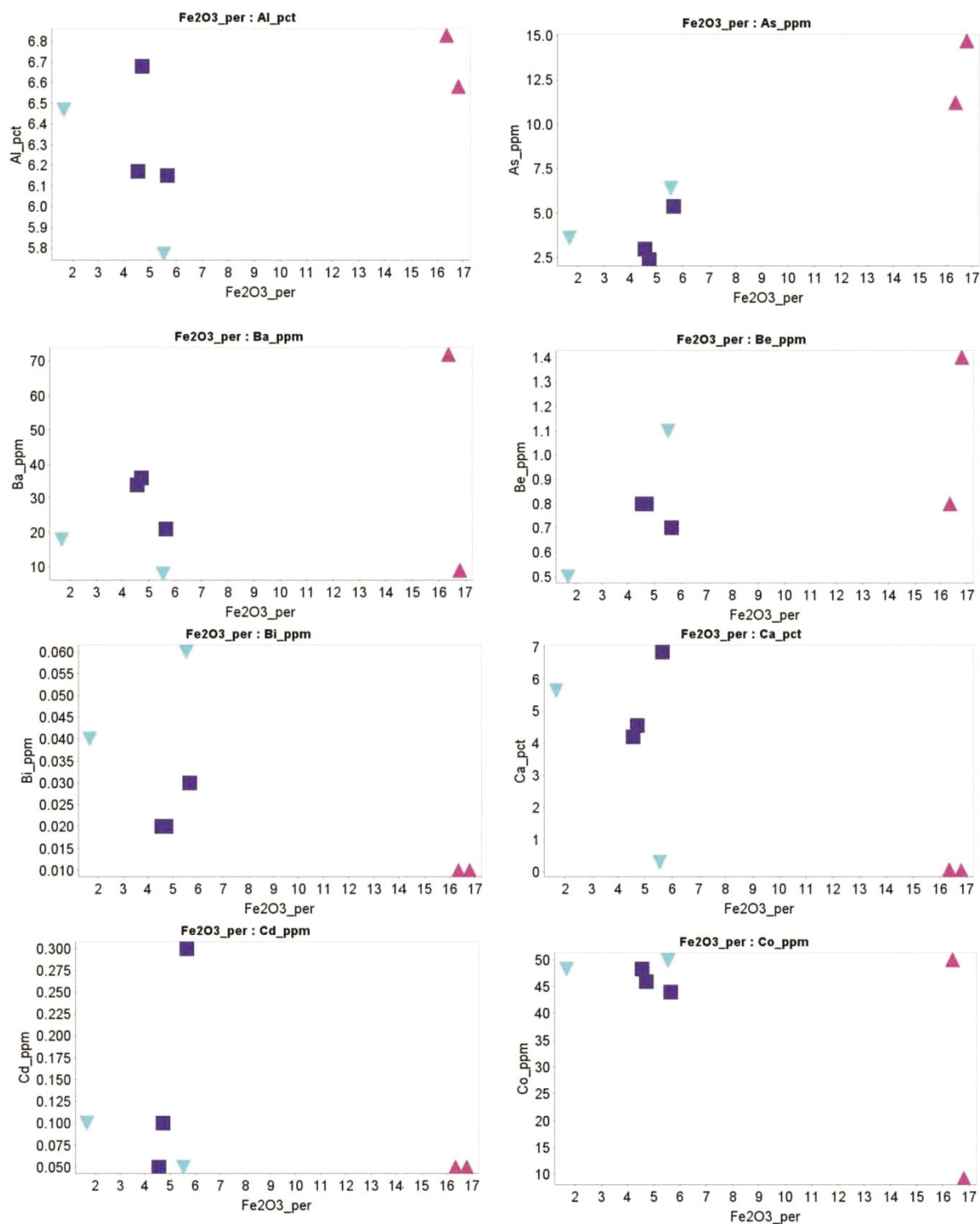
Binary plot showing $\text{Fe}_2\text{O}_{3\text{Total}}$ versus other major element oxides for mafic igneous rocks.



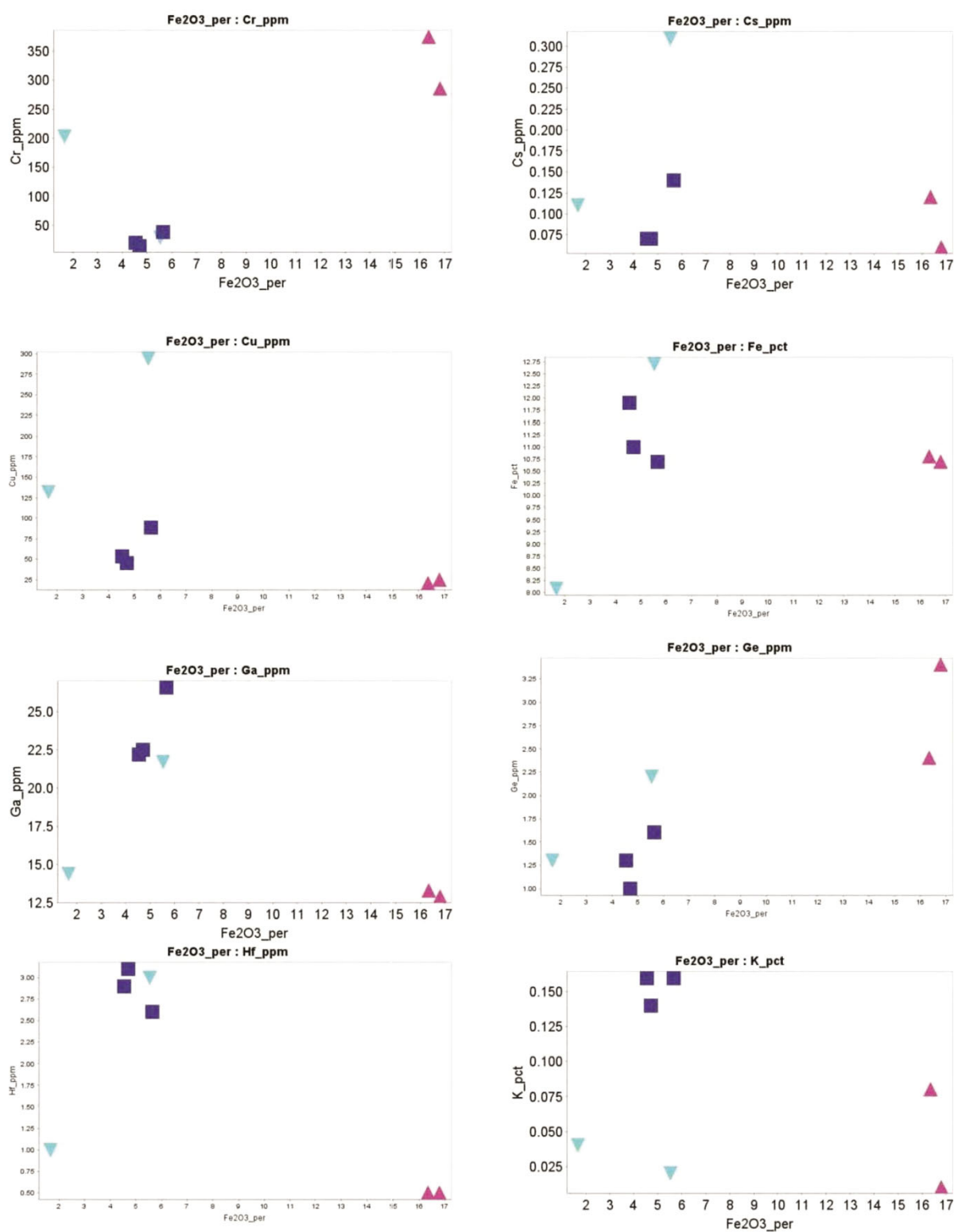
Binary plot showing $\text{Fe}_2\text{O}_{3\text{Total}}$ versus other major element oxides for mafic igneous rocks.



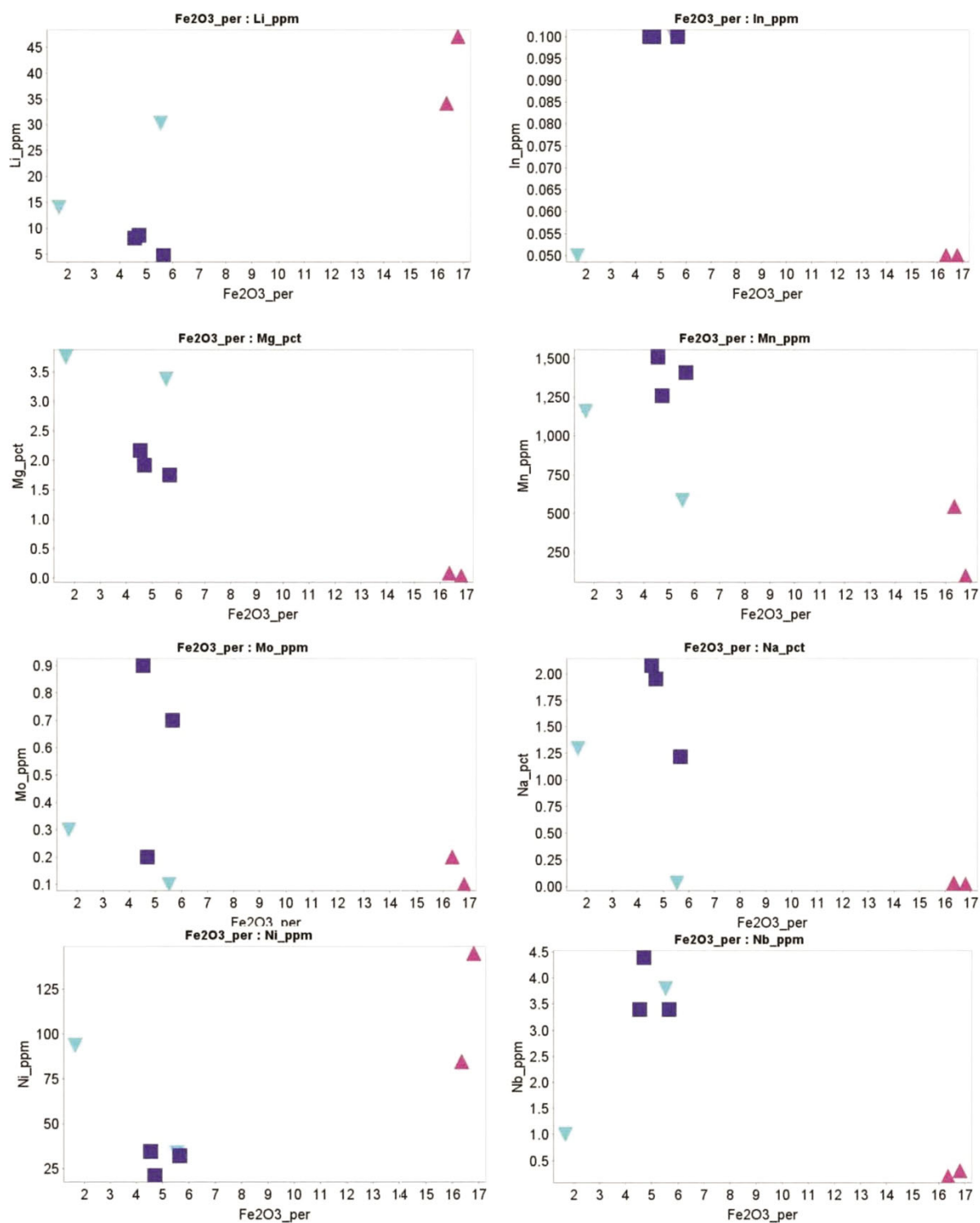
Binary plot showing $\text{Fe}_2\text{O}_{3\text{Total}}$ versus trace elements for mafic igneous rocks.



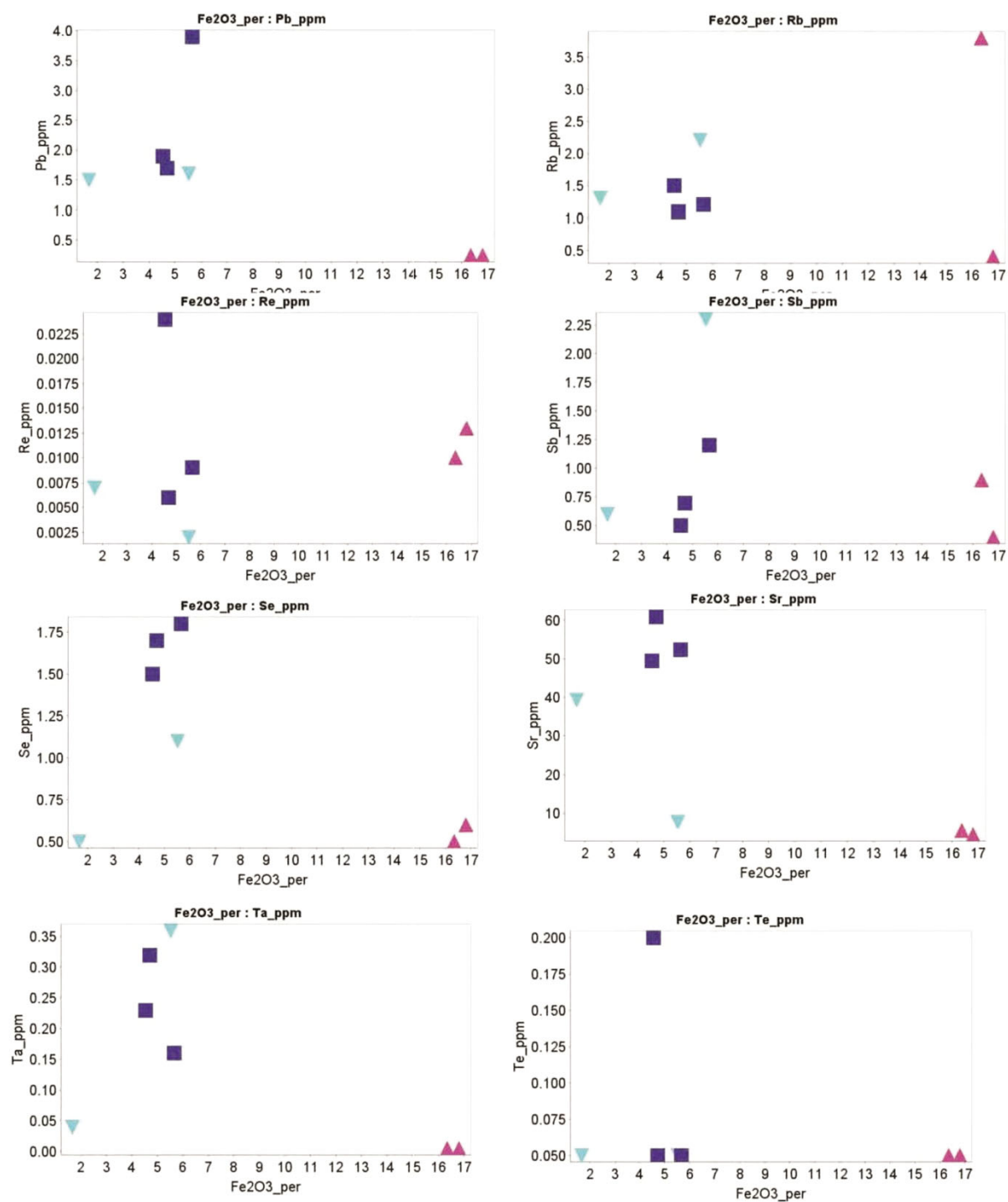
Binary plot showing $\text{Fe}_2\text{O}_{3\text{Total}}$ versus trace elements for mafic igneous rocks.



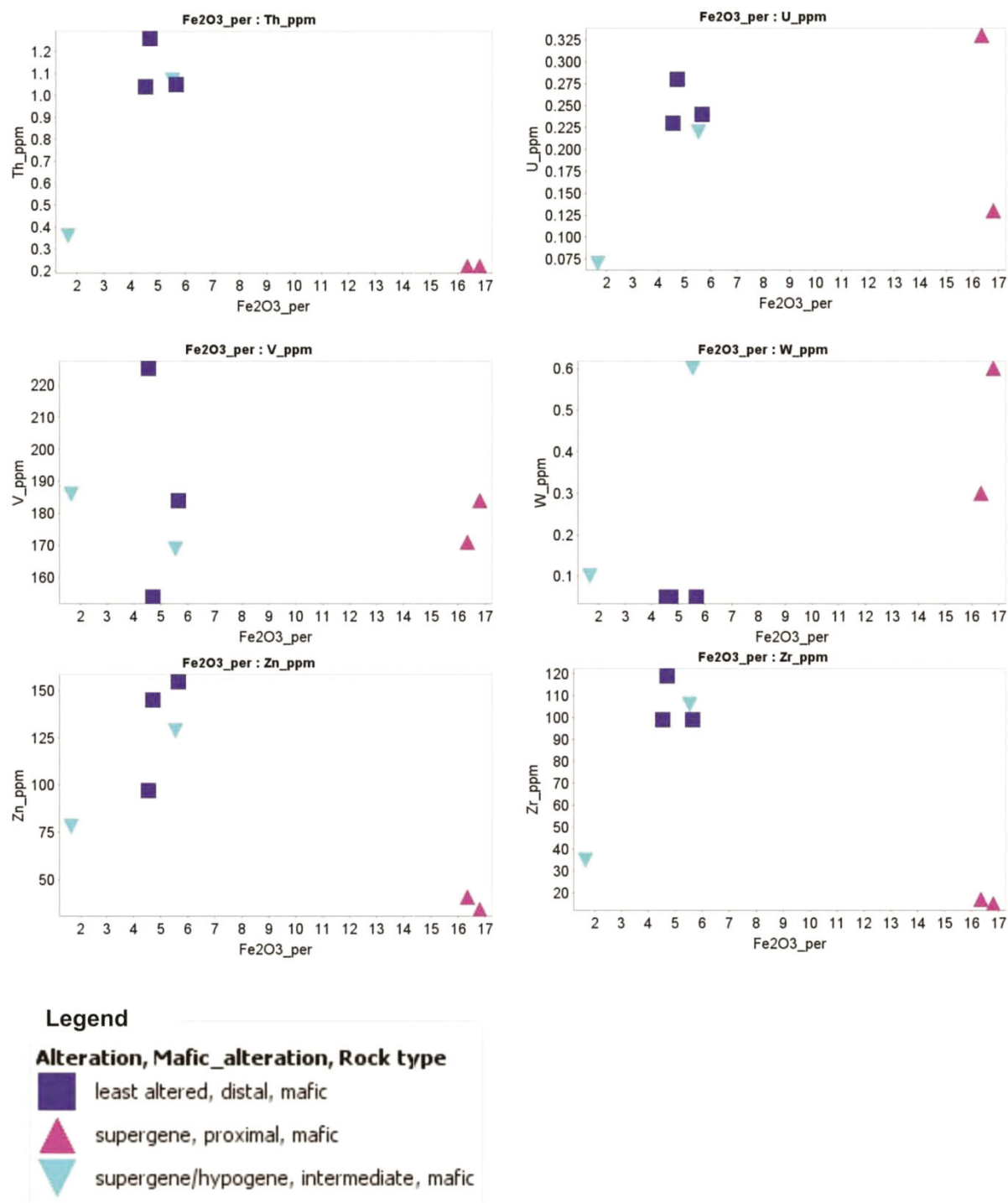
Binary plot showing $\text{Fe}_2\text{O}_{3\text{Total}}$ versus trace elements for mafic igneous rocks.



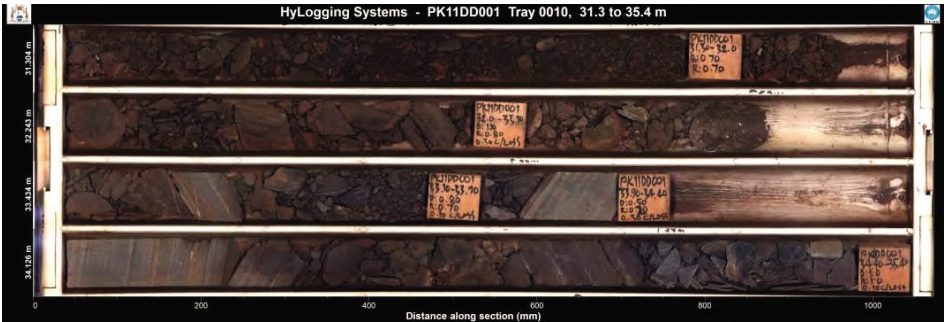

Binary plot showing $\text{Fe}_2\text{O}_{3\text{Total}}$ versus trace elements for mafic igneous rocks.





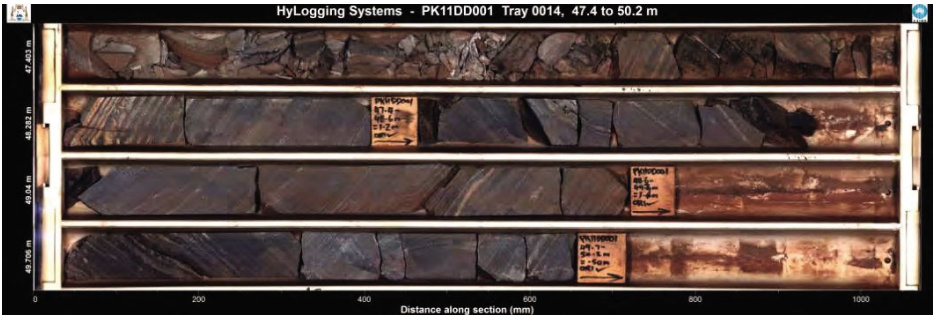
Binary plot showing $\text{Fe}_2\text{O}_{3\text{Total}}$ versus trace elements for mafic igneous rocks.


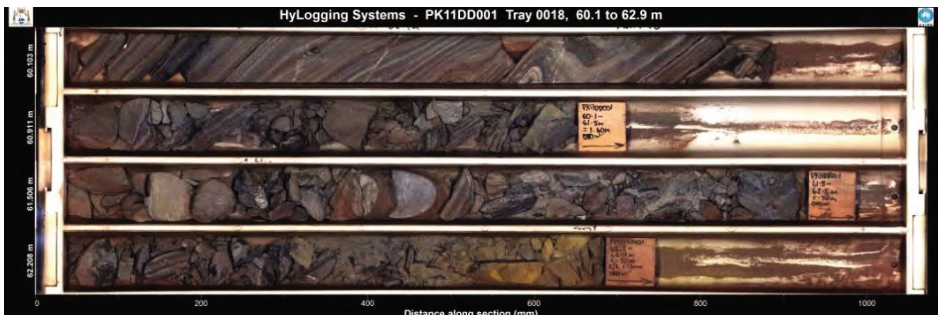


APPENDIX 8: THIN SECTION DESCRIPTIONS


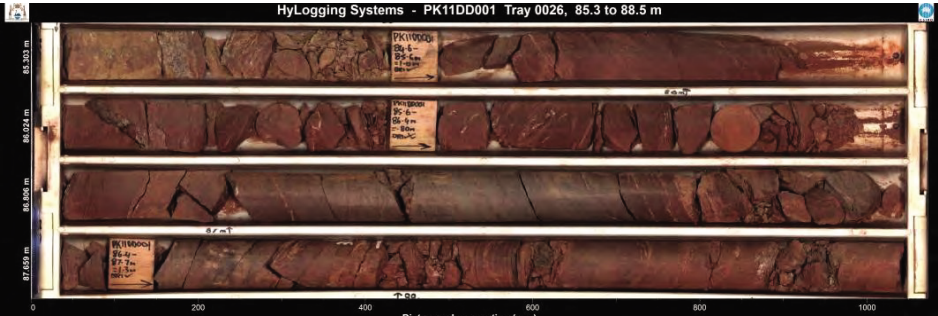
Sample numbers: LCMR04	Mineralogy	Block description
Depth: 32.9m depth	Supergene enriched rock: 90% goethite: 200um 10% void: anhedral, dissolution of quartz Hypogene vein: 70% Hematite, anhedral 30% Goethite, anhedral	BIF that has been highly altered so that no primary banding exists and all silica content has be dissolved. Coarse grained specular hematite veins enrich this rock, overprinting primary bands. Later supergene enrichment of goethite is observed, dissolving silica minerals and replacing with ochreous and vitreous goethite, making a porous rock enriched in iron.
Alteration : Supergene modified hypogene altered BIF		
Images 1. Drill core image		
Sample numbers: LCMR06	Mineralogy	Block description
Depth: 39.5m depth	Silica rich bands: Quartz 85%, anhedral 150um hematite 10%, euhedral 250um Goethite 5%, infill textures of quartz grains Disseminated hematite bands: Hematite 60%, euhedral 250um Quartz 30%, anhedral 150um Goethite 10% euhedral 100um	Thinly banded BIF rock of alternating silica rich and iron rich bands. Hypogene alteration in this rock is observed as disseminated hematite textures in silica rich bands. And alteration of iron oxides to larger anhedral hematite and martite minerals.
Alteration : <i>Hypogene altered BIF</i>		
Images 1. Drill core image		


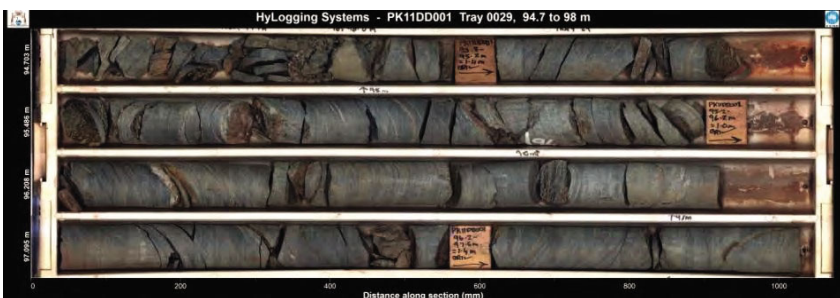
Sample numbers: LCMR07	Mineralogy	Block description
Depth: 46m depth	Iron rich microbands: Hematite 50%, euhedral 20ums Magnetite 50%, anhedral 30ums	Very fine grained hypogene altered rock, with very thin banding (microbands) of alternating iron oxides (no silica). Microbands contain no silica, contain magnetite and hematite minerals. large coarse grained veins of hypogene iron oxides cut these microbands, bringing in quartz.
Alteration : <i>Hypogene altered BIF</i>	Iron oxide veins Hematite 45%, euhedral 500um Magnetite 45% euhedral 400um Quartz 5%, anhedral 300um Goethite 5%, euhedral 100um	
Images 1. Drill core image		
Sample numbers: LCMR08	Mineralogy	Block description
Depth: 46.5m depth	Iron rich microbands: Hematite 50%, euhedral 20ums Magnetite 50%, anhedral 30ums	Very fine grained hypogene altered BIF containing some primary banding of silicate and iron oxides bands. Coarse grained hypogene altered iron oxides rich veins cut the banding.
Alteration : <i>Hypogene altered BIF</i>	Iron oxide veins Hematite 45%, euhedral 500um Magnetite 45% euhedral 400um Quartz 5%, anhedral 300um Goethite 5%, euhedral 100um	
Images 1. Drill core image		



Sample numbers: LCMR09	Mineralogy	Block description
Depth: 48.5m depth Alteration : <i>Least altered BIF</i>	Silica rich bands: Quartz 80%, anhedral 300 µm Magnetite:10%, euhedral 300 µm Hematite dusting: 10%, anhedral 100µm Iron oxide rich bands: Magnetite 50%, anhedral 500 µm Hematite dusting 45%, anhedral 100 µm Goethite 10%, 100 µm	Least altered BIF rock. Regularly banded (1mm-1cm thick) of iron rich and silica rich bands. Silica rich bands (50%) predominately recrystallised quartz with some disseminated hematite, or hematite 'dusting'. Iron rich bands (50%)slightly oxidised minerals with some quartz present.
Images 1. Drill core image		


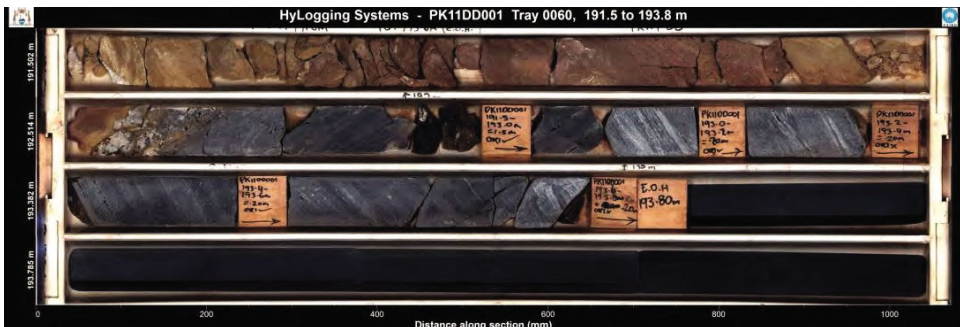
Sample numbers: LCMR10	Mineralogy	Block description
Depth: 55.5depth	Silica rich bands: Quartz 80%, anhedral 300 µm Magnetite:10%, euhedral 300 µm Hematite dusting: 10%, anhedral 100µm Iron oxide rich bands: Magnetite 50%, anhedral500 µm Hematite dusting 45%, anhedral 100 µm Goethite 10%, 100 µm	Least altered BIF rock. Regularly banded (1mm-1cm thick) of iron rich and silica rich bands. Silica rich bands (50%) predominately recrystallised quartz with some disseminated hematite, or hematite 'dusting'. Iron rich bands (50%)slightly oxidised minerals with some quartz present. Some veining cut the BIF, 1mm thick quartz veins
Alteration : <i>Least altered BIF</i>		
Images 1. Drill core image		
Sample numbers: LCMR11	Mineralogy	Block description
Depth: 60.5m depth	Silica rich bands: Quartz 70%, anhedral goethite 15%, euhedral Hematite 15% euhedral Iron oxide rich bands: Hematite 60%, euhedral Goethite 30%, euhedral Quartz 10%, anhedral	Hypogene altered BIF with fold structures. Thinly banded, 0.5mm-1cm thick. Hypogene alteration is pre folding event, strain on minerals at fold hinges and brecciation of bands. Iron oxides are a smaller grain size at fold hinges, with silica bands containing more iron oxides.
Alteration : <i>Folded Hypogene altered BIF</i>		
Images 1. Drill core image		

Sample numbers: LCMR12	Mineralogy	Block description
Depth: 65m depth Alteration : <i>Folded Hypogene altered BIF</i>	Silica rich bands: Quartz 70%, anhedral goethite 15%, euhedral Hematite 15% euhedral Iron oxide rich bands: Hematite 60%, euhedral Goethite 30%, euhedral	Hypogene altered BIF with fold structures. Thinly banded, 0.5mm-1cm thick. Hypogene alteration is pre folding event, strain on minerals at fold hinges and brecciation of bands. Iron oxides are a smaller grain size at fold hinges, with silica bands containing more iron oxides
Images 1. Drill core image		
Sample numbers: LCMR14	Mineralogy	Block description
Depth: 70.5m depth Alteration : <i>Hypogene veining altered BIF,</i>	Hypogene vein: Martite 40%, euhedral Specular hematite 40% Goethite 15%, overprint, laths Void 5%, anhedral	Hypogene veining completely altering the BIF rock, no primary banding is observed. Silica has been completely removed, some voids and supergene goethite enrichment is present.
Images 1. Drill core image		

Sample numbers: LCMR15	Mineralogy	Block description
Depth: 71m depth Alteration : <i>Intensely supergene modified hypogene vein altered BIF</i>	Hypogene veins: Hematite 70%, euhedral Quartz 30%, anhedral Disseminated iron oxide bands: Hematite 60%, euhedral Quartz 40%, anhedral Silica banding: Quartz 60%, anhedral Goethite 20%, euhedral Hematite 20%, anhedral	Supergene modified hypogene rock, thinly banded and very fine grained. Hypogene veins running parallel to banding. Banding consists of silica rich bands and disseminated iron oxide bands.
Images 1. Drill core image		
Sample numbers: LCMR17	Mineralogy	Block description
Depth: 86m depth Alteration : <i>Supergene altered mafic</i> Proximal zone	Quartz 5% Goethite 30% Hematite (cryptocrystalline?) 40% Kaolinite 25%	Supergene altered mafic rock, total replacement of all primary minerals. Highly schistose texture, very fine grained rock.
Images 1. Drill core image		

Sample numbers: LCMR18	Mineralogy	Block description
Depth: 90.5m depth	Quartz 10% Goethite 25% Hematite (cryptocrystalline?) 40% Kaolinite 15%	Supergene altered mafic rock, total replacement of all primary minerals. Highly schistose texture, very fine grained rock.
Alteration : <i>Supergene altered mafic</i> Proximal zone		
Images 1. Drill core image		
Sample numbers: LCMR19	Mineralogy	Block description
Depth: 96.5 m depth	Epidote 30% Chlorite 20% Quartz 10% Feldspar 5% Magnetite 5%	Proimal mafic rock with no supergene alteration. Highy schistose rock with a fine grained schistose matrix of quartz and (sericite?). large epidote veins showing deformation, amphiboles has been replaced.
Alteration : <i>Mafic rock proximal</i>		
		

Sample numbers: LCMR20	Mineralogy	Block description
Depth: 100.5m depth	Carbonate 40% Quartz 30% Chlorite 10% Feldspar 20%	Very fine grained schistose rock with coarse grained carbonate veining. Infilling after deformation/alteration of mafic. Late carbonate episode.
Alteration : <i>Mafic</i>		
Images 1. Drill core image		
Sample numbers: LCMR22	Mineralogy	Block description
Depth: 134m depth	Hornblende 55% Quartz 30% Opaque (magnetite) 10% Plagioclase 5%	Strongly foliated mafic rock, large amphibole laths show strong foliation (hornblende, biotite). Chlorite is replacing primary amphiboles.
Alteration : <i>Least altered mafic</i>		
Images 1. Drill core image		

Sample numbers: LCMR23	Mineralogy	Block description
Depth: 153m depth	Hornblend 50% Biotite 30% Opaque 10% Quartz 10%	Fine grained mafic rock, no foliation of minerals. Amphiboles are not lath shaped rounded clasts. Amphiboles textures are very different, may have been product of metamorphism.
Alteration : <i>Least altered mafic</i>		
Images 1. Drill core image		
Sample numbers: LCMR24	Mineralogy	Block description
Depth: 192.5m depth	Hematite(specular) Magnetite	Primary banding of this rocks is not clear, silica bands have been replaced with iron oxides. very thinly banded (<0.5mm) . Cryptocrystalline quartz is present, no supergene minerals. Hypogene altered footwall BIF. Pyrite observed, but not enough to have any significance.
Alteration : <i>Footwall BIF Highly magnetic dark rock</i>		
Images 1. Drill core image		

**APPENDIX 9: GEOSCIENCES PRODUCT DESCRIPTION (MFEM
SCRIPTS) - SELECTED VNIR AND SWIR ACTIVE MINERAL
GROUP/PHASES**

Product name	Minerals detected	Base algorithm	Filters/Masks	Lower stretch limit	Upper stretch limit (based on UGD1683)	related publication	Comments on general accuracy
Ferric oxide abundance (Ferric_oxide_abundance.txt)	Hematite, goethite, jarosite, "limonite"	Continuum removed depth of the 900 nm absorption calculated using a fitted 2 nd order polynomial between 776 and 1050 nm 900D	R450 > R1650	0.04: low content	not specified yet - depending on results from other drill cores	further developed on the basis of Haest et al, (2012a,b), which used a 4th order polynomial or 4 band ratio approach	High: Complicated by (1) water vapour residuals; (2) mixing with green and dry vegetation, carbon black (e.g. soil carbon); and (3) ferrous iron in silicates/carbonates. Rocklea case study: RMSE = 9.7%
Ferrous iron abundance (Ferrous iron abundance.txt)	Fe ²⁺ in silicates & carbonates. (Fe-chlorites, Fe-amphibole, Fe-pyroxene, Fe-olivine, Fe-carbonate)	$(R_{920}+R_{1650}) / (R_{1020}+R_{1235})$ Ferrous		~1.005: low content	not specified yet - depending on results from other drill cores	Laukamp et al. (2012)	Moderate. Broad absorption centred at ~1100nm can be influenced by ferrous iron in a range of silicates and carbonates. Including non-OH-bearing minerals like pyroxenes and garnets, as well as ferric iron.

Opagues 1 (greybody) (Opagues_1.txt)	“Reduced” materials such as carbon black, sulphides and magnetite as well as Mn oxides. Note sulphides and magnetite are expected to easily oxidise in the regolith to other minerals.	(R456)/(R1650) OPAQUES_450D16 50	albedo @ 1650 nm <30%	0.25: low content	not specified yet - depending on results from other drill cores		Moderate: Errors introduced by a lack of Fe3+ absorption in the visible, e.g. iron oxide poor clays that in theory would be masked by the <30% albedo but may be in partial “shadow”.
opaques2 (opaques2inv.txt)	“Reduced” materials such as carbon black, sulphides and magnetite as well as Mn oxides.	albedo @ 1650 nm 1650	OPAQUES_45 0D1650 >0.25; albedo @ 1650 nm 1650 <30%	2: low content	not specified - depending on samples		
White mica and Al-smectite abundance (wmAlsmat.txt)	Abundance of white micas (e.g. illite, muscovite, paragonite, brammalite, phengite, lepidolite, margarite) and smectites (montmorillonite, beidellite)	Relative absorption depth of the 2200 nm absorption for which the continuum is removed between 2120 and 2245, determined using a 3 band polynomial fit around the band with the lowest reflectance. 2200D3pfit	(R2326+R2376) / (R2343+R2359)) 2350DE >0.035) + ((R ₂₁₃₈ +R ₂₁₉₀) / (R ₂₁₅₆ +R ₂₁₇₉) 2160D2190 <1.063	0.02: low content	not specified yet - depending on results from other drill cores	further developed on the basis of Sonntag et al. (2012), which used a 4th order polynomial or 4 band ratio approach	Moderate: Inherent errors related to the process of masking rather than unmixing. That is, the threshold levels on mask parameters could exclude/include other materials especially for “lower” levels.

White mica and Al-smectite composition (wmAlsmci.txt)	Tschermak substitution of white micas, ranging from paragonite, brammalite, to illite, muscovite to phengite, and smectites, ranging from beidellite to montmorillonite.	Minimum wavelength of the 2200 nm absorption for which the continuum is removed between 2120 and 2245, determined using a 3 band polynomial fit around the band with the lowest reflectance. <i>2200W3pfit</i>	$\frac{(R_{2326}+R_{2376})}{(R_{2343}+R_{2359})} > 0.035 + \frac{((R_{2138}+R_{2190}) / (R_{2156}+R_{2179}))}{2160D2190} < 1.063$	2180 nm: Al-rich mica (muscovite, illite, paragonite, brammalite, lepidolite)	2220 nm: Al-poor mica (~phengite)	further developed on the basis of Sonntag et al. (2012), which used a 4th order polynomial or 4 band ratio approach	High:
Kaolin abundance index	Kaolin group minerals, namely kaolinite halloysite, dickite and nacrite	2200D (Normalized depth of a fitted 4th order polynomial between 2120 and 2245 nm)	$\frac{2160D}{((R_{2138}+R_{2190})/(R_{2156}+R_{2179}))} > 1.005$			Sonntag et al. (2012)	
Kaolin composition index	Composition and crystallinity of kaolin group minerals ranging from well-ordered kaolinite to halloysite to dickite (and nacrite)	$[(R_{2138}+R_{2173})/R_{2156}]/[(R_{2156}+R_{2190})/R_{2173}]$	$2200D > 0.005$			Sonntag et al. (2012)	

chlorite-epidote(-biotite) abundance (chlepai3pfit.txt)	Chlorite, epidote, biotite	Relative absorption depth of the 2250 nm absorption for which the continuum is removed between 2230 and 2270, determined using a 3 band polynomial fit around the band with the lowest reflectance. 2250D3pfit	2250D3pfit >0.01, 2230nm < 2250w vl <2270nm;	0.02: low content	not specified yet - depending on results from other drill cores	further developed on the basis of Sonntag et al. (2012), which used a 4th order polynomial or 4 band ratio approach	probably some correlation with Ferrous iron abundance!
chlorite(-biotite) abundance (chlai.txt)	Chlorite, biotite	Relative absorption depth of the 2250 nm absorption for which the continuum is removed between 2230 and 2270, determined using a 3 band polynomial fit around the band with the lowest reflectance. 2250D3pfit	2250D3pfit >0.01, 2230nm < 2250wxl <2270nm; 1550Dpoly <0.01	0.02: low content	not specified yet - depending on results from other drill cores	further developed on the basis of Sonntag et al. (2012), which used a 4th order polynomila or 4 band ratio approach	probably some correlation with Ferrous iron abundance!

Chlorite composition (chlepci3pfit.txt)	estimation of the Mg/Fe-ratio (~Mg#) of Chlorites	Minimum wavelength of the 2250 nm absorption for which the continuum is removed between 2230 and 2270, determined using a 3 band polynomial fit around the band with the lowest reflectance. <i>2250W3pfit</i>	2250D3pfit >0.01, 2230nm < 2250w vl <2270nm; 1550Dpoly <0.01	2248nm: Mg-rich (Bishop et al., 2008)	2261nm: Fe-rich (Bishop et al., 2008)		Medium: high influence of abundance of epidote and biotite!
epidote abundance (epai.txt)	epidote	Relative absorption depth of the 2250 nm absorption for which the continuum is removed between 2230 and 2270, determined using a 3 band polynomial fit around the band with the lowest reflectance. 2250D3pfit	2250D3pfit >0.01, 2230nm < 2250w vl <2270nm; 1550Dpoly >0.01	0.02: low content	not specified yet - depending on results from other drill cores		probably some correlation with Ferrous iron abundance!

Amphibole & Talc abundance (Amph_Talc_abundance.txt and Amph_Talc_abundance_without_kaol_inmask.txt)	Abundance of amphibole and talc	2380D ((R2365+R2415)/(R2381+R2390))	Composite mask* + MgOH abundance > 1.01 (+ 2160D2190 < 1.005)	1.005 : low content	not specified yet - depending on results from other drill cores	Laukamp et al. (2012)	
Carbonates abundance (carbai3pfit.txt)	carbonates vs. MgOH-bearing silicates, based on left-asymmetry of CO ₃ feature @ 2340	Relative absorption depth of the 2340 nm absorption for which the continuum is removed between 2270 and 2370, determined using a 3 band polynomial fit around the band with the lowest reflectance. 2340D	2340D >0.04, 2295nm< 2340W <2360nm, 2250D < 0.025, 2380D <0.1117* 2340D +0.0002, Asymmetry of the 2340 absorption using a fitted 4th order polynomial between 2120 and 2370: 2340_left_asym > 1.13	0.05 : low content	not specified yet - depending on results from other drill cores	further developed on the basis of Sonntag et al. (2012), which used a 4th order polynomial or 4 band ratio approach	

Carbonate composition (carbci3pfit.txt)	separating calcite, dolomite, siderite, ...	Minimum wavelength of the 2340 nm absorption for which the continuum is removed between 2270 and 2370, determined using a 3 band polynomial fit around the band with the lowest reflectance. 2340W	2340D >0.04, 2295nm< 2340W <2360nm, 2250D < 0.025, 2380D <0.1117* 2340D +0.0002, Asymmetry of the 2340 absorption using a fitted 4th order polynomial between 2120 and 2370: 2340_left_asym > 1.13	2303 nm: magnesite; 2326 nm: dolomite	2343 nm: calcite	further developed on the basis of Sonntag et al. (2012), which used a 4th order polynomial or 4 band ratio approach	Moderate: works well for those carbonates, which are not masked out
---	---	---	--	---------------------------------------	------------------	---	---

Base scripts

Product name	Minerals detected	Base algorithm	Filters/ Masks	Lower stretch limit	Upper stretch limit (based on UGD1683)	related publication	Comments on general accuracy
650D	Yellowness	Continuum removed depth of 650nm CFA,1 calculated using a fourth- order polynomial between 600 and 740 nm				Haest et al, (2012a,b)	
900D	Fe (oxyhydr-)oxides	Continuum removed depth of 900 nm CFA,2, calculated using a second-order polynomial between 776 and 1,050 nm				Haest et al, (2012a,b)	
900wvl	Fe (oxyhydr-)oxides	Continuum removed wavelength of 900 nm CFA,2 calculated using a fourth-order polynomial between 776 and 1,150 nm				Haest et al, (2012a,b)	
1300wvl	Fe oxyhydroxide type	Position of maximum reflectance between 1,260 and 1,420 nm				Haest et al, (2012a,b)	
1300R/1800R	~vitreous index	Ratio of maximum reflectance at 1,340 ± 80 nm over the minimum reflectance at 1,780 ± 40 nm				Haest et al, (2012a,b)	
1300R/2500R	~water index	Ratio of maximum reflectance at 1,340 ± 80 nm over the minimum reflectance at 2,500 nm				Haest et al, (2012a,b)	

1480D	prehnite	Relative absorption depth of the 1480 nm absorption for which the continuum is removed between 1450 and 1500, determined using a 3 band polynomial fit around the band with the lowest reflectance. 1480D				Stam et al. (in prep)	
1550D (1550Dpoly.txt)	epidote, clinozoisite (minor in chlorite)	Relative absorption depth of the 1550 nm absorption for which the continuum is removed between 1500 and 1610, determined using a 3 band polynomial fit around the band with the lowest reflectance. 1550D					conflict with gypsum, when used for identification of epidote series minerals
1550W	epidote, clinozoisite	Minimum wavelength of the 1550 nm absorption for which the continuum is removed between 1500 and 1610, determined using a 3 band polynomial fit around the band with the lowest reflectance. 1550W		epidote (in Yilgarn study by Roache et al., 2010: 1550W < 1552.5)	clinozoisite (in Yilgarn study by Roache et al., 2010: 1550W > 1552.5)		conflict with gypsum, when used for identification of epidote series minerals
N1650R	Albedo	Normalized reflectance at $1,650 \pm 100$ nm					
1760D	sulphates (e.g. gypsum and alunite, but not jarosite)	$(R1730+R1790)/(R1740+R1780)$ 1760D					

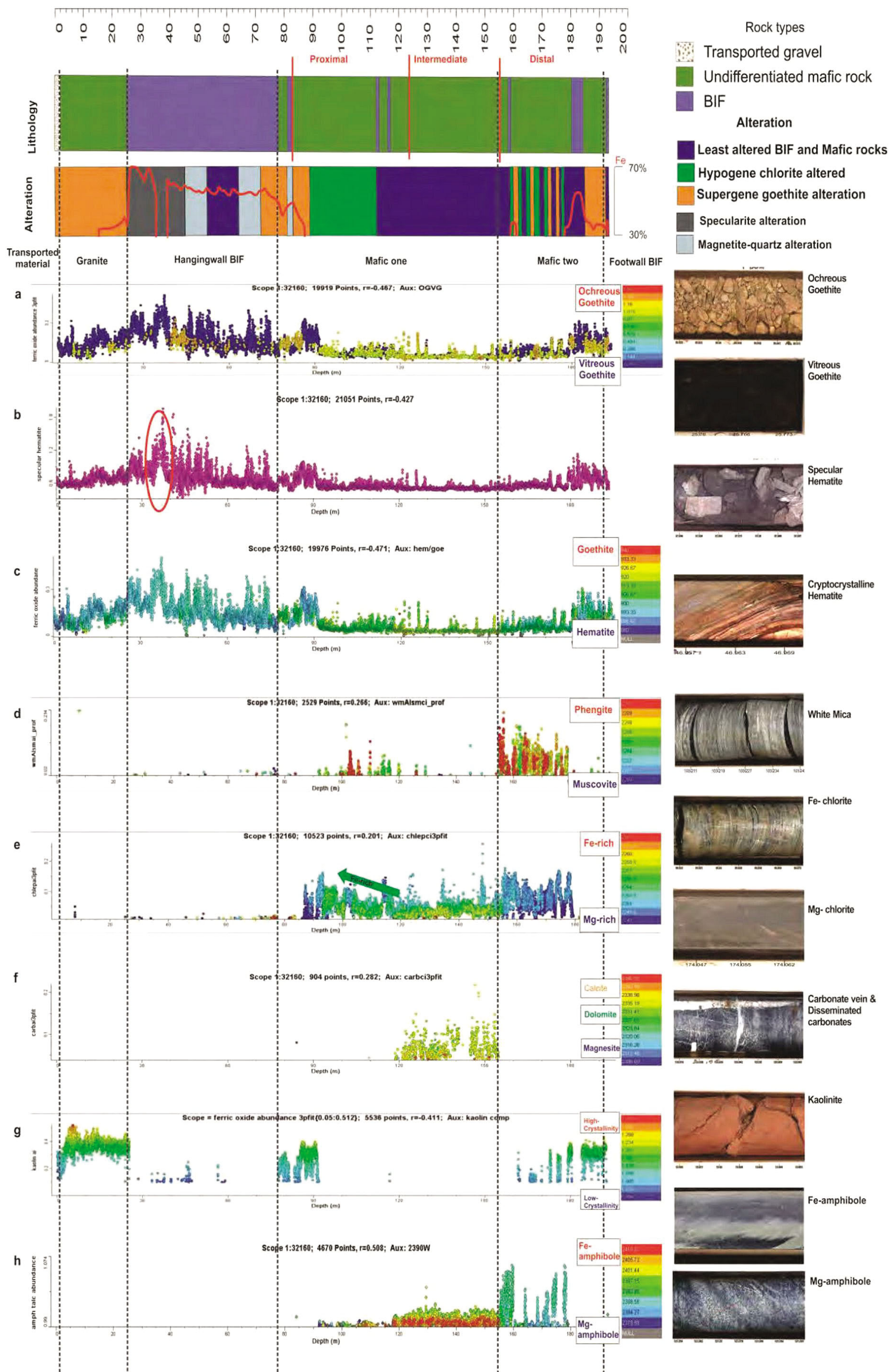
2080D3pfit	Depth of the 2080 feature, evident in talc. Useful for separating talc from Amphiboles, the latter ones in general not showing this absorption feature.	Depth of the 2080 nm absorption feature, for which the continuum is removed between 2060 and 2100, determined using a second order polynomial fitted through the 3 bands with the lowest reflectance. 2080D				Laukamp et al. (2012)	
2200D3pfit (2200D3pfit.txt)	Abundance of Al-clays	Relative absorption depth of the 2200 nm absorption for which the continuum is removed between 2120 and 2245, determined using a 3 band polynomial fit around the band with the lowest reflectance. 2200D					
2200W3pfit (2200W3pfit.txt)	Tschermak substitution of Al-clays	Minimum wavelength of the 2200 nm absorption for which the continuum is removed between 2120 and 2245, determined using a 3 band polynomial fit around the band with the lowest reflectance. 2200W		~ 2180 nm : Al-rich	~ 2215 nm : Al-poor		
2250D3pfit (2250D3pfit.txt)	Chlorite, epidote, biotite	Relative absorption depth of the 2250 nm absorption for which the continuum is removed between 2230 and 2280, determined using a 3 band polynomial fit around the band with the lowest reflectance. 2250D					

2250W3pfit (2250W3pfit.txt)	Estimation of the Mg/Fe-ratio (~Mg#) in chlorite, but also the shift of an coinciding absorption feature in epidote and bitotite, where the wavelength position is not necessarily only due to the Mg#, but possibly more due to the relative Al, Fe ³⁺ or Ca content.	Minimum wavelength of the 2250 nm absorption for which the continuum is removed between 2230 and 2280, determined using a 3 band polynomial fit around the band with the lowest reflectance. 2250W		2248nm: Mg-rich (Bishop et al., 2008)	2261nm: Fe-rich (Bishop et al., 2008)		
2290D	Fe smectite	Continuum removed depth of fourth-order polynomial between 2,270 and 2,330 nm				Haest et al, (2012a,b)	
2290wvl	Fe smectite	Continuum removed wavelength of fourth-order polynomial, fitted between 2,270 and 2,330 nm				Haest et al, (2012a,b)	
2320W	In carbonates: wavelength position of the 2320 feature relates to Mg and/or Fe content of carbonates	Wavelength of absorption minimum calculated using a fitted fourth order polynomial between 2300 and 2345 nm, focused between 2310 and 2340 nm. 2320W				Laukamp et al. (2012)	
2330Asym	Carbonates	Continuum removed asymmetry of fourth-order polynomial, fitted between 2,120 and 2,370 nm				Haest et al, (2012a,b)	

2350Dey	Depth of the 2350 feature, evident in white mica. Used to separate white mica from Al-smectites.	$(R2326+R2359)/(R2343+R2359)$ 2350De		<1.025: Al-smectite (when 2200D present) < not applied in this project	>1.035: white mica (when 2200D present) < not applied in this project	Haest et al, 2012a,b)	
2380D	Depth of the 2380 feature, evident in for example amphiboles and talc	$(R2365+R2415)/(R2381+R2390)$ 2380D				Haest et al, (2012a,b)	
2390W3pfit (2390W3pfit.txt)	estimation of the Mg/Fe-ratio (~Mg#) in for example amphiboles and talc	Wavelength of absorption minimum calculated using a fitted fourth order polynomial between 2365 and 2430 nm, focused between 2380 and 2410 nm. 2390W		2382nm: Mg-rich (Laukamp et al., 2012)	2406nm: Fe-rich (Laukamp et al., 2012)	Laukamp et al. (2012)	
2160D2190	intensity of the 2160 feature, indicative for Kaolin abundance. Used to separate Kaolin from non Kaolin Al-silicates (i.e. Al-smectite & white mica)	$(R2136+R2188)/(R2153+2171)$ 2160D2190		<1.005: no kaolin	>1.005: kaolin	Haest et al, (2012a,b)	

- Cudahy, T., Jones, M., Thomas, M., Laukamp, C., Caccetta, M., Hewson, R., Rodger, A., Verrall, M. (2008): Next Generation Mineral Mapping: Queensland airborne HyMap and satellite ASTER surveys 2006-2008.- CSIRO report P2007/364, 161pp.
- Haest, M., Cudahy, T., Laukamp, C., Gregor, S. (2012a): Quantitative mineralogy from visible to shortwave infrared spectroscopic data - I. Validation of mineral abundance and composition products of the Rocklea Dome channel iron deposit in Western Australia.- *Economic Geology*, 107, 209 - 228. (IF10: 2.021, 5yearIF10: 2.761; citations: 1)
- Haest, M., Cudahy, T., Laukamp, C., Gregor, S. (2012b): Quantitative mineralogy from visible to shortwave infrared spectroscopic data - II. 3D mineralogical characterisation of the Rocklea Dome channel iron deposit, Western Australia - *Economic Geology*, 107, 229 - 249. (IF10: 2.021, 5yearIF10: 2.761; citations: 1)
- Laukamp, C., Termin, K.A., Pejčic, B., Haest, M., Cudahy, T. (2012): Vibrational Spectroscopy of Calcic Amphiboles - Applications for Exploration and Mining.- *European Journal of Mineralogy*, 24, 863-878. (IF10: 1.469, 5yearIF10: 1.487)
- Laukamp, C., Cudahy, T., Caccetta, M., Chia, J., Gessner, K., Haest, M., Liu, Y.C., Rodger, A. (2010): The uses, abuses and opportunities for hyperspectral technologies and derived geoscience information.- *AIG Bulletin*, 51(Geo-Computing 2010 Conference, Brisbane, September 2010): 73-76.
- Roache, T.J., Walshe, J.L., Huntington, J.F., Quigley, M.A., Yang, K., Bil, B.W., Blake, K.L., Hyvaerinen, T. (2011): Epidote-clinzoisite as a hyperspectral tool in exploration for Archean gold.- *Australian Journal of Earth Sciences*, 58 (7), 813-822.
- Sonntag, I., Laukamp, C., Hagemann, S. (2012): Low potassium hydrothermal alteration in low sulfidation epithermal systems as detected by IRS and XRD: an example from the Co-O Mine, Eastern Mindanao, Philippines.- *Ore Geology Reviews*, 45, 47-60. (IF10: 2.079, 5yearIF10: 2.2; citations: 1)

APPENDIX 10: FIGURE 20 A3 SIZE



This Record is published in digital format (PDF) and is available as a free download from the DMP website at
<www.dmp.wa.gov.au/GSWApublications>.

Further details of geological products produced by the Geological Survey of Western Australia can be obtained by contacting:

Information Centre
Department of Mines and Petroleum
100 Plain Street
EAST PERTH WESTERN AUSTRALIA 6004
Phone: +61 8 9222 3459 Fax: +61 8 9222 3444
www.dmp.wa.gov.au/GSWApublications

